E.O. Paton Electric Welding Institute of the National Academy of Science of Ukraine
International Association “Welding”

The Paton Welding Journal

08
2024

International Scientific-Technical and Production Journal ♦ Founded in January 2000 (12 Issues Per Year)

Address of Editorial Office
E.O. Paton Electric Welding Institute, 11 Kazymyr Malevych Str., 03150, Kyiv, Ukraine
Tel.: (38044) 205 23 90, E-mail: patonpublishinghouse@gmail.com; journal@paton.kiev.ua
https://patonpublishinghouse.com/eng/journals/tpwj

The Journal was registered by the National Council of Ukraine on Television and Radio Broadcasting on 09.05.2024,
carrier identifier R30-04569; ISSN 0957-798X; DOI: http://dx.doi.org/10.37434/tpwj

Subscriptions, 12 issues per year:
348 Euro — annual subscription for the printed (hard copy) version, air postage and packaging included;
288 Euro — annual subscription for the electronic version (sending issues in pdf format or providing access to IP addresses).

Representative Offices of “The Paton Welding Journal”:

BRAZIL, Arc Dynamics
Address: Nova Iguacu, Rio de Janeiro, Brazil
Daniel Adolpho, Tel.: +55 21 9 6419 5703, E-mail: dadolpho@arcdynamics.com.br

BULGARIA, Bulgarian Welding Society
Address: Blvd. Asen Yordanov No.10, Sofia 1592, Bulgaria
Pavel Popgeorgiev, Tel.: +359 899 96 22 20, E-mail: office@bws-bg.org

CHINA, China-Ukraine Institute of Welding, Guangdong Academy of Sciences
Address: Room 210, No. 363 Changxing Road, Tianhe, Guangzhou, 510650, China
Zhang Yupeng, Tel.: +86-20-61086791, E-mail: patonjournal@gwi.gd.cn

POLAND, PATON EUROPE Sp. z o. o.
Address: ul. Kapitałowa 4, 35-213, Rzeszów, Poland
Anton Stepakhno, Tel.: +38067 509 95 67, E-mail: Anton.Stepakhno@paton.ua

The content of the Journal includes articles received from authors from around the world in the field of welding, cutting, cladding, soldering, brazing, coating, 3D additive technologies, electrometallurgy, material science, NDT and selectively includes translations into English of articles from the following journals, published in Ukrainian:

- «Avtomatychne Zvaryuvannya» (Automatic Welding), https://patonpublishinghouse.com/eng/journals/as;
- «Suchasna Elektrometalurhiya» (Electrometallurgy Today), https://patonpublishinghouse.com/eng/journals/sem;
- «Tekhnichna Diahnostyka ta Neruinivnyi Kontrol» (Technical Diagnostics & Nondestructive Testing), https://patonpublishinghouse.com/eng/journals/tdnk.

CONTENTS

ORIGINAL ARTICLES

*Translated Article(s) from “Avtomatychne Zvaryuvannya” (Automatic Welding), No. 3, 2024.

**Translated Article(s) from “Avtomatychne Zvaryuvannya” (Automatic Welding), No. 4, 2024.

***Translated Article(s) from “Suchasna Elektrometalurhiya” (Electrometallurgy Today), No. 2, 2024.

****Translated Article(s) from “Tekhnichna Diahnostyka ta Neruinivnyi Kontrol” (Technical Diagnostics & Nondestructive Testing), No. 2, 2024.

Indexing: The electronic edition of the Journal is stored in the V.I. Vernadsky National Library of Ukraine (eVerLib), included in the OPEN UKRAINIAN CITATION INDEX database and international databases: CROSSREF, EBSCO, Google Scholar, INDEX COPERNICUS, IET Inspec, ULRICHSWEB.

DOI: https://doi.org/10.37434/tpwj2024.08.01

CHALLENGES FOR TESTING HYDROGEN-ASSISTED COLD CRACKING IN WELD SEAMS OF HIGH-STRENGTH STEEL GRADES

M. Rhode[1,2], T. Mente[1], T. Kannengießer[1,2], T. Schaupp[3], A. Zavdoveev[4]

[1]Bundesanstalt für Materialforschung und -prüfung (BAM), Berlin, Germany
[2]Otto-von-Guericke University, Magdeburg, Germany
[3]SPC Werkstofflabor GmbH, Westhausen, Germany
[4]E.O. Paton Electric Welding Institute of the NASU
11 Kazymyr Malevych Str., 03150, Kyiv, Ukraine

ABSTRACT

Hydrogen can cause weld cold cracking even days after fabrication. In this respect, higher strength steels present a challenge to established cold crack testing. In general, the tolerable hydrogen concentration for crack prevention decreases with increasing material strength. In addition, advanced welding processes require changes in weld geometry and heat input. This directly influences the formation of crack-critical microstructures, e.g. in hardened areas of the heat-affected zone. The limits of use and application of modern cold cracking tests are evaluated by (1) the externally loaded Implant-test and (2) the self-restraint Tekken-test. In particular, external mechanical stresses, which cause additional mechanical loads on the components during welding, must be considered due to the component-specific stiffness of high-strength steels. Accompanying test methods for determining hydrogen concentration and diffusion in welds are presented, such as carrier gas hot extraction for determining hydrogen concentration (ISO 3690) or temperature-dependent diffusion coefficients. These values are of great importance for a holistic approach to the evaluation of the cold cracking sensitivity of high strength steels.

KEYWORDS: hydrogen, cold crack, test, welding, high-strength steel

COLD CRACKING IN HIGH-STRENGTH STEEL WELDING JOINTS

High-strength structural steels have been used successfully in mechanical and plant engineering for several decades, especially increasingly for offshore wind turbines and bridge construction. Manufacturers offer numerous base materials and adapted welding consumables for this purpose. However, the increasing strengths place significantly higher demands on welding processing due to narrower process limits [1, 2]. Improper weld processing can result in weld damage. Hydrogen-assisted cracking (HAC) is a major risk because it can occur with a significant time delay. HAC microcracks are caused by the critical interaction of local crack-critical microstructure (e.g., hardened heat-affected zone — HAZ), diffusible hydrogen concentration, and local strain/stress. The main sources of hydrogen are moisture (electrode coating and flux) or contamination of the welded parts by hydrocarbon oils, greases, etc. or humid ambient conditions, e.g. during field welding.

During the last 20 years, the strength of high strength steels has been continuously improved by the addition of microalloying elements (V, Nb, Ti) [3]. The alloying concepts result in different weld microstructures and mechanical properties [4] and have a considerable influence (due to the precipitates formed) on the increased time delay of hydrogen diffusion [5]. Welded structures with yield strengths ≥ 960 MPa can be susceptible to HAC at hydrogen concentrations of

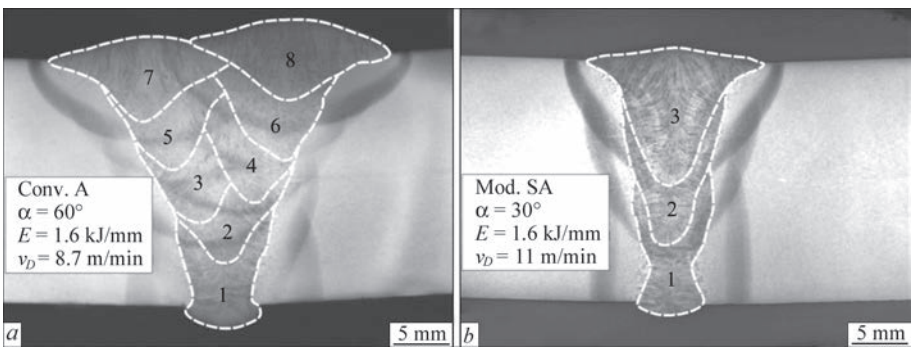

Figure 1. Influence of welding process/arc type on necessary weld bead number for constant weld heat input: *a* — conv. A, 60°, eight runs; *b* — mod. SA, 30°, three runs (Figure unchanged and taken from ref. [7], open access license CC-BY-4.0)

HD ≥ 1 ml/100 g [6]. To determine the cold crack resistance of base and filler materials, a test method is required that can reproduce realistic stresses at a practicable specimen level. The high strengths of modern materials and advanced welding processes, such as the arc form for focusing the welding heat input, e.g. by modified spray arc ("Mod. SA" in Figure 1, *b*) compared to the conventional arc ("Conv. A" in Figure 1, *a*), pose challenges for the cold crack testing [7, 8]. Figure 1, *a* and *b* are taken from ref. [7] (open access license CC-BY-4.0)

The old simplification/"general rule" that the risk of cracking increases almost exclusively with the hydrogen concentration does not apply to high-strength materials and especially to modern welding processes such as the modified spray arc ("mod. SA"). These influencing factors therefore require an adaptation of the existing cold crack tests.

CHALLENGES FOR COLD CRACKING TESTING

GENERAL REMARKS

More than 200 methods are available for the cold crack testing of a welded joints [9]. However, only a small number have found practical application. They are among the test methods for weldability, i.e. the ability of a component to be welded under given production conditions and design requirements so that it can perform its function. The susceptibility of the base metal (BM) and deposited filler metal to cold cracking must therefore always be determined as a function of the welding process and parameters used. Particular attention must be paid to the stiffness of the welded structure, i.e. its resistance to deformation due to external stresses. This has a significant influence (and associated thermomechanical effects during welding and cooling) on the susceptibility to cold cracking. Depending on the test method, cold crack tests provide qualitative (crack/no crack) or quantitative (parameter limit curves for crack-free welds) results for the materials/filler materials or welding parameters tested. According to [9–12], cold cracking tests are categorized by the test load:

SELF-RESTRAINT COLD CRACKING TESTS

impose a structural stress on the specimen resulting from its own design stiffness (resistance to shape and position change during welding). For example, these may be slit specimens with varying weld seam geometry or lap welds as circumferential welds. A phase transformation can add additional residual stresses to the overall level.

IN EXTERNALLY LOADED COLD CRACKING TESTS

the specimen is subjected to specific mechanical stresses in a preferred direction. The applied load is always superimposed on existing welding-specific residual stresses. The external load can be applied independently of the welding parameters and must be selected to reflect the practical application as realistically as possible, i.e. stressing the material up to the yield point for a selected geometry.

The most common cold cracking tests are standardized and can be found in the three parts of ISO 17642 [10–12]. The tests reach their limits for modern high-strength materials or adapted welding processes and must be adapted. Two examples of a self-loaded and externally loaded cold cracking test are presented below. In addition, hydrogen determination according to ISO 3690 [13] is briefly discussed.

TEKKEN-TEST

For the cold cracking TEKKEN test, according to ref. [11], a flat slot specimen with an inclined Y-groove is prepared to create a test weld closed at both ends with a length of 80 mm (see Figure 2, *a*). A single-pass weld is made in the Y-groove using the welding process parameters and filler materials to be tested. The

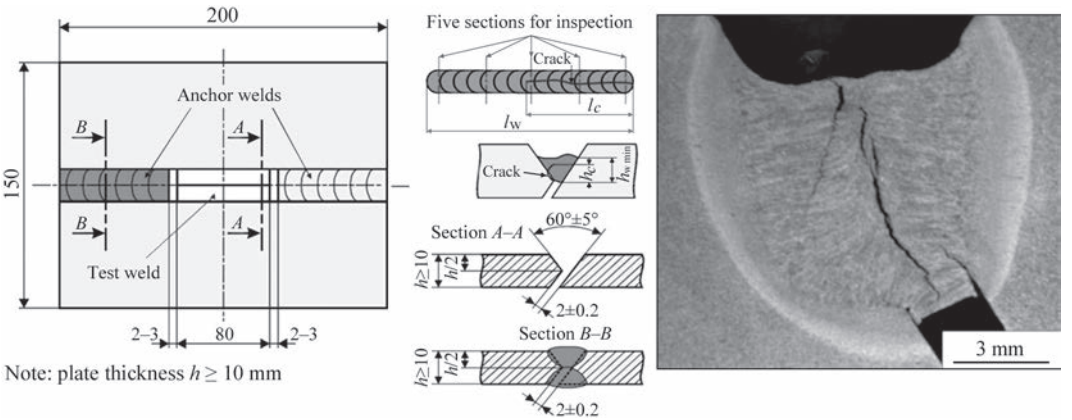

Figure 2. TEKKEN-Test: *a* — weld sample; *b* — welded Y-groove with cold crack, taken with permission by Springer Nature from ref. [9]

Y-groove serves as a mechanical notch, i.e. to increase the notch stress and locally preferential crack initiation. The sample geometry results in a hindered shrinkage during cooling of the weld seam, i.e. a self-restraint cold cracking test. Due to the slow diffusion of hydrogen, a waiting time of 48 hours after welding must be observed. The weld is then visually inspected. Any cracks found that are open to the surface are determined using the crack length coefficient (in %) from the total length of the cracks and the weld seam length. In addition, a light microscopic crack inspection is carried out in the weld metal (WM) and in the HAZ on five metallographic cross sections (see Figure 2, *b*). Both Figures 2, *a* and *b* were taken from the work of Boellinghaus et al., see ref. [9], with permission by Springer Nature.

Although the TEKKEN represents a cold cracking test, it can also be used as a hot cracking test due to the high mechanical restraint imposed by the specimen geometry. On the one hand in design specific hot cracking investigations under the high restraint conditions of the Tekken test. This must be evaluated especially in case of (1) higher alloyed materials or (2) when the main crack propagation is parallel to the welding direction [9]. In that case, a fractographic evaluation should be performed to distinguish between hot cracks in terms of solidification cracks. Actually "hot cracking safe" low-alloyed steels can show unexpected hot instead of cold cracking at very high mechanical strength level [14]. In addition, the root-cause of the cracking can be misinterpreted. It was recently reported that micro hot cracking in low-alloyed steels can be a potential site for further propagating cold cracks [15, 16].

The TEKKEN sample should have a minimum thickness of 10 mm to safely exclude distortions during welding and cooling and to ensure a sufficient stiffness [17]. It is standardized in the EN ISO 17642-2 [11]. Unfortunately, the applicability of this test is limited, and some boundary conditions should be considered.

- In the past, welded specimens were usually made from two individual sheets using anchor welds. Especially for high-strength materials, the issue of the anchor weld can fail due to the simple unavailability of adequate welding consumables. An alternative is to machine the Y-groove directly from the steel plate by EDM.
- In the case of high filler material strengths, the base material must have a similar strength or a significant plate thickness, otherwise the residual stresses in the WM will be distorted compared to real components. In addition, the specimen geometry is too "soft" and provides insufficient stiffness ratios. Therefore, the base and filler material combination should have similar values in terms of the yield strength (R_{eH}) or proof stress ($R_{P0.2}$) level. Alternatively, the specimen thickness, i.e. the sheet thickness, can be increased.
- For advanced welding processes such as mod. SA with a very short arc, it is necessary to adapt the weld geometry because the weld depth is smaller. This must be taken into account in the Y-joint in order to achieve the required root formation.

IMPLANT-TEST

The Implant-test (see ref. [12]) belongs to the group of externally loaded cold cracking tests. The load is applied via a welded-in cylindrical rod (implant pin with helical notch geometry), which is loaded in tension by a defined weight. The basic test setup is shown in Figure 3. Figure 3, *a* shows the so-called implant pin (left-hand side) and the machined annular or helical notch, of which the geometry is checked by a profile projector or stereomicroscope (see right-hand side of Figure 3, *a*). This notch ensures the concentration of the mechanical stresses, i.e. tightened local HAC conditions. The implant pin itself consists of the material to be tested. Figure 3, *c* shows the general assembly of the test-setup. Figure 3, *a* to c were taken from ref. [18] (via open access license CC-BY-4.0).

The implant pin is inserted into the hole (6 mm diameter) in the support plate (see Figure 3, *c*). The support plate and implant pin are joined by bead-on-plate welding using the appropriate filler material and welding parameters. After cooling to ambient temperature, the specimen is subjected to a static tensile load for ≥ 16 h. To determine the maximum test load, the load is successively increased with several welded specimens. The time-to-failure ("TTF") is recorded for each specimen. Occurring cracks are evaluated using metallographic methods. The implant specimen is then annealed at 250 to 300 °C for one hour. Free crack surfaces of the crack oxidize and can thus be distinguished from the unaffected residual fracture surface (after opening of the sample in the laboratory, if not fractured). The Implant-test permits a qualitative "crack or no crack" statement. Quantitative values such as minimum preheating temperature or welding heat input can be determined, as well as the maximum allowable stress for crack-free welds. This so-called "critical implant stress" represents the highest test load/stresses at which neither fracture nor incipient cracking occurs [7, 9, 18] and exemplarily shown in Figure 4, *c*. The corresponding remaining "critical" hydrogen concentration can be determined either by the analysis of the broken implant pin as well as by ISO 3690 samples to identify the initial diffusible hydrogen concentration [9, 12, 13].

Figure 4 shows different weld penetration depth for different implant specimens made of a high-strength

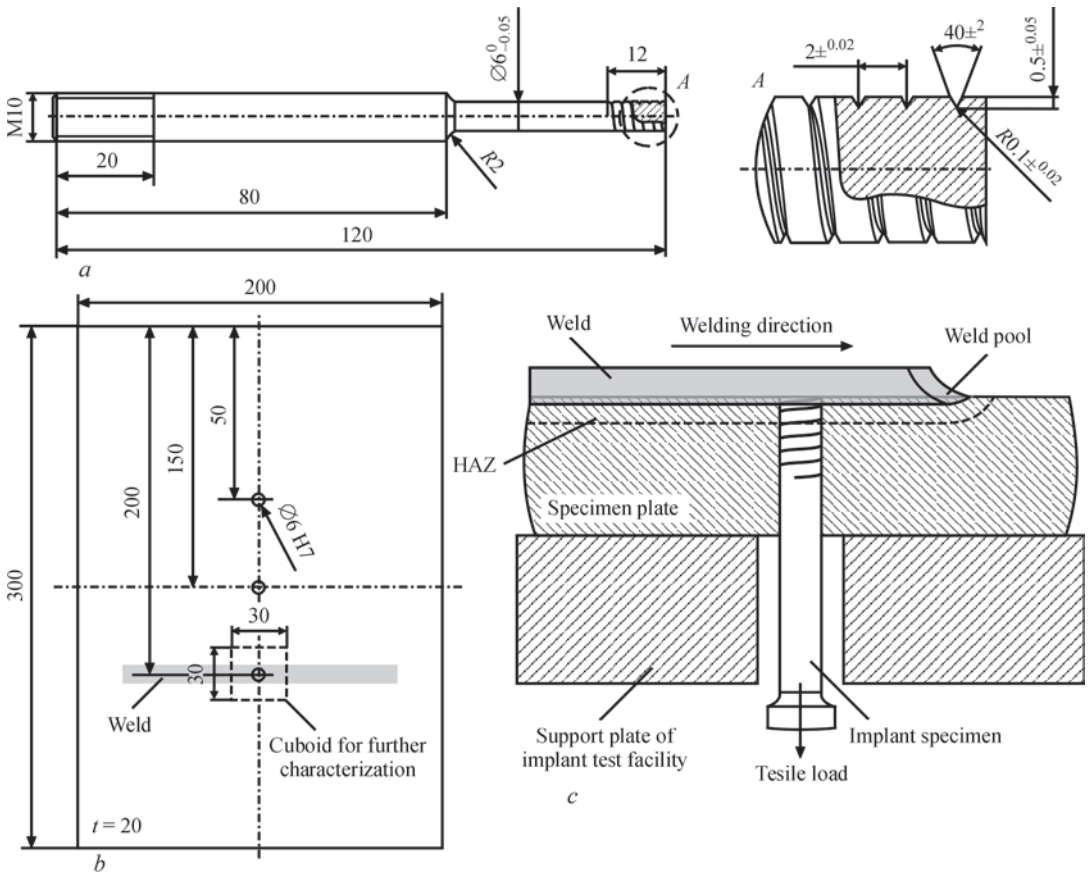

Figure 3. Implant test: *a* — implant pin with circumferential notch; *b* — BM support plate; *c* — schematic of test-setup, (unchanged Figure taken from ref. [18] with open access license CC-BY-4.0)

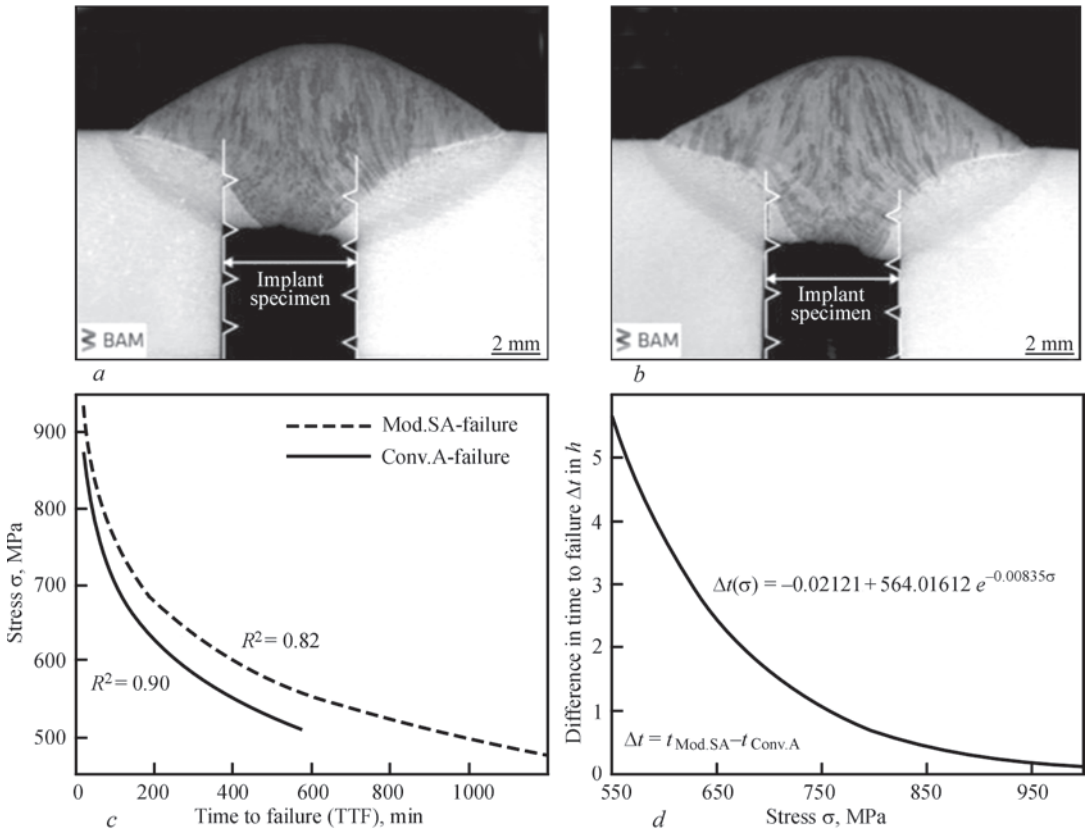

Figure 4. Implant-test: cross-sections of samples welded with: *a* — conv. A; *b* — mod. SA; *c* — calculated regression curves of implant samples; *d* — corresponding residuals, (Figure parts unchanged and rearranged, taken from ref. [7] with open access license CC-BY-4.0)

structural steel S960. Both samples were welded by metal active gas welding (GMAW) using conv. A (see Figure 4, *a*) or mod. SA (see Figure 4, *b*). It is evident that the penetration depth changes with the conventional or modified arc, regardless of the material grade tested. Thus, the Implant-test results differed significantly in terms of the time to failure achieved. For this reason, Figure 4, *c* shows the corresponding regression curves for both implant test series, and Figure 4, *d* shows the calculated differences in the TTF. The detailed work and results can be found in ref. [7]. Figure 4, *a* to *d* were taken from [7] (via open access license CC-BY-4.0).

In general, the Implant-test is used to standardize the cold cracking testing of base materials for coated electrode manual metal arc welding (MMAW), shielded metal arc welding (SMAW) with solid and flux-cored wire, and submerged arc welding (SAW) [9, 12]. However, similar restrictions apply to the Implant-test as to the Tekken test.

● Cold crack testing of filler materials is generally possible but requires extensive preparation of the Implant pin. This means that for newly developed filler materials, the suitability of weld crack testing must always be assessed first. For example (and as mentioned in section 2.2), hot microcracks must be anticipated as they may propagate as cold cracks at ambient temperature [15, 16].

● Advanced welding processes (such as mod. SA) require an adjustment of the weld geometry as the penetration depth is increased (see Figure 1, *b*). This affects the layer thickness, changes the hydrogen diffusion and in some cases significantly affects the crack resistance/critical implant stress (see Figure 3, *c* and *d*).

● The influence of the material must be amplified by the specific welding processing. In other words, the weldability of materials (especially for newly developed materials) must be of special interest prior to the industrial applications.

● In this context, the available minimum sheet thicknesses of the investigated high-strength steel limits the manufacturability of the Implant pins [18]. From that point of view, a critical evaluation of the implant pin geometry could be perhaps beneficial in the future.

● Another factor is that existing testing concepts are usually designed for specific material strength. The use of high-strength materials (e.g. S960 vs. S355 structural steel, i.e. 960 N/mm² vs. 355 N/mm² yield limit) requires correspondingly higher test loads to be applied. This requires stiffer test frames and advanced measurement technology (such as appropriate mechanical load frames).

DETERMINATION OF HYDROGEN CONCENTRATION IN ACCORDANCE WITH ISO 3690 USING CARRIER GAS HOT EXTRACTION

The measurement of hydrogen content, i.e. the extent to which a particular filler material introduces hydrogen into the weld pool, is essential in the welding process. An example of this is the HD classification. According to [13], an "HD5" specification guarantees that deposited weld metal contains ≤ 5 ml/100g Fe hydrogen. Considering the curves in Figure 2, *c*, this requirement becomes clear (degradation S960QL already at about 1.0 to 1.5 ml/100 g Fe hydrogen content in the WM [7, 18]. The ISO 3690 standard specifies requirements for test piece preparation (see Figure 5, *a*) and determination of the diffusible hydrogen in the WM for steels and applies to arc welding processes. For this purpose, the test piece is welded with a bead on plate seam, the run-off and run-off pieces are removed, and the center

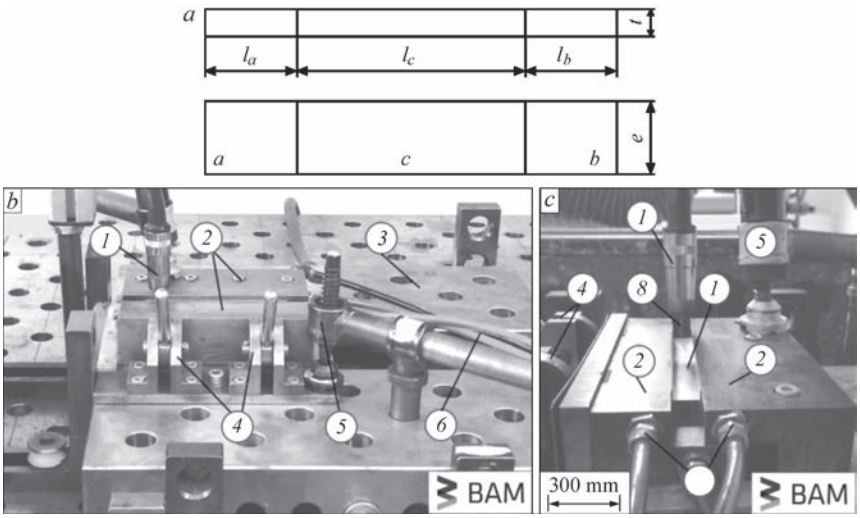

Figure 5. ISO 3690-welding: *a* — test sample; *b–c* — welding fixture, taken with permission from Springer Nature from ref. [19]: *1* — welding torch; *2* — copper clamps; *3* — fixing plate; *4* — toggle clamps; *5* — attachment; *6* — cooling water; *7* — specimen; 8 — welding consumable

section is stored deep-frozen in liquid nitrogen before hydrogen analysis, see Figure 5, *a*.

A major challenge is to quickly dissipate the welding heat from the sample, otherwise hydrogen will immediately escape at higher temperatures and falsify the measurement. For this purpose, the sample is welded in a water-cooled device that allows the sample to be removed within seconds after welding (Figure 5, *b* and *c*). The hydrogen is then quantified using carrier gas hot extraction (CGHE), as described in [19, 20]. Similarly, the fractured implant samples are analyzed for residual hydrogen content by CGHE. In addition, the CGHE measurements provide a starting point for the calculation of pre- or post-heating temperatures to remove hydrogen after welding [21].

CONCLUSIONS AND OUTLOOK

Hydrogen can cause delayed cracking in the weld of high-strength steel components. Modern welding processes such as mod. SA influence the heat input and thus the formation of crack critical microstructures (e.g. the HAZ) or the introduced hydrogen content. The cold crack tests have to be adapted accordingly. The following conclusions can be drawn from this study.

- For both self-restraint and externally loaded cold cracking tests, the occurring mechanical stress must be high enough to cause HAC-critical conditions. This can be achieved either by sufficient test loads and/or critical geometric conditions such as notches.
- For very high mechanical strength (especially high-strength low-alloyed steels with yield strength > 800 MPa), the available plate thickness can be a problem for sufficient cold cracking testing. On the one hand, for the self-restraint (e.g. TEKKEN) cold cracking tests, a minimum plate thickness is necessary to reproduce realistic restrain conditions. On the other hand, externally loaded cold cracking tests may require a minimum plate thickness for further machining of samples like in the case of the implant pin geometry.
- Advanced weld processing (e.g. conventional vs. mod. SA) can result in completely different cold crack resistance for similar welding conditions (as shown in [7, 18] and Section 3.2). The reason for this is, among other things, the changed weld seam geometry and welding run sequence, which affects the diffusion path length for the hydrogen. This must be considered when evaluating the test results.
- The determination of the hydrogen concentration (e.g. for implant or ISO 3690 tests) by CGHE is strongly recommended, as this is the only way to quantify the hydrogen. Further determination of diffusion coefficients is of great importance for welding practice, e.g. to derive holding times for hydrogen annealing, e.g. according to [21].

REFERENCES

1. Gliner, R.E. (2011) Welding of advanced high-strength sheet steels. *Weld. Int*., 25(5), 389–396, 2011. DOI: https://doi.org/10.1080/09507116.2011.554234
2. EN 1011-2:2001: Welding — Recommendations for welding of metallic materials.
3. Villalobos, J.C., Del-Pozo, A., Campillo, B. et al. (2018) Microalloyed steels through history until 2018: Review of chemical composition, processing and hydrogen service. *Metals*, 8(**5**), 351. DOI: https://doi.org/10.3390/met8050351
4. Zhang, L., Kannengiesser, T. (2016) HAZ softening in Nb–, Ti– and Ti+ V-bearing quenched and tempered steel welds. *Weld. World*, 60(**2**), 177–184. DOI: https://doi.org/10.1007/s40194-016-0299-7
5. Grabke, H.J., Riecke, E. (2000) Absorption and diffusion of hydrogen in steels. *Mater. Technol*., 34(**6**), 331–342.
6. Zimmer, P, Seeger, D.M., Boellinghaus, T. (2005) Hydrogen permeation and related material properties of high strength structural steels. In: *High strength steels for hydropower plants*. Verlag der Technischen Universität Graz, Austria, **17**, 1–18.
7. Schaupp, T., Rhode, M., Yahyaoui, H., Kannengiesser, T. (2020) Hydrogen-assisted cracking in GMA welding of high-strength structural steels using the modified spray arc process. *Weld. World*, **64**, 1997–2009. DOI: https://doi.org/10.1007/s40194-020-00978-0
8. Schaupp, T., Rhode, M., Kannengiesser, T. (2018) Influence of welding parameters on diffusible hydrogen content in high-strength steel welds using modified spray arc process. *Weld. World*, 62(**1**), 9–18. DOI: https://doi.org/10.1007/s40194-017-0535-9
9. Kannengiesser, T., Boellinghaus, T. (2013) Cold cracking tests — An overview of present technologies and applications. *Weld. World*, **57**, 3–37. DOI: https://doi.org/10.1007/s40194-012-0001-7
10. ISO 17642-1:2004: Destructive tests on welds in metallic materials — Cold cracking tests for weldments — Arc welding processes. Pt 1: *General*.
11. ISO 17642-2:2005: Destructive tests on welds in metallic materials — Cold cracking tests for weldments — Arc welding processes. Pt 2: *Self-restraint tests*.
12. ISO 17642-3:2005: Destructive tests on welds in metallic materials — Cold cracking tests for weldments — Arc welding processes. Pt 3: E*xternally loaded tests*.
13. ISO 3690:2018: *Welding and allied processes — Determination of hydrogen content in arc weld metal*.
14. Kromm, A., Thomas, M., Liepold, P. et al. (2011) Influence of welding and testing parameters for hot cracking assessment of high-strength welding consumables. *Fortschrittsberichte der Materialforschung und Werkstofftechnik*, **12**, 357–365. Shaker Verlag, Düren, Germany.
15. Rhode, M., Kromm, A., Mente, T. et al. (2024) Component test for the assessment of delayed hydrogen-assisted cracking in thick-walled SAW joints for offshore applications. *Weld. World*, **68**, 621–634. DOI: https://doi.org/10.1007/s40194-023-01658-5
16. Tasak, E., Ziewiec, A., Adamiec, J.A. (2011) The role of hydrogen in weld cracking processes — A new look at the problem. *Weld Int*. 25(**6**), 409–414. DOI: https://doi.org/10.1080/09507111003655200
17. Schwenk, C., Kannengiesser, T., Rethmeier, M. (2008) Restraint conditions and welding residual stresses in self-restrained cold cracking tests. In: *Proc. of the 8th Inter. Conf. on Trends in Welding, Pine Mountain, USA, 2008*, 766–771. ASM International. DOI: https://doi.org/10.1361/cp2008twr766
18. Schaupp, T., Ernst, W., Spindler, H., Kannengiesser, T. (2020) Hydrogen-assisted cracking of GMA welded 960 MPa grade

high-strength steels. *Int. J. Hydro Energ*., **45**, 20080–20093. DOI: https://doi.org/10.1016/j.ijhydene.2020.05.077
19. Rhode, M., Schaupp, T., Muenster, C. et, al. (2019) Hydrogen determination in welded specimens by carrier gas hot extraction — A review on the main parameters and their effects on hydrogen measurement. *Weld. World,* **63**, 511–526. DOI: https://doi.org/10.1007/s40194-018-0664-9
20. Rhode, M., Mente, T., Kannengiesser, T. (2024) Parameters and challenges for reliable hydrogen determination in welded joints by carrier gas hot extraction. *The Paton Welding J*., **4**, 3–10. DOI: https://doi.org/10.37434/tpwj2024.04.01
21. Mente, T., Boellinghaus, T., Schmitz-Niederau, M. (2012) Heat treatment effects on the reduction of hydrogen in multi-layer high strength weld joints. *Weld. World*, 56(**7–8**), 26–36. DOI: https://doi.org/10.1007/BF03321362

ORCID
M. Rhode: 0000-0003-4490-4688,
T. Mente: 0009-0007-8325-9657,
T. Kannengießer: 0000-0002-8513-2429,
T. Schaupp: 0000-0001-9069-8294
A. Zavdoveev: 0000-0003-2811-0765

CONFLICT OF INTEREST
The Authors declare no conflict of interest

CORRESPONDING AUTHOR
M. Rhode
Bundesanstalt für Materialforschung und -prüfung (BAM), Berlin, Germany
E-mail: michael.rhode@bam.de

SUGGESTED CITATION
M. Rhode, T. Mente, T. Kannengießer, T. Schaupp (2024) Challenges for testing hydrogen-assisted cold cracking in weld seams of high-strength steel grades. *The Paton Welding J*., **8**, 3–9.
DOI: https://doi.org/10.37434/tpwj2024.08.01

JOURNAL HOME PAGE
https://patonpublishinghouse.com/eng/journals/tpwj

Received: 21.05.2024
Received in revised form: 09.07.2024
Accepted: 26.08.2024

DOI: https://doi.org/10.37434/tpwj2024.08.02

MECHANICAL PROPERTIES OF THE REACTION-DIFFUSION BONDING OF THE HEAT-RESISTANT NICKEL-BASED ALLOY ChS70VI

V.E. Mazurak, M.O. Cherviakov, T.M. Kushnaryova, I.R. Volosatov

E.O. Paton Electric Welding Institute of the NASU
11 Kazymyr Malevych Str., 03150, Kyiv, Ukraine

ABSTRACT

The joint of the heat-resistant nickel-based alloy ChS70VI, obtained by the method of reaction-diffusion bonding during the formation of a weld by the melt of the heat-resistant nickel-based alloy with zirconium as a depressant is considered. The microstructures and concentration distribution of all chemical elements through the joint zone (with a gap width of ~20 μm and 50 μm) after the formation of the weld and subsequent heat treatment were analyzed. It is shown that the selected mode of heat treatment allows significantly reducing the amount of zirconium-rich eutectic phases (they are more easily melted, with a melting temperature of 960 °C), which increases the heat resistance of the joint. During heat treatment, the process of diffusion takes place, and the concentration of chemical elements in the weld is close to corresponding concentrations in the base alloy. Mechanical tests showed sufficiently high strength properties of the joint at temperatures up to 1100 °C. It was established that at the test temperature of 750°C, the strength of the joint is at the level of 95–98 % of ultimate strength of the base alloy.

KEYWORDS: heat-resistant nickel-based alloys, microstructure, mechanical properties, reaction-diffusion bonding, ChS70VI alloy, contact-reactive fusion, transient liquid phase bonding

INTRODUCTION

At present heat-resistant nickel-based alloys are an integral part in the field of construction of gas-turbine engines and power gas-turbine units. The good prospects and scope of application of these alloys directly depend on the possibilities of manufacturing concrete parts and structures of a complex shape that, in its turn, is due to the ability to join the respective alloys by permanent joints. A feature of heat-resistant nickel-based alloys is their extremely limited joinability by the traditional fusion welding methods. Such negative factors as higher sensitivity of the welded joints to hot cracking and local fracture in the overheating zone, lead to a considerable lowering of the welded joint properties [1]. Fusion welding, diffusion bonding and brazing are known as the main methods of repair and/or joining of the heat-resistant nickel-based alloys [2]. Each of these methods has certain limitations, so that the studies performed in this area both by local scientists and abroad remain to be relevant.

The method of reaction-diffusion bonding (RDB) in vacuum allows producing joints without autonomous melting of the base metal, eliminating the risk of macro- and microcrack formation, preserving the initial structure and avoiding the negative influence of the thermal cycle on physico-mechanical characteristics of the material being joined [3].

RDB method is based on formation of a liquid phase saturated with depressant (for Ni–Cr–Co system) and its penetration into a fixed gap between the planes being joined with its further crystallization and diffusion dissolution during heat treatment. The phenomenon of contact-reactive fusion of dissimilar metals is used to produce the liquid phase [4]. The liquid phase forms beyond the limits or directly near the gap between the parts being joined, as a result of contact-reactive fusion of the heat-resistant nickel-based alloy and depressant, and at certain bonding temperature it feels the gap under the action of the capillary forces. Zirconium in the form of foil was used as the depressant. In this capacity zirconium was studied and used in filler materials for brazing heat-resistant nickel alloys [5, 6].

THE OBJECTIVE OF THE WORK

is testing the method of reaction-diffusion bonding of heat-resistant nickel-based alloy ChS70-VI with a considerable area of weld edges, metallographic studies and assessment of mechanical characteristics of the produced joints.

INVESTIGATION MATERIALS AND METHODS

Investigations were conducted on joints of ChS70-VI alloy, which is the representative of the class of heat-resistant nickel-based cast alloys, and has been used for a long time already for manufacturing the hot section parts in power gas-turbine units. Blanks of 55×30×12 mm dimensions, cut out of one blank from ChS70-VI alloy were used to make the joints (Figure 1). Chemical composition of ChS70-VI alloy is given in Table 1. The gap of overall area of 660 mm^2

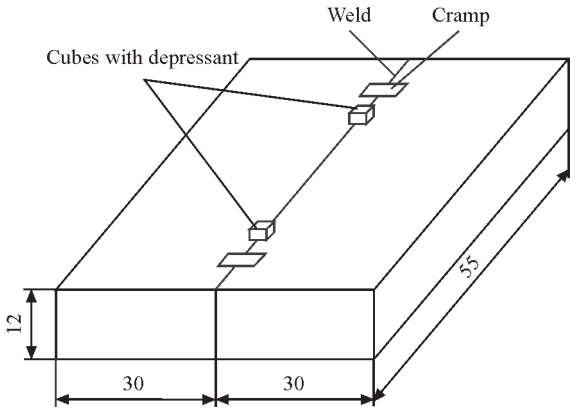

Figure 1. Scheme of assembly of a butt joint of ChS70-VI alloy

Table 1. Chemical composition of ChS70-VI alloy (TU 1-809-1040–96)

Weight fraction of elements, %								
C	Cr	Co	W	Mo	Al	Ti	Nb	Ni
0.06 0.12	15.0 16.7	10.0 11.5	4.5 6.0	1.5 2.5	2.4 3.2	4.2 5.0	0.1 0.3	Base

was filled with the liquid phase (based on Ni–Cr–Co system), saturated with zirconium. Before conducting RDB, the blanks were annealed at the temperature of 1050 °C for 2 h in vacuum. The abutted surfaces of the specimen were ground, and then butt joints were made. The uniformity of the fixed gap along the entire length of the specimen was provided by cramps from nichrome alloy, which were welded on the specimen surface by resistance spot welding. The cubes with zirconium foil were placed on top above the weld. They were also attached by resistance spot welding. The process of RDB of the assembled specimen (Figure 2, *a*) was conducted in a vacuum furnace in the following mode: heating up to the temperature of 1200 °C at the heating rate of 30–40 °C/min; soaking for 10 min, further cooling at the rate of 50–60 °C/min.

The appearance of the blank after RDB process showed complete wetting and filling of the gap along the entire length of the weld being made, with formation of grooves. Then, a piece of the joint was cut out

Figure 3. General view of MTS-810 testing machine

of the blank to conduct metallographic studies (Figure 2, *b*), and the rest of the specimen was subjected to diffusion annealing by the following mode: 1100 °C, soaking for 1 h; 1150 °C, soaking for 5 h. After that, part of the specimens were cut out for mechanical testing, and the rest of the joint metal was subjected to heat treatment by the following mode: 1050 °C, soaking for 3.5 h; aging at 860 °C, soaking for 17 h.

Microstructural investigations were conducted, using microhardness meter PMT-3 with 50 g load. Mechanical properties of the produced joints and base metal of ChS70-VI alloy were studied using MTS-810 servohydraulic machine (Figure 3). It consists of the following components: MTS 661.20F-02 dynamometer with axial load of up to 50 kN with the resolution of up to 0.1 N; MTS 632.53F-11 extensometer for operation with higher and high temperatures with 25 mm base and measurement resolution of 0.00001 %; MTS 653 Furnace with maximal temperature of specimen heating at testing of up to 1100 °C and three-zone monitoring with up to 5 °C tempera-

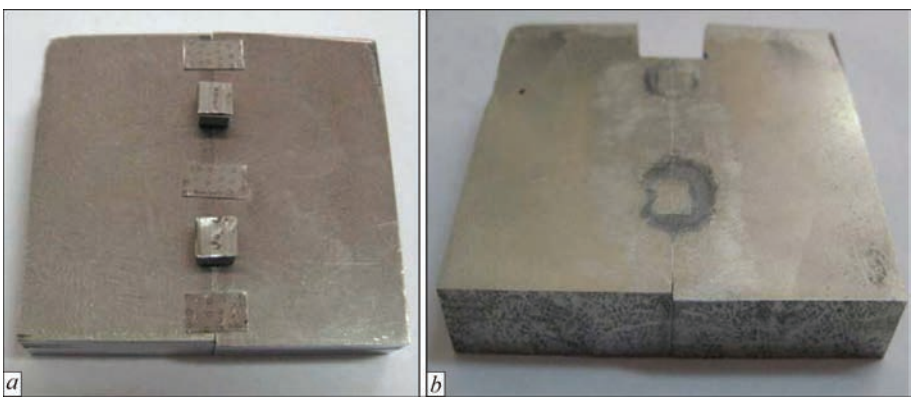

Figure 2. Specimen of a butt joint of ChS70-VI alloy before (*a*) and after joint formation at the temperature of 1200 °C for 10 min (*b*)

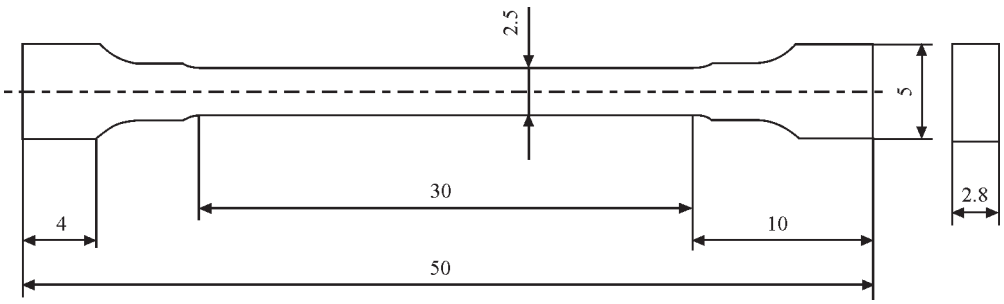

Figure 4. Specimen for short-time strength testing at room and high temperatures

ture gradient. Testing for short-term strength of the base metal and butt welded joints was conducted on flat specimens (Figure 4). Geometrical dimensions of the working length relative to the cross-sectional area and the initial length correspond to DSTU [7, 8] for room and higher temperatures, respectively. The strain rate during testing was equal to 0.00067 s^{-1}, which corresponds to the standards.

To conduct metallographic examinations the specimens were cut out normal to the weld. Polishing was performed using diamond paste and chromium oxide (III). Oxidation in air at the temperature of 350–400 °C was conducted to study the microsections in Neophot-32 optical microscope. The distribution of chemical elements was investigated by the method of local microX-ray spectral analysis, using energy-dispersive spectrometer Oxford Instruments X-max (80 mm^2), under the guidance of INCA software. The locality of the measurements was not greater than 1 μm. Shooting of the microstructures was conducted using scanning electron microscope TescanMira 3 LMU in backscattered electrons (BES), which allows examination of the microsections without chemical etching.

RESULTS AND DISCUSSION

METALLOGRAPHIC INVESTIGATIONS

Figure 5 shows the joint microstructures in the condition after the gap filling with the liquid phase and after diffusion annealing. Microhardness distribution across the weld before and after diffusion annealing (Figure 6) shows that the hardness of weld metal after conducting the full heat treatment became close to base metal hardness of 423 *HV* 0.05. However, in some regions of the weld of 50 μm width phases with hardness of both 480 *HV* 0.05 and 321 *HV* 0.05 remained after annealing. In the microstructures in Figure 5 one

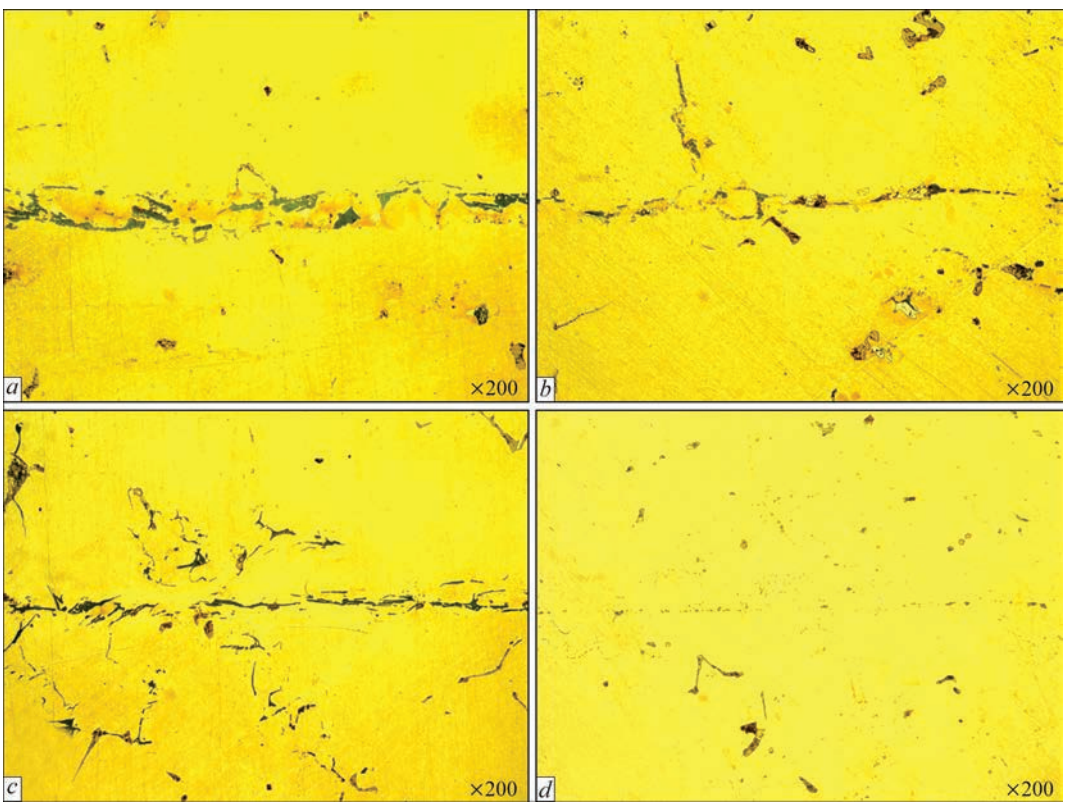

Figure 5. Microstructure (×200) of a butt joint of ChS70-VI alloy with gap width of ~50 μm (*a*, *b*) and ~10 μm (*c*, *d*), filled with liquid phase saturated with zirconium in the condition after heating up to 1200 °C, soaking for 10 min (*a*, *c*) and heat treatment at the temperature of 1100 °C, soaking for 1 h and 1150 °C, soaking for 5 h (*b, d*)

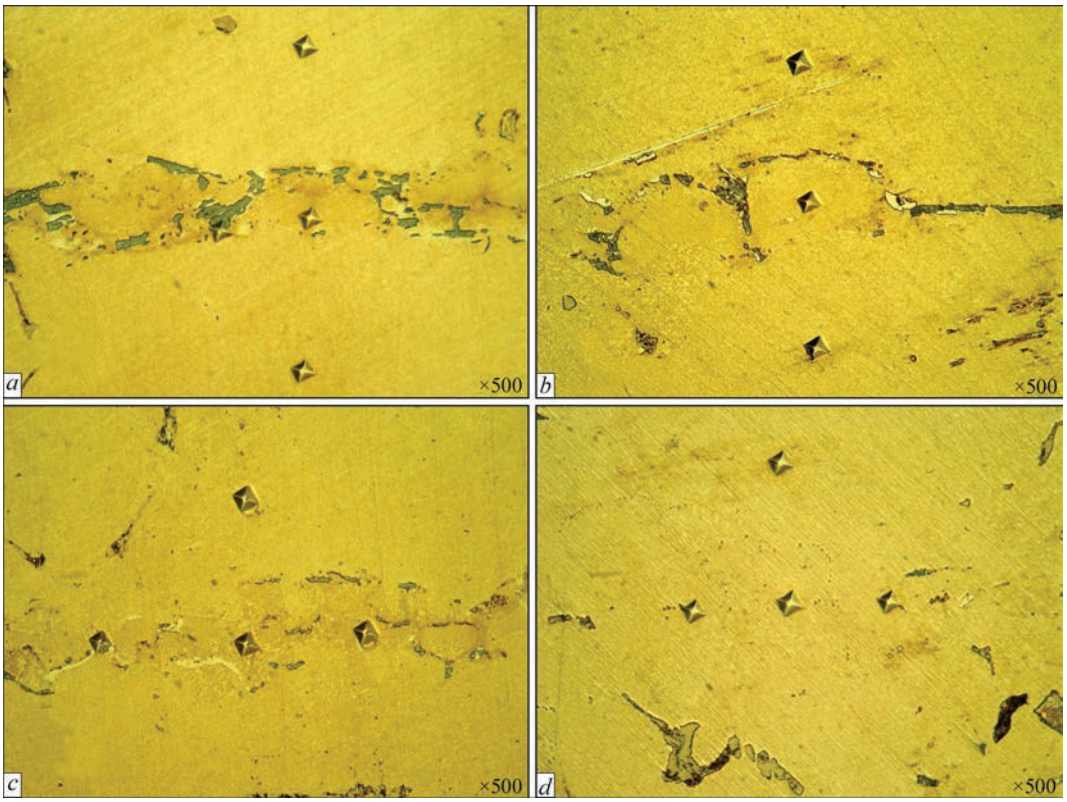

Figure 6. Measurement of *HV* microhardness (*P* = 50 g) across the weld 50 μm (*a, b*) and 20 μm wide (*c, d*) of the joint of ChS70-BI alloy, filled with the liquid phase saturated with zirconium in the condition after heating up to 1200 °C, soaking for 10 min (*a*, *c*) and heat treatment at the temperature of 1100 °C, soaking for 1 h and 1150 °C, soaking for 5 h (*b*, *d*) (×500)

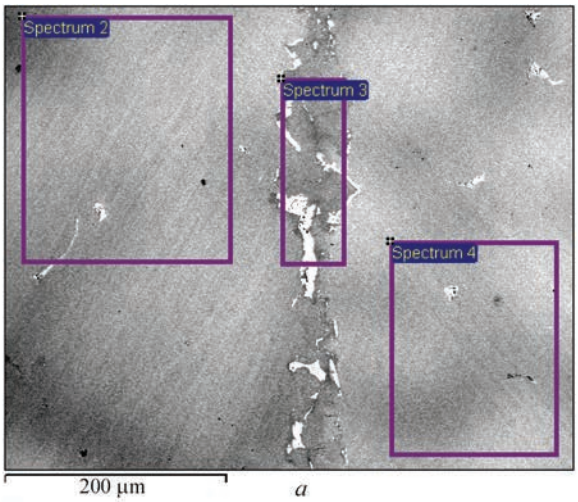

Spectrum	In the initial condition (1200 °C, 10 min)									
	Chemical element, wt.%									
	Al	Ti	Cr	Co	Ni	Zr	Nb	Mo	W	Total
2	2.64	3.13	13.23	8.74	66.52		0.19	1.44	4.11	100
3	2.65	4.21	12.46	7.05	63.50	1.79	0.71	2.52	5.11	100
4	2.91	3.81	13.27	8.43	66.49		0.44	1.73	2.93	100

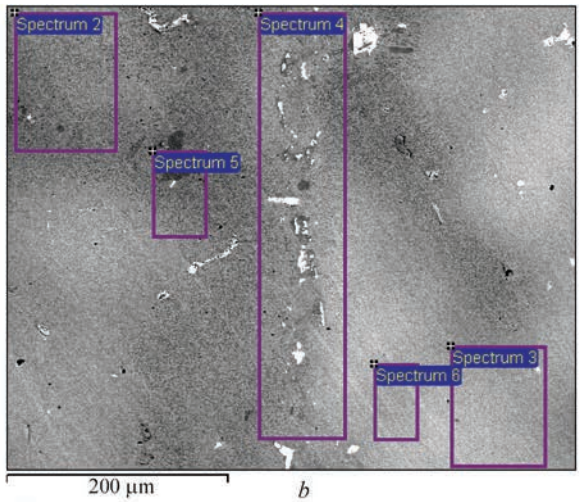

Spectrum	After diffusion annealing (1100 °C, 1 h + 1150 °C, 5 h)									
	Chemical element, wt.%									
	Al	Ti	Cr	Co	Ni	Zr	Nb	Mo	W	Total
2	2.60	4.28	13.78	9.24	64.80			1.89	3.41	100
3	2.40	3.56	14.7	9.79	64.34			1.83	3.38	100
4	2.83	3.78	14.09	9.03	64.22	1.24		1.57	3.24	100
5	2.89	5.3	12.44	8.65	67.49			1.46	1.77	100
6	2.54	3.27	14.86	9.77	62.20			1.56	5.80	100

Figure 7. Chemical composition of the weld zone (50 μm wide) and near-weld zone of the joint of ChS70-VI alloy, produced with application of zirconium depressant in the condition after formation of the joint at the temperature of 1200 °C, soaking for 10 min (*a*) and after homogenizing annealing at the temperature of 1100 °C, soaking for 1 h and 1150 °C, soaking for 5 h (*b*)

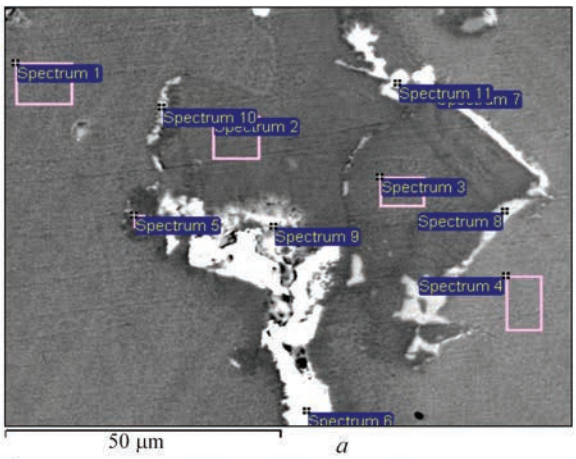

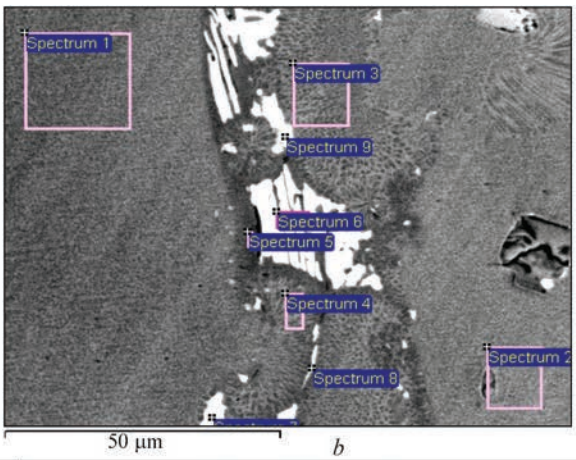

Spect.	Chemical element, wt.%									
	Al	Ti	Cr	Co	Ni	Zr	Nb	Mo	W	Total
1	2.80	3.35	12.82	8.48	67.12		0.01	1.45	3.96	100
2	3.10	3.71	12.73	8.21	67.79	0.55		1.45	2.46	100
3	2.88	3.79	12.96	8.08	67.87	0.55		1.35	2.52	100
4	2.75	3.05	13.34	8.63	65.67			2.07	4.49	100
5	3.48	5.62	7.58	6.87	73.05	1.13		0.66	1.61	100
6		2.08	35.89	1.51	3.26	1.39	1.91	23.53	30.44	100
7		1.29	37.96	1.78	17.83	1.12	0.80	14.96	24.25	100
8	0.52	1.30	1.97	5.17	63.48	26.63			0.93	100
9	3.27	12.67	6.44	5.57	60.11	2.40	3.22	1.60	4.72	100
10	0.79	2.11	6.87	5.48	60.40	22.04	1.11	1.20		100
11	0.21	1.07	49.87	1.68	5.79	0.82		15.77	24.79	100

Spect.	Chemical element, wt.%									
	Al	Ti	Cr	Co	Ni	Zr	Nb	Mo	W	Total
1	2.66	4.08	12.7	7.84	68.7			1.67	2.36	100
2	2.74	5.33	12.41	7.51	63.23	0.55	1.00	2.53	4.7	100
3	3.24	4.41	11.29	7.58	69.51			1.29	2.68	100
4	3.18	4.21	11.51	7.61	69.17	0.44		1.48	2.4	100
5	2.97	4.98	9.62	8.64	69.37	1.29	0.73	0.87	1.54	100
6	0.35	1.20	15.49	4.11	51.8	18.75	1.06	4.05	3.21	100
7	0.49	1.33	1.76	5.08	62.7	27.5	1.13			100
8	1.23	2.27	7.22	6.96	63.68	16.33	1.24	1.07		100
9	0.55	8.67	1.49	1.31	23.79	50.31	9.75		4.14	100

Figure 8. Chemical composition of individual phases of the weld and near-weld zone of the joint of ChS70-VI alloy, produced with application of zirconium in the condition after joint formation at the temperature of 1200 °C, soaking for 10 min

can clearly see that the applied heat treatment allows practically "resorbing" the weld 10–20 μm wide.

Figure 7 shows the structure and distribution of the concentration of all the elements through the zone of the joint ~ 50 μm wide in the condition after joint formation (1200 °C – 10 min) and after heat treatment (1100 °C – 1h + 1500 – 5 h). Studies were performed on a specimen with weld width of ~ 50 μm. One can clearly see that during heat treatment at 1100 °C for 1 h + 5 h at 1150 °C (which is just homogenizing) the weld width is noticeably reduced, the chemical composition and structure of the weld zone become close to that of the base material. It was established that the overall concentration of zirconium in the weld changed from 1.79 to 1.24 wt.%, i.e. zirconium diffusion into the base metal took place. Complete diffusion of zirconium from the weld into the base metal at the considered weld width requires not less than 20 h of homogenizing heat treatment. The final structure of the joint and, consequently, the strength of the formed joint depend on completeness of running of the processes of equalizing diffusion.

Comparative analysis of chemical composition of phases in individual regions of the joint zone before (Figure 8) and after (Figure 9) heat treatment on the studied length of 100 μm shows that the quantity of zirconium-rich phases (~22–26 wt.%, white phase) is markedly reduced. This phase represents the remains of the eutectic phase located between the common grains formed at RDB. Only small point islets of this phase remain after heat treatment. Here, the near-boundary zone of the weld has regions with zirconium content of 3–4 wt.% at 30–50 μm distance from the weld. (Ti + Zr) phase is observed in the weld and near-boundary zone both before and after heat treatment, with a high content of titanium (57.47 % Ti + 7.5 % Zr, 48.26 % Ti + 4.12 % Zr and 52.67 % Ti + 3.83 % Zr). Comparing the microstructures of the joint zone before and after vacuum annealing (Figures 8 and 9) one can come to the conclusion that a strengthening phase precipitated in the weld and its size is somewhat smaller than in the base metal. Judging from the nature of the results of X-ray spectral microanalysis (XSMA) phases enriched in W, Mo and Cr precipitate on the boundaries of crystallized grains. With the highest probability these are carbides of $Me_{23}C_6$ type [9, 10], precipitation of which is due to the alloy chemical composition during heat treatment.

Presence of Zr-rich phases in the weld (Figure 9) points to the completeness of running of Zr dissolution process in the alloy matrix, and the

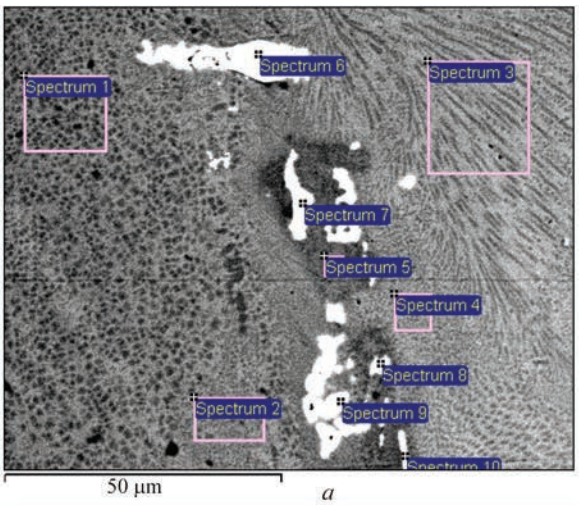

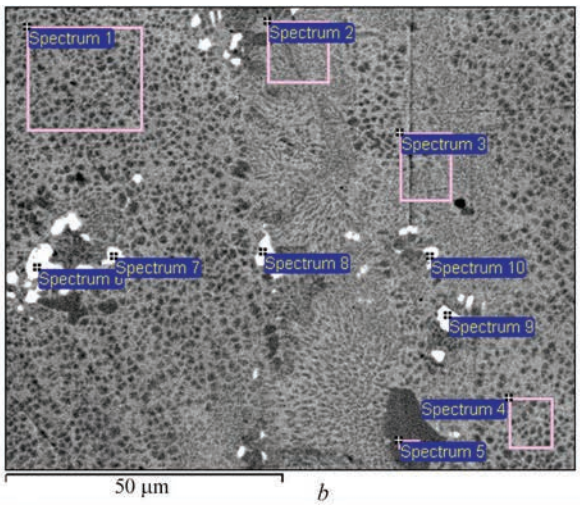

Spect.	Chemical element, wt.%								
	Al	Ti	Cr	Co	Ni	Zr	Mo	W	Total
1	2.8	4.39	14.01	8.77	66.34		1.57	2.1	100
2	2.91	3.65	14.69	8.74	64.29	0.69	1.68	3.36	100
3	2.37	3.48	14.57	9.32	63.45	0.51	2.02	4.28	100
4	2.85	3.34	14.35	9.03	64.39		2	4.04	100
5	3.14	5.26	10.78	8.8	67.15	1.47	1.19	1.64	100
6	1.01	57.49	0.89	0.66		7.5	2.79	5.82	100
7		1.5	2.03	5.88	60.62	29.03			100
8	1.17	2.08	3.12	6.64	61.53	24.4			100
9		6.78	1.99	1.5	5.72	73.78			100
10	0.65	1.92	4.63	6.25	61.55	24.02			100

Spect.	Chemical element, wt.%								
	Al	Ti	Cr	Co	Ni	Zr	Mo	W	Total
1	2.84	4.09	14.19	8.92	65.84		1.29	2.83	100
2	2.84	4.15	14.1	8.63	66.32		1.24	2.73	100
3	2.71	3.62	14.79	9.34	64.83		1.6	3.11	100
4	3.03	4.1	13.05	8.55	66.05	0.54	1.2	3.48	100
5	5.08	7.92	3.42	5.56	75.0	1.09		1.93	100
6	0.68	52.67	1.28			3.83	4.98	16.81	100
7		48.26	2.67	1.63	5.46	4.12	4.53	15.1	100
8	0.89	1.92	3.01	5.69	62.95	24.41			100
9		2.89	28.33	2.67	11.44	1.5	21.87	29.5	100
10	1.79	2.55	8.2	8.02	62.29	13.75	0.62	2.77	100

Figure 9. Chemical composition of the weld and near-weld zone of the joint of ChS70-VI alloy produced using zirconium, in the condition after homogenizing annealing in vacuum at the temperature of 1100 °C, soaking for 1 h and 1150 °C, soaking for 5 h

Table 2. Results of short-time strength testing of specimens of ChS70-VI alloy

Specimen	Specimen number	σ_t, MPa	$\sigma_{0.2}$, MPa	δ, %	T_{test}, °C	Fracture site
Base metal	1*	714.5	621.5	4.9	20	–
	2*	727.2	565.9	2.7	750	–
Joint	3*	701.9	657.3	2.1	20	Base metal
	4*	683.8	564.6	2.3	750	Weld
	5**	696.7	633.2	1.3	20	
	6**	781.3	656.8	6.3	20	Base metal
	7**	792.4	572.8	5.6	700	
	8**	729.6	575.2	2.7	800	Weld
	9**	526.1	383.3	12.7	900	
	10**	322.9	249.1	14.5	1000	
	11**	148.5	123.9	14	1100	Base metal
Base metal	32**	856.6	644.2	6.4	20	–
	33**	780.8	543.9	4.5	700	–
	34**	760.4	527.9	1.9	800	–
	35**	541.2	531.1	1.5	900	–
	36**	286.4	248.8	2.2	1000	–
	37**	140.7	121.9	8.3	1100	–

*Heat treatment: 1100 °C – 1 h + 1150 °C – 5 h.
**Heat treatment: 1100 °C – 1 h + 1150 °C – 5 h + 1050 °C – 3.5 h + 860 °C – 17 h.

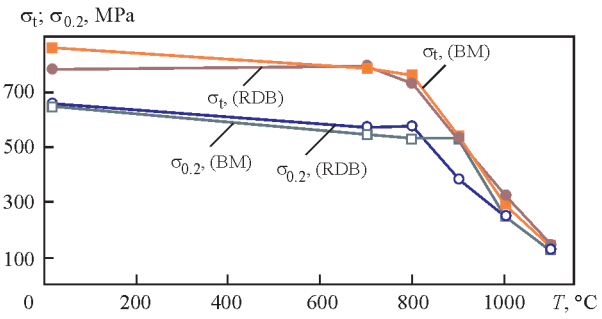

Figure 10. Temperature dependencies of ultimate strength σ_t and yield limit $\sigma_{0.2}$ of the base metal and butt specimens from ChS70-VI alloy produced by RDB method. Heat treatment is the same for all the specimens: 1100 °C – 1 h + 1150 °C – 5 h + 1050 °C – 3.5 h + 860 °C – 17 h

need to correct the joint gap width and the time of heat treatment duration.

MECHANICAL TESTING

Butt joints produced by RDB, before mechanical testing, were subjected to homogenizing annealing by the mode of 1100 °C for 1 h + 1150 °C for 5 h. Part of the specimens was additionally treated by two-stage aging at 1050 °C for 3.5 h + aging at 860 °C for 17 h. Testing was conducted in air at the following temperatures: 20, 750, 900, 1000, 1100 °C. The results are shown in Table 2. Specimens which additionally passed two-stage aging demonstrated a slight improvement of short-term strength and higher ductility at mechanical testing. For clarity, the data are also presented in the form of temperature dependencies of σ_t and $\sigma_{0.2}$ (Figure 10) and load diagrams (Figure 11).

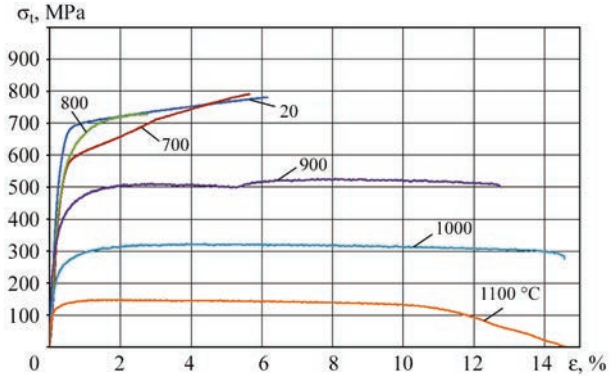

Figure 11. Load diagrams derived during short-time tensile testing of butt specimens from ChS70-VI alloy produced by RDB method with the following heat treatment: 1100 °C – 1 h + 1150 °C – 5 h + 1050 °C – 3.5 h + 860 °C – 17 h

Results of mechanical testing for short-term strength demonstrated a rather high level of weld strength, which is comparable with base metal level at the same heat treatment. Ultimate strength of RDB joints was equal to 91–100 % of that of the base metal, and the yield limit of RDB joints was equal to 95–100 % of that of the base metal. Figure 12 shows the broken specimens after testing. On part of the specimens with the joint the fracture ran through the base metal and not through the weld. This data indicate that homogenizing annealing at 1100 °C for 1 h + 1150 °C for 5 h led to dissolution of brittle intermetallics of zirconium, as well as diffusion of zirconium proper into the base metal, which is confirmed by metallographic examinations. The high strength and ductility (Figure 10, Figure 11) of RDB joints at test tempera-

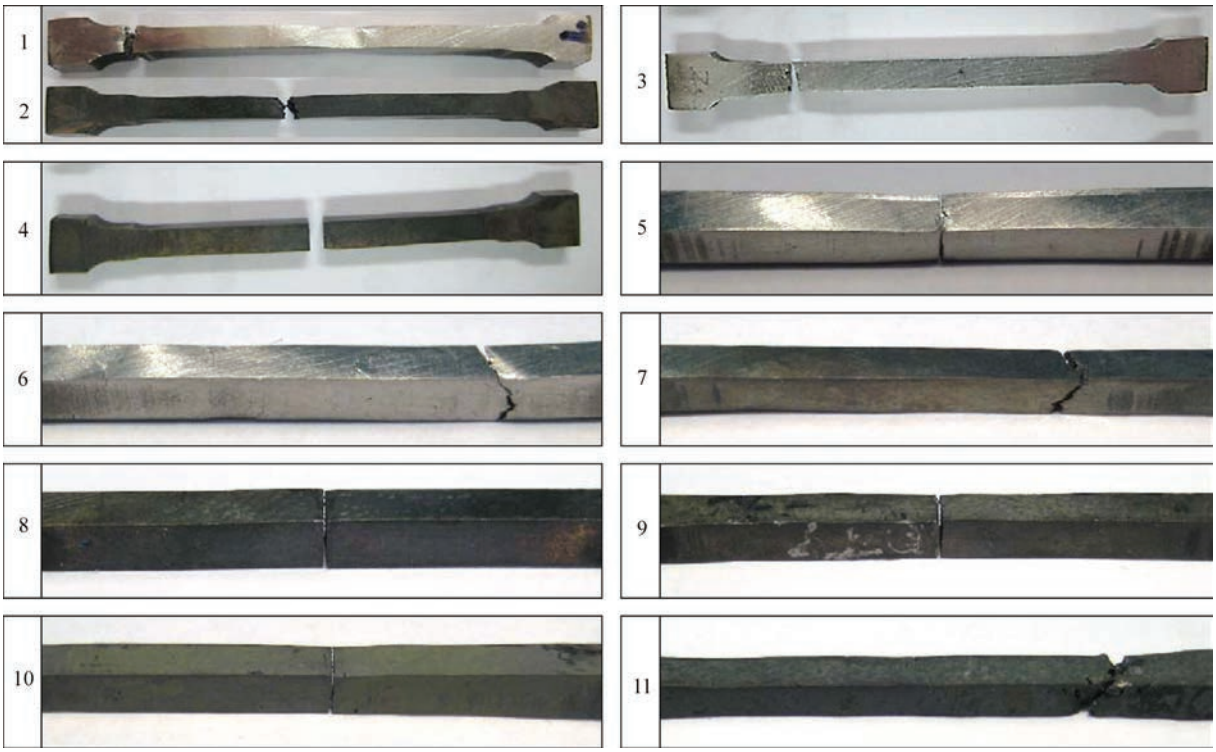

Figure 12. Appearance of specimens after destruction. Numbers on the left correspond to specimens shown in Table 2

tures of 1000 and 1100 °C (specimens 10 and 11), are also indicative (together with X-ray spectral chemical microanalysis) of the intensity of running of equalizing diffusion processes in the joint zone (weld and near-weld zone) and lowering of zirconium concentration in the weld during heat treatment. The lowest melting eutectic phases of intermetallics of Ni–Zr system have melting temperature of 960 °C ($NiZr_2$) and 1010 °C (NiZr) [11]. In the joints with weld width greater than 50 μm, the remains of such phases within the grain boundaries in the weld center can markedly lower their high-temperature strength.

CONCLUSIONS

A study was conducted with production of a butt joint of heat-resistant nickel-based ChS70-VI alloy by filling the gap with butt surface area of 660 mm^2 with the liquid phase formed during contact fusion of sintered powder of heat-resistant austenitic nickel-chromium alloy and metal of zirconium foil depressant. It is shown that at the temperature of 1200 °C the liquid phase has sufficient flowability and completely fills the joint gap.

Analysis of the structures and distribution of chemical elements in the base metal, weld and near-weld zone of the joint before and after homogenizing annealing revealed that the process of dissolution of some zirconium-rich intermetallic phases takes place, as well as carbide phase precipitation on the grain boundary. Concentrations of chemical elements in the weld are close to those in the base metal.

It is established that the strength properties of the joints at test temperatures of 750 °C correspond to 95–98 % of base alloy ultimate strength. Relatively high heat resistance of RDB joint has been achieved right up to the temperature of 1100 °C (maximal temperature of testing machine furnace).

REFERENCES

1. Kablov, E.N. (2001) *Cast blades of gas turbine engines (Alloys, technologies, coatings)*. Moscow, MISIS [in Russian].
2. Zhang, Y., Cheng, Y., He, N. et al. (2023) Microstructural characterization of TLP bonded joints of Mar-M247 superalloys with Ni–Cr–B interlayer. *Mater. Charact*., **198**, 112766 DOI: https://doi.org/10.1016/j.matchar.2023.112766
3. Nesmikh, V.S., Yushchenko, K.A., Kushnaryova, T.M. (2005) *Method of diffusion-reactive joining of metals and alloys.* Pat. Ukraine **73308** [in Ukrainian].
4. Lashko, S.V., Lashko, N.F. (1988) *Soldering of metals.* Moscow, Mashinostroenie [in Russian].
5. Kvasnytskyi, V.V., Myalnitsa, G.F., Matvienko, M.V. et al. (2019) Investigation of interaction of Ni_3Al-based alloy with interlayers of different alloying systems for TLP-bonding. *The Paton Welding J.,* **8**, 12–17. DOI: https://doi.org/10.15407/tpwj2019.08.03
6. Maksymova, S.V., Voronov, V.V., Kovalchuk, P.V. (2017) Brazing filler metal without boron and silicon for brazing of heat-resistant nickel alloy. *The Paton Welding J.*, **8**, 12–17. DOI: doi.org/10.15407/tpwj2017.08.02
7. (2020) DSTU ISO 6892-1:2019: *Metallic materials. Tensile testing.* Pt 1: Method of test at room temperature. Kyiv, SE UkrNDNTs [in Ukrainian].
8. (2021) DSTU ISO 6892-2:2020: *Metallic materials. Tensile testing.* Pt 2: Method of test at elevated temperature. Kyiv, SE UkrNDNTs [in Ukrainian].
9. Kishkin, S.T., Stroganov, G.B., Logunov, A.V. (1987) *Casting high-temperature nickel-based alloys.* Moscow, Mashinostroenie [in Russian].
10. Lashko, N.F., Zaslavskaya, L.V., Kozlova, M.N. et al. (1978) *Physico-chemical phase analysis of steels and alloys.* Moscow, Metallurgiya [in Russian].
11. (2001) *State diagrams of binary metal systems:* Refer. Book in 3 Vol. Ed. by N.P. Lyakishev. Moscow, Mashinostroenie [in Russian].

ORCID

V.E. Mazurak: 0000-0001-8671-348X,
M.O. Cherviakov: 0000-0003-4440-7665,
T.M. Kushnaryova: 0000-0003-1920-3118,
I.R. Volosatov: 0000-0003-2593-9869

CONFLICT OF INTEREST

The Authors declare no conflict of interest

CORRESPONDING AUTHOR

M.O. Cherviakov
E.O. Paton Electric Welding Institute of the NASU
11 Kazymyr Malevych Str., 03150, Kyiv, Ukraine.
E-mail: cherviakov@paton.kiev.ua

SUGGESTED CITATION

V.E. Mazurak, M.O. Cherviakov, T.M. Kushnaryova, I.R. Volosatov (2024) Mechanical properties of the reaction-diffusion bonding of the heat-resistant nickel-based alloy ChS70VI. *The Paton Welding J.*, **8**, 10–17. DOI: https://doi.org/10.37434/tpwj2024.08.02

JOURNAL HOME PAGE

https://patonpublishinghouse.com/eng/journals/tpwj

Received: 01.11.2023
Received in revised form: 27.05.2024
Accepted: 19.08.2024

DOI: https://doi.org/10.37434/tpwj2024.08.03

MATHEMATICAL MODELLING OF DISTORTIONS AT WELDING OF LARGE VESSELS OF ALUMINIUM ALLOY

B.R. Tsaryk, O.V. Makhnenko

E.O. Paton Electric Welding Institute of the NASU
11 Kazymyr Malevych Str., 03150, Kyiv, Ukraine

ABSTRACT

The problem of calculation prediction of the overall distortions of a large vessel made of aluminium alloy during friction stir welding (FSW) is considered. A mathematical model was developed using numerical methods of thermoplasticity analysis for determining the stress-strain state during FSW, by means of which it is possible to obtain residual plastic strains (the inherent strain function parameters) for both types of welded vessel joints (longitudinal and circumferential). This makes it possible to predict the overall distortions of a large cylindrical vessel with a great number of welded joints by the approximated method of inherent strains within the limits of the theory of elasticity. The reliability of the mathematical model for determination of the residual stresses and strains at FSW of aluminium alloy is confirmed by the agreement of the calculated distribution of the residual longitudinal stresses with the data of experimental measurements. This can contribute to ensuring the necessary accuracy of predicting the overall distortions of large vessels. The developed mathematical models and calculation algorithms can be effectively used for in-process prediction of the stress-strain state during assembly welding of large cylindrical vessels made of aluminium alloys.

KEYWORDS: welded vessels, aluminium alloy, friction stir welding, plastic strains, residual stresses, mathematical modelling

INTRODUCTION

Welding technology is widely used to produce joints of large structures made of aluminium alloys, such as fuel tanks for aerospace engineering, bodies for transport mechanical engineering, etc. [1, 2]. To predict the accuracy, strength and fatigue life of such welded structures, the relevant task is to determine residual stresses and strains by calculation. The calculation prediction of the overall distortions of large structures with a great number of welded joints [3] is particularly difficult problem, and the use of aluminium alloys for such structures, as is known, significantly increases welding strains [4]. The solution of such problems requires large computing resources and a long time for computation, which complicates the use of calculation methods in practice during technological preparation of assembling and assembly welding of new structures. Recently, when manufacturing cylindrical vessels of aluminium alloys, a new friction stir welding process (FSW) began to be used. It is believed that FSW provides high quality of welded joints without such defects as pores and hot cracks, as well as a much lower level of residual stresses and strains compared to arc welding processes [1, 5]. Thus, the problem of developing effective calculation methods for in-process prediction of stress-strain state during assembly welding of large cylindrical vessels of aluminium alloys is quite relevant.

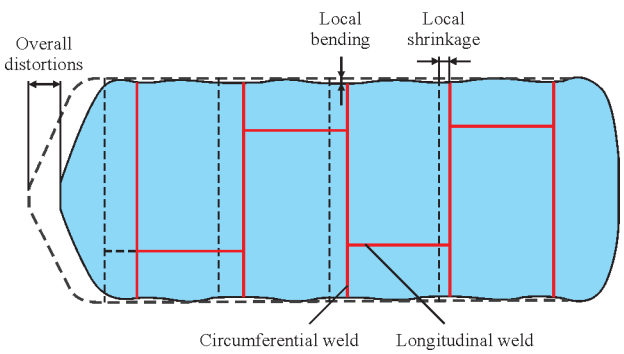

Figure 1. Scheme of distortions of a cylindrical vessel with a great number of longitudinal and circumferential welded joints

PROCEDURE FOR CALCULATED DETERMINATION OF WELDING STRAINS

To solve the problem of predicting strains in large cylindrical vessels of aluminium alloy with a great number of welds (Figure 1), a procedure of modelling welding stresses and strains is used based on the combined use of the general thermoplasticity method [6] and approximated inherent strain method [7]. By means of the thermoplasticity method, temporary and residual stresses and strains for individual welded joints are modelled. It is known that residual welding stresses and plastic strains are formed in a limited area in the welded joint zone. Therefore, the distribution of residual stresses and inherent strain function parameters can be obtained on simplified models of a welded joint of a limited size, which requires much smaller computer resources and time for calculation.

Regarding large cylindrical vessels with longitudinal and circumferential butt joints, it is advis-

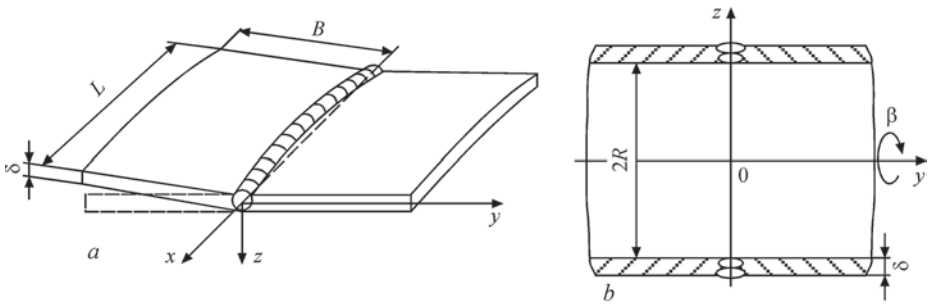

Figure 2. Determination of inherent strain function parameters: *a* — 3D model of a butt welded joint of limited size plates; *b* — 2D model of a circumferential welded joint

able to consider two types of simplified models. To determine the local residual strains (inherent strain function parameters) in the zones of longitudinal joints, the model of a butt joint of plane elements of a limited size can be used (Figure 2, *a*). In the zone of circumferential joints, to determine the residual stresses and strains (inherent strain function parameters), a simplified model in a two-dimensional formulation of a butt circumferential joint of a real size can be used, but with the assumption of a fast-moving welding heating source and "plain strain" hypothesis (Figure 2, *b*).

Then, by means of a three-dimensional model of a cylindrical vessel of a real size using the approximated method of inherent strain function in the framework of elastic formulation of the problem, the overall distortions of large welded structure from all welds are modelled.

GENERALIZED PRESENTATION OF INHERENT STRAIN FUNCTION AS A TENSOR FUNCTION

Let us present the inherent strain function as a tensor of plastic strains:

$$\Pi_{ij} = \begin{Vmatrix} \Pi_{xx} & \Pi_{xy} & \Pi_{xz} \\ \Pi_{yx} & \Pi_{yy} & \Pi_{yz} \\ \Pi_{zx} & \Pi_{zy} & \Pi_{zz} \end{Vmatrix} = \begin{Vmatrix} \varepsilon^p_{xx} & \varepsilon^p_{xy} & \varepsilon^p_{xz} \\ \varepsilon^p_{yx} & \varepsilon^p_{yy} & \varepsilon^p_{yz} \\ \varepsilon^p_{zx} & \varepsilon^p_{zy} & \varepsilon^p_{zz} \end{Vmatrix} =$$
$$= \begin{Vmatrix} \varepsilon^p_{xx} & 0 & 0 \\ 0 & \varepsilon^p_{yy} & 0 \\ 0 & 0 & -(\varepsilon^p_{xx} + \varepsilon^p_{yy}) \end{Vmatrix} = \begin{Vmatrix} \Pi_{xx} & 0 & 0 \\ 0 & \Pi_{yy} & 0 \\ 0 & 0 & -(\Pi_{xx} + \Pi_{yy}) \end{Vmatrix}, \quad (1)$$

$\varepsilon^p_{xy} = \varepsilon^p_{yx} = \varepsilon^p_{xz} = \varepsilon^p_{zx} = \varepsilon^p_{zy} = \varepsilon^p_{yz} = 0$, since the axes X and Y are the main axes for the longitudinal and transverse direction of welded joints; $\varepsilon^p_{zz} = -(\varepsilon^p_{xx} + \varepsilon^p_{yy})$ from the condition of volume preservation. If an inherent strain function along the welded joint is permanent, then $\Pi_{xx} = \varepsilon^p_{xx}(y,z)$, $\Pi_{yy} = \varepsilon^p_{yy}(y,z)$.

FORMULATION OF THE PROBLEM OF DETERMINING STRAINS OF THE CYLINDRICAL SHELL BASED ON THE TENSOR INHERENT STRAIN FUNCTION

In the cylindrical coordinate system, the tensor of full strains ε_{ij} in the welded shell will be determined by the sum of the tensor of elastic strains ε^p_{ij} and the tensor of inherent strain function Π_{ij}:

$$\varepsilon_{ij} = \varepsilon^e_{ij} + \Pi_{ij}, \ (i,j = r,\beta,z). \quad (2)$$

The components of the tensor ε_{ij} are expressed at each point (r, β, z) of the shell by three components of the displacement vector U_i (Cauchy distribution) [10]:

$$\varepsilon_{rr} = \frac{\partial U_r}{\partial r}, \ \varepsilon_{zz} = \frac{\partial U_z}{\partial z}, \ \varepsilon_{\beta\beta} = \frac{\partial U_\beta}{r\partial\beta} + \frac{U_r}{r},$$
$$\varepsilon_{rz} = \frac{1}{2}\left(\frac{\partial U_r}{\partial z} + \frac{\partial U_z}{\partial r}\right), \ \varepsilon_{r\beta} = \frac{1}{2}\left(\frac{\partial U_r}{r\partial\beta} + \frac{\partial U_\beta}{\partial r} - \frac{U_\beta}{r}\right), \quad (3)$$
$$\varepsilon_{z\beta} = \frac{1}{2}\left(\frac{\partial U_\beta}{\partial z} + \frac{\partial U_z}{r\partial\beta}\right)$$

as well as with each other by the strains compatibility equations. On the boundary surfaces, the displacement values U_i are determined by the boundary conditions of the first kind, i.e. the values ΔU_r., ΔU_β, ΔU_z.

Strains compatibility equations [10]:

$$\frac{\partial^2\varepsilon_{rr}}{\partial z^2} + \frac{\partial^2\varepsilon_{zz}}{\partial r^2} = 2\frac{\partial^2\varepsilon_{rz}}{\partial r\partial z};$$
$$\frac{1}{r}\frac{\partial^2\varepsilon_{rr}}{\partial\beta\partial z} = -\frac{\partial^2}{\partial r\partial\beta}\left(\frac{\varepsilon_{rz}}{r}\right) - \frac{1}{r^2}\frac{\partial^2(r^2\varepsilon_{r\beta})}{\partial r\partial z} + \frac{\partial}{\partial r}\left(\frac{1}{r}\frac{\partial\varepsilon_{\beta z}}{\partial r}\right);$$
$$\frac{1}{r}\frac{\partial^2\varepsilon_{rr}}{\partial\beta^2} + \frac{1}{r}\frac{\partial}{\partial r}\left(r^2\frac{\partial\varepsilon_{\beta\beta}}{\partial r}\right) = \frac{2}{r}\frac{\partial^2(r\varepsilon_{\beta r})}{\partial\beta\partial r} + \frac{\partial\varepsilon_{rr}}{\partial r};$$
$$r\frac{\partial}{\partial z}\left(\varepsilon_{rr} - \frac{\partial(r\varepsilon_{\beta\beta})}{\partial r}\right) = \frac{\partial^2\varepsilon_{rz}}{\partial\beta^2} - \frac{\partial^2(r\varepsilon_{\beta z})}{\partial r\partial\beta} - \frac{\partial^2(r\varepsilon_{\beta r})}{\partial z\partial\beta}; \quad (4)$$
$$\frac{\partial^2\varepsilon_{\beta\beta}}{\partial z^2} + \frac{1}{r^2}\frac{\partial^2\varepsilon_{zz}}{\partial\beta^2} + \frac{1}{r}\frac{\partial\varepsilon_{zz}}{\partial r} = \frac{2}{r}\frac{\partial}{\partial z}\left(\frac{\partial\varepsilon_{\beta z}}{\partial\beta} + \varepsilon_{rz}\right);$$
$$\frac{\partial^2}{\partial r\partial\beta}\left(\frac{\varepsilon_{zz}}{r}\right) = -\frac{\partial^2\varepsilon_{\beta r}}{\partial z^2} + r\frac{\partial^2}{\partial r\partial z}\left(\frac{\varepsilon_{\beta z}}{r}\right) + \frac{1}{r}\frac{\partial^2\varepsilon_{rz}}{\partial z\partial\beta}.$$

Components of the full strain tensor ε_{ij} as part of the elastic formulation of the problem are related to the stress tensor σ_{ij} by the Hooke's law [8]:

$$\begin{gathered}\varepsilon_{rr}=\frac{1}{E}\left(\sigma_{rr}-\nu\left(\sigma_{\beta\beta}+\sigma_{zz}\right)\right)+\Pi_{rr};\\ \varepsilon_{\beta\beta}=\frac{1}{E}\left(\sigma_{\beta\beta}-\nu\left(\sigma_{rr}+\sigma_{zz}\right)\right)+\Pi_{\beta\beta};\\ \varepsilon_{zz}=\frac{1}{E}\left(\sigma_{zz}-\nu\left(\sigma_{rr}+\sigma_{\beta\beta}\right)\right)+\Pi_{zz};\\ \varepsilon_{r\beta}=\frac{2(1+\nu)}{E}\sigma_{r\beta}+\Pi_{r\beta};\ \ \varepsilon_{rz}=\frac{2(1+\nu)}{E}\sigma_{rz}+\Pi_{rz};\\ \varepsilon_{\beta z}=\frac{2(1+\nu)}{E}\sigma_{\beta z}+\Pi_{\beta z}.\end{gathered}\tag{5}$$

Components of the stress tensor are related to each other by the equilibrium equations [10]:

$$\begin{gathered}\frac{1}{r}\frac{\partial}{\partial r}(r\sigma_{rr})+\frac{1}{r}\frac{\partial\sigma_{r\beta}}{\partial\beta}+\frac{\partial\sigma_{rz}}{\partial z}+\rho F_r=0;\\ \frac{1}{r^2}\frac{\partial}{\partial r}(r^2\sigma_{r\beta})+\frac{1}{r}\frac{\partial\sigma_{\beta\beta}}{\partial\beta}+\frac{\partial\sigma_{\beta z}}{\partial z}+\rho F_\beta=0;\\ \frac{1}{r}\frac{\partial}{\partial r}(r\sigma_{rz})+\frac{1}{r}\frac{\partial\sigma_{\beta z}}{\partial\beta}+\frac{\partial\sigma_{zz}}{\partial z}+\rho F_z=0,\end{gathered}\tag{6}$$

where ρ is the material density; F_r, F_β, F_z are the components of mass force, in the considered problem of determining welding stresses and strains in the cylindrical shell $F_r = F_\beta = F_z = 0$.

The linear problem of elasticity theory can be solved by displacements. From the generalized Hooke's law equations (5), stresses through strains look as follows [8]:

$$\begin{gathered}\sigma_{rr}=A_1\varepsilon_{rr}+A_2(\varepsilon_{\beta\beta}+\varepsilon_{zz})+Y_{rr};\\ \sigma_{\beta\beta}=A_1\varepsilon_{\beta\beta}+A_2(\varepsilon_{rr}+\varepsilon_{zz})+Y_{\beta\beta};\\ \sigma_{zz}=A_1\varepsilon_{zz}+A_2(\varepsilon_{rr}+\varepsilon_{\beta\beta})+Y_{z};\\ \sigma_{r\beta}=A_3\varepsilon_{r\beta}+Y_{r\beta};\quad \sigma_{rz}=A_3\varepsilon_{rz}+Y_{rz};\\ \sigma_{\beta z}=A_3\varepsilon_{\beta z}+Y_{\beta z};\\ A_1=\frac{2K+\psi}{3\psi K};\quad A_2=\frac{\psi-K}{3\psi K};\quad A_3=\frac{1}{\psi};\\ K=\frac{1-2\nu}{E};\quad G=\frac{E}{(1+\nu)},\end{gathered}\tag{7}$$

where E is the normal elasticity modulus (Young's modulus); K is the bulk pressure modulus; G is the shear modulus; ψ is the material state function, that takes into account the plastic flow for the elastic behaviour of the material $\psi = 0.5G$; additions $Y_{i,j}$ take into account the load of the cylindrical shell by additional strains from welding shrinkage (in general appearance):

$$\begin{gathered}Y_{rr}=A_1\Pi_{rr}+A_2(\Pi_{zz}+\Pi_{\beta\beta});\\ Y_{\beta\beta}=A_1\Pi_{\beta\beta}+A_2(\Pi_{rr}+\Pi_{zz});\\ Y_{zz}=A_1\Pi_{zz}+A_2(\Pi_{rr}+\Pi_{\beta\beta});\\ Y_{r\beta}=A_3\Pi_{r\beta};\quad Y_{z\beta}=A_3\Pi_{z\beta};\quad Y_{rz}=A_3\Pi_{rz}.\end{gathered}\tag{8}$$

To model welding strains in a cylindrical shell from circumferential and longitudinal welded joints, the following basic parameters of the inherent strain function can be specified: plastic shrinkage strains in the axial Π_{zz} and circumferential $\Pi_{\beta\beta}$ directions. Plastic shrinkage strains in the radial direction Π_{rr} (across the thickness of the shell wall) cause local strains and do not significantly affect the overall distortions of the welded cylindrical shell. The tangent components of plastic shrinkage strains Π_{rz}, $\Pi_{r\beta}$, $\Pi_{z\beta}$ can be neglected, since the directions of welds in the cylindrical shell coincide with the longitudinal and circumferential direction of the cylindrical coordinate system.

$$\begin{gathered}Y_{rr}=A_2(\Pi_{zz}+\Pi_{\beta\beta});\\ Y_{\beta\beta}=A_1\Pi_{\beta\beta}+A_2\Pi_{zz};\\ Y_{zz}=A_1\Pi_{zz}+A_2\Pi_{\beta\beta};\\ Y_{r\beta}=0;\quad Y_{z\beta}=0;\quad Y_{rz}=0.\end{gathered}\tag{9}$$

With the use of the Cauchy distributions (3) binding the components of the full strain tensor ε_{ij} with the components of the displacement vector U_i, the stresses (7) can be presented through the displacements:

$$\begin{gathered}\sigma_{rr}=A_1\frac{\partial U_r}{\partial r}+A_2\left(\frac{\partial U_z}{\partial z}+\frac{\partial U_\beta}{r\partial\beta}+\frac{U_r}{r}\right)+Y_{rr};\\ \sigma_{\beta\beta}=A_1\left(\frac{\partial U_\beta}{r\cdot\partial\beta}+\frac{U_r}{r}\right)+A_2\left(\frac{\partial U_r}{\partial r}+\frac{\partial U_z}{\partial z}\right)+Y_{\beta\beta};\\ \sigma_{zz}=A_1\frac{\partial U_z}{\partial z}+A_2\left(\frac{\partial U_r}{\partial r}+\frac{\partial U_\beta}{r\cdot\partial\beta}+\frac{U_r}{r}\right)+Y_{z};\\ \sigma_{r\beta}=A_3\frac{1}{2}\left(\frac{\partial U_r}{r\partial\beta}+\frac{\partial U_\beta}{\partial r}-\frac{U_\beta}{r}\right);\\ \sigma_{rz}=A_3\frac{1}{2}\left(\frac{\partial U_r}{\partial z}+\frac{\partial U_z}{\partial r}\right);\ \sigma_{\beta z}=A_3\frac{1}{2}\left(\frac{\partial U_\beta}{\partial z}+\frac{\partial U_z}{r\partial\beta}\right);\end{gathered}\tag{10}$$

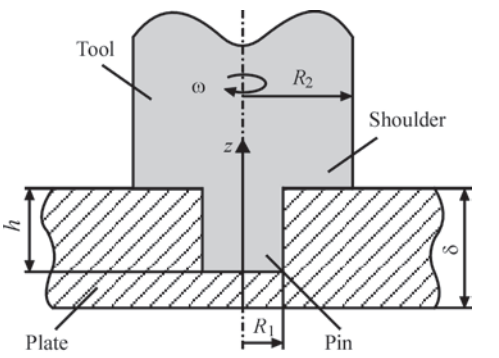

Figure 3. Scheme of working tool and joint plates at FSW

Let us substitute the obtained expressions for the components of the stress tensor into the equilibrium equation (6):

$$\begin{aligned}
&\frac{1}{r}\frac{\partial}{\partial r}\left(rA_1\frac{\partial U_r}{\partial r}+rA_2\left(\frac{\partial U_z}{\partial z}+\frac{\partial U_\beta}{r\partial\beta}+\frac{U_r}{r}\right)\right)+\\
&+\frac{1}{r}\frac{\partial}{\partial\beta}\left(A_3\frac{1}{2}\left(\frac{\partial U_r}{r\partial\beta}+\frac{\partial U_\beta}{\partial r}-\frac{U_\beta}{r}\right)\right)+\\
&+\frac{\partial}{\partial z}\left(A_3\frac{1}{2}\left(\frac{\partial U_r}{\partial z}+\frac{\partial U_z}{\partial r}\right)\right)=-\frac{1}{r}\frac{\partial}{\partial r}(rY_{rr});\\
&\frac{1}{r^2}\frac{\partial}{\partial r}\left(r^2A_3\frac{1}{2}\left(\frac{\partial U_r}{r\partial\beta}+\frac{\partial U_\beta}{\partial r}-\frac{U_\beta}{r}\right)\right)+\\
&+\frac{1}{r}\frac{\partial}{\partial\beta}\left(A_1\left(\frac{\partial U_\beta}{r\partial\beta}+\frac{U_r}{r}\right)+A_2\left(\frac{\partial U_r}{\partial r}+\frac{\partial U_z}{\partial z}\right)\right)+\\
&+\frac{\partial}{\partial z}\left(A_3\frac{1}{2}\left(\frac{\partial U_\beta}{\partial z}+\frac{\partial U_z}{r\partial\beta}\right)\right)=-\frac{1}{r}\frac{\partial Y_{\beta\beta}}{\partial\beta};\\
&\frac{1}{r}\frac{\partial}{\partial r}\left(rA_3\frac{1}{2}\left(\frac{\partial U_r}{\partial z}+\frac{\partial U_z}{\partial r}\right)\right)\sigma_{rz}+\\
&+\frac{1}{r}\frac{\partial}{\partial\beta}\left(A_3\frac{1}{2}\left(\frac{\partial U_\beta}{\partial z}+\frac{\partial U_z}{r\partial\beta}\right)\right)+\frac{\partial}{\partial z}\times\\
&\times\left(A_1\frac{\partial U_z}{\partial z}+A_2\left(\frac{\partial U_r}{\partial r}+\frac{\partial U_\beta}{r\partial\beta}+\frac{U_r}{r}\right)\right)=-\frac{\partial Y_{zz}}{\partial z}.
\end{aligned}\tag{11}$$

The obtained system of equations relative to the three components of the displacement vector U_x, U_β, U_z of an arbitrary point (x, β, z) of the cylindrical shell during loading by additional strains from the welding shrinkage (components Y_{rr}, $Y_{\beta\beta}$, Y_{zz} in the right part of the equations) and boundary conditions on the shell surface determine the general formulation of the boundary problem.

DETERMINATION OF INHERENT STRAIN FUNCTION FOR WELDED JOINTS

To determine the inherent strain function, the methods of mathematical modelling of temperature distributions and stress-strain state of a butt joint of plates at welding heating were used.

The peculiarity of the developed model of the heating source at FSW is the heat dissipation due to the friction of the tool relative to the joint material [6]. The tool (Figure 3) rotates around a vertical axis at a certain angular speed ω, rev/s and is pressed to the plate with an axial distributed force P_n, Pa, which causes the heat flux into the joint material on the contact surface of the tool:

$$\begin{aligned}
&\lambda\frac{\partial T}{\partial n}=\mu P_n\omega r,\ \mathrm{W/m^2};\\
&Q=\mu P_n\omega\iint\limits_s rdS,
\end{aligned}\tag{12}$$

where μ is the friction coefficient, whose value can be accepted as permanent at a level of 0.3–0.4 or variable depending on the temperature [11]; Q is the power of heat dissipation, W; S is the area of the corresponding contact surfaces, $Q_1=2\pi/3\,\mu P_n\omega(R_2^3-R_1^3)$ on the shoulder (z = δ, $R_1 < r < R_2$), $Q_2=2\pi\mu P_n\omega R_1^2 h$ on the side surface of the pin ($r = R_1$, δ – $h > z >$ δ), $Q_3=2\pi/3\,\mu P_n\omega R_1^3$ on the lower end surface of the pin (z = δ – h, 0 > $r > R_1$); δ is the thickness of welded plates, m; h is the length of the pin, m. The power of bulk heat dissipation $W(x, y, z, t)$, W/m^3 consists of heat dissipation in the volume V_1 on the upper surface of the joint plates under the tool shoulder and in the volume of the pin V_2 (dz is the size of the finite element):

$$\begin{aligned}
W(x,y,z,t)&=W_1+W_2=\frac{Q_1}{V_1}+\frac{Q_2+Q_3}{V_2}=\\
&=\frac{2\mu P_n\omega(R_2^2+R_2R_1+R_1^2)}{3(R_2+R_1)dz}+\frac{2\mu P_n\omega}{h}\left(h+\frac{R_1}{3}\right).
\end{aligned}\tag{13}$$

The model of thermoplastic deformation of the welded joint material provides that overall distortion tensor is the sum of elastic and plastic strains [8]:

$$\begin{aligned}
&\varepsilon_{ij}=\varepsilon_{ij}^e+\varepsilon_{ij}^p,\\
&\varepsilon_{ij}=\frac{\sigma_{ij}-\delta_{ij}\sigma}{}+\delta_{ij}(K\sigma+\varphi)\ \ (i,j=x,y,z),
\end{aligned}\tag{14}$$

where δ_{ij} is the Cronecker symbol; σ is the ball tensor; φ = α(T – T_0), where α is the ratio of relative temperature elongation of the material. Plastic strains are associated with the stresses by the equation of the theory of plastic non-isothermal flow (von Mises condition) [8].

RESULTS OF RESIDUAL STRESSES AND PLASTIC STRAINS CALCULATION

The calculated model for determination of residual stresses and strains at FSW of plates made of aluminium alloy (Al–6.5 % Cu) was validated by comparing the results of calculation by residual stresses with experimental measurement data. The calculated residual longitudinal stresses at FSW of a butt joint of an aluminium alloy with 10 mm thickness were determined as a result of the solution of the thermoplasticity problem for 3D model of a butt joint of plates of the limited size of 300×300 mm (Figure 2, *a*). Thermophysical and mechanical properties of aluminium alloy, depending on the temperature are shown in Figure 4 [9]. FSW parameters are R_2 = 10 mm, R_1 = 5 mm, ω = 700 rpm, P_n = 70 MPa, linear welding speed is 160 mm/min. The maximum calculated temperature at the set FSW parameters does not exceed 470 °C (Figure 5).

Experimental measurements of residual stress distribution were carried out on the samples of butt joints

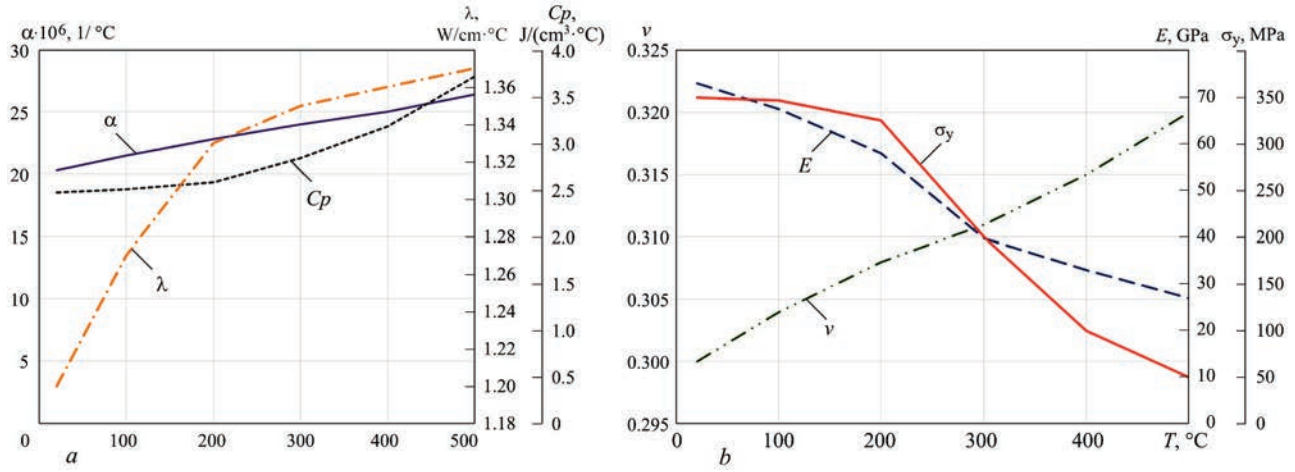

Figure 4. Thermophysical (*a*) and mechanical (*b*) properties of aluminium alloy (Al–6.5 % Cu)

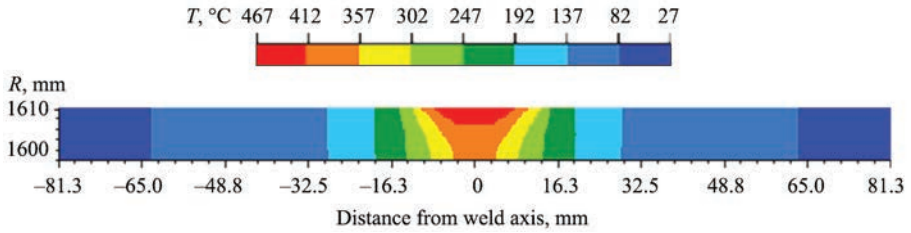

Figure 5. Maximum calculated temperature at FSW of a butt joint

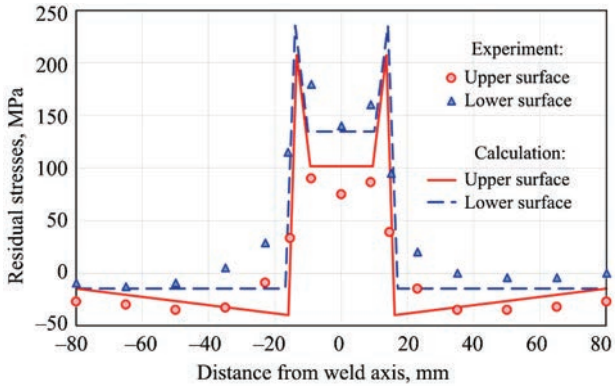

Figure 6. Distribution of residual longitudinal stresses

made by FSW by the method of full cutting into templates and measurement of elastic strains by means of mechanical strain gauge.

The nature of the distribution of calculated residual stresses is close to the experimental (Figure 6). The maximum level of calculated tensile stresses (up to 200 MPa) is slightly higher than experimental values up to 180 MPa). In the welded joint center, a zone of significant reduction in the tensile longitudinal stresses is located, which is associated with the effect of aluminium alloy softening. Also for experimental and calculated data, a significant difference between stresses on the upper and lower surfaces of welded

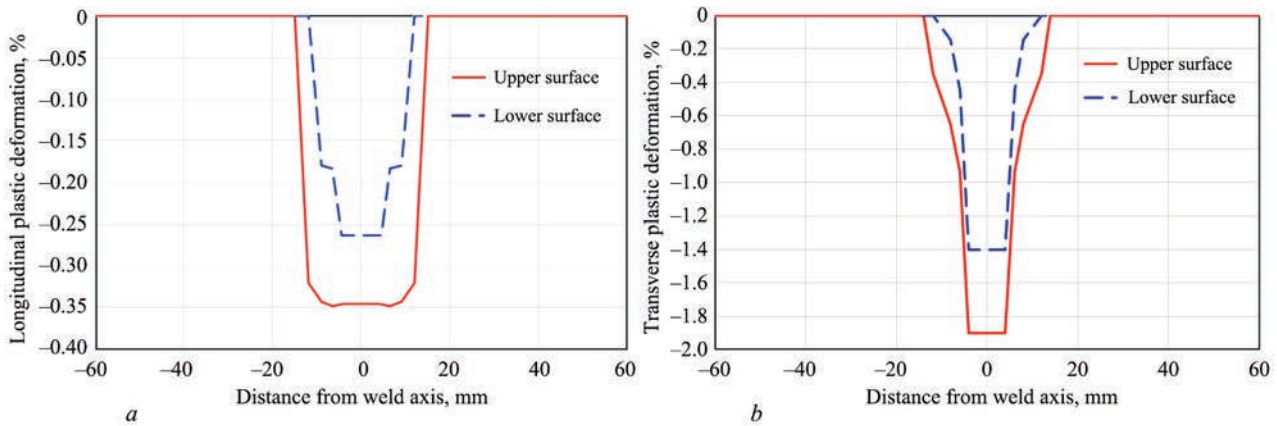

Figure 7. Results of calculating the distribution of longitudinal (*a*) and transverse (*b*) plastic strains for butt welded joints in the model of FSW of plates (300×300 mm, δ = 10 mm)

joint is typical — on the lower surface, residual tensile stresses are higher.

The estimate of the error of calculation data shows that in the zone of tensile stresses (3 central points, from –16 to +16 mm from the joint axis), the mean-square deviation from the experimental values on the lower surface of the sample is 21 %, and on the upper surface it is up to 31 %. Such an error can be accepted as satisfactory, considering the complex nature of residual stress distribution.

The results of residual distributions of longitudinal $\Pi_{xx} = \varepsilon^p_{xx}(y,z)$ and transverse $\Pi_{yy} = \varepsilon^p_{yy}(y,z)$ plastic strains at FSW were obtained (Figure 7). It should be noted that transverse and longitudinal plastic strains on the upper surface of the welded plate are approximately by 25 % higher in absolute value than those on the lower surface. This is predetermined by the nonuniform distribution of the maximum temperature over the welded joint thickness. It should also be noted that transverse plastic strains in terms of absolute value are approximately five times higher than longitudinal, but the zone of longitudinal plastic strain formation is 1.5–2 times wider.

RESULTS OF WELDING STRAIN MODELLING

The obtained distributions of residual longitudinal $\Pi_{xx} = \varepsilon^p_{xx}(y,z)$ and transverse $\Pi_{yy} = \varepsilon^p_{yy}(y,z)$ plastic strains were used in the prediction of the overall distortions of the long cylindrical shell by the inherent strain function method (2) (Figure 8, *a*, $2R$ = = 3200 mm, L = 6000 mm, δ = 10 mm), which contains six longitudinal and five circumferential welded joints (location coordinates of the circumferential welded joints z = 1, 2, 3, 4, 5 m, longitudinal welded

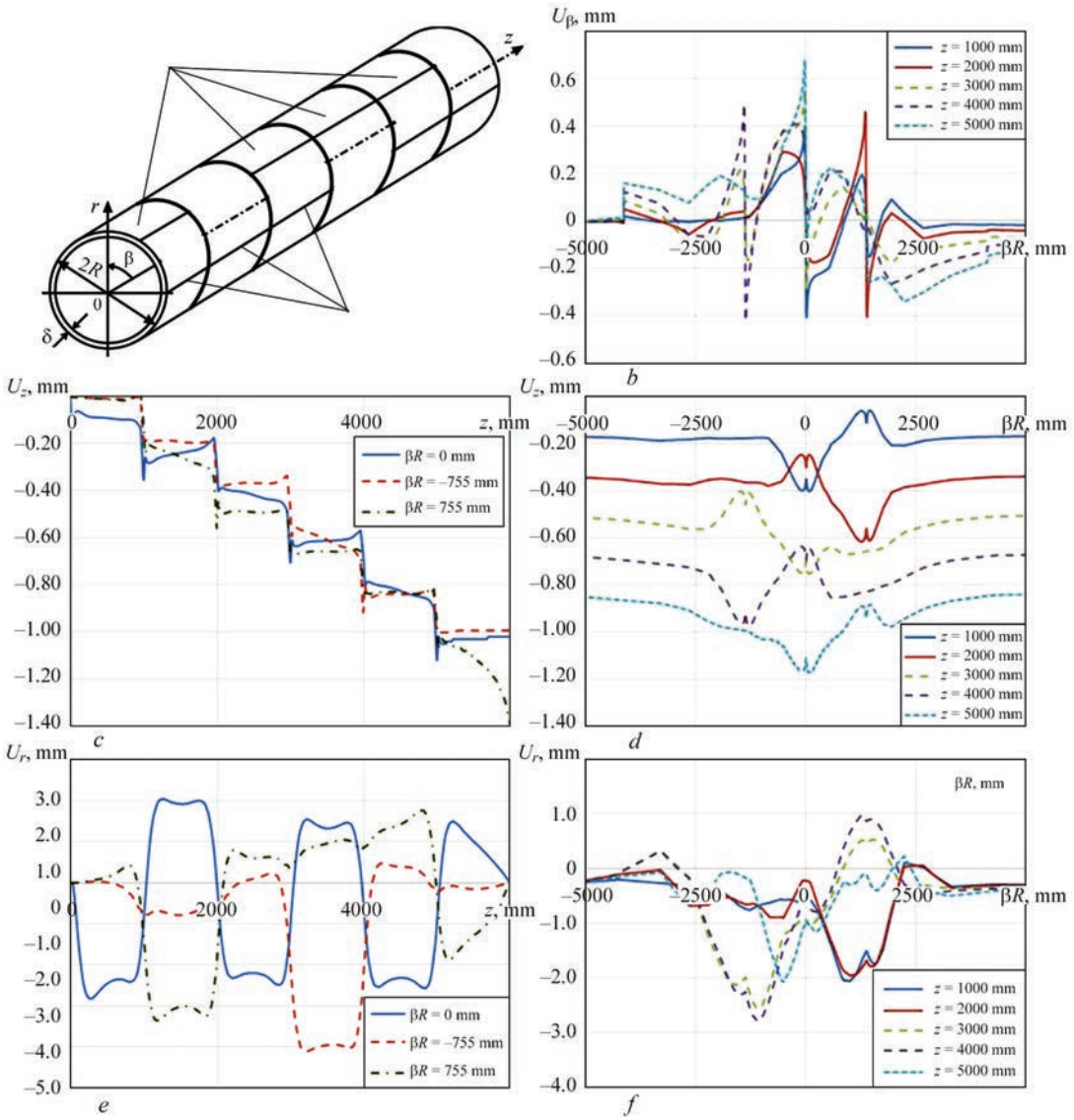

Figure 8. Welding distortions of the cylindrical shell: *a* — scheme of welds location; *b* — displacements U_β along the shell circle; *c* — displacement U_z along the shell axis; *d* — displacements U_z in different sections along the length of the shell; *e* — radial bending U_r along the shell axis; *f* — radial bending U_r along the circle in different sections along the length of the shell

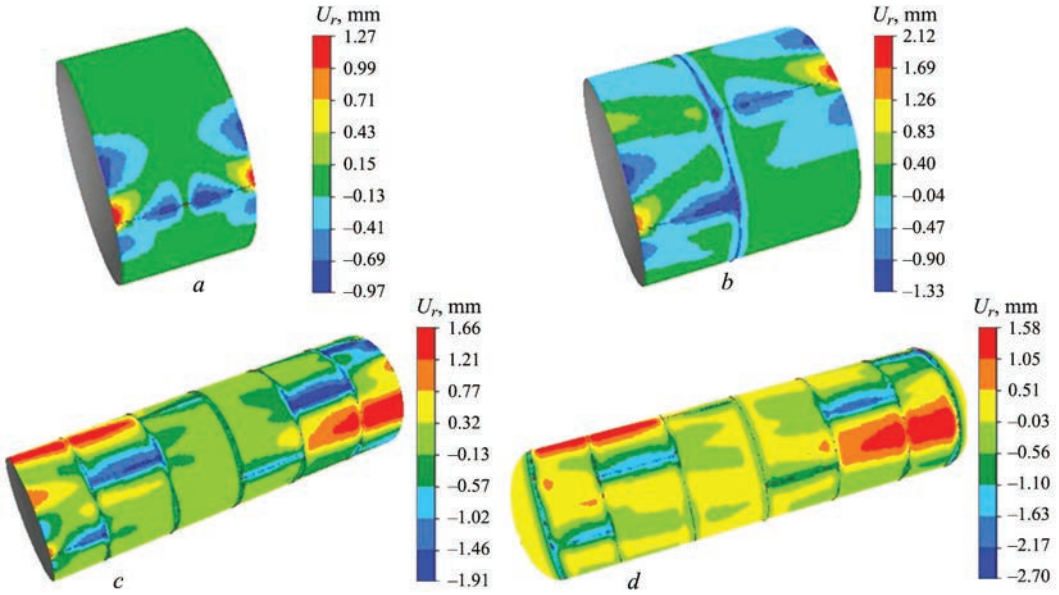

Figure 9. Radial displacements of the cylindrical vessel at different stages of assembly and assembly welding: *a* — longitudinal joint of the shell ring; *b* — circumferential joint of two rings; *c* — cylindrical shell with circumferential and longitudinal welds; *d* — cylindrical vessel with welded-on bottoms

butts β = 0, ±755 mm). The solution of the problem by displacements of the surface points of the cylindrical shell was obtained by the finite element method on a full-size model for each welded joint separately and then overall displacements were added by the principle of superposition.

The presence of a great number of circumferential joints leads to the accumulation of axial (longitudinal) displacements U_z along the shell (Figure 8, *c*, *e*). The rest of the strain components like circumferential displacements U_β (Figure 8, *b*) and radial bending U_r (Figure 8, *e*, *f*) have a complex local nature of distribution. This example demonstrates the efficiency of the developed calculation algorithm when predicting welding strains of large cylindrical shells with a great number of welded joints based on the approximated inherent strain function method.

The developed mathematical model and calculation algorithm based on the inherent strain function method can be effectively used in the technological preparation of manufacturing large cylindrical vessels of aluminium alloys for in-process prediction of stress-strain state. As an example, Figure 9 presents the results of predicting the distribution of radial displacements at different stages of assembly and assembly welding of a large cylindrical vessel. Radial displacements have a complex nature of distribution, deflections of up to ≈ –3 mm in the zones of circumferential and longitudinal welded joints are changed with the shell bends of up to ≈ 1.5 mm in the gaps between the welded joints. Given the large sizes of the considered welded vessel (3200 mm diameter), the maximum obtained displacement values are not high, due to the low level of residual strains at FSW.

CONCLUSIONS

1. A mathematical model and calculation algorithm have been developed based on the inherent strain function method for numerical determination of welding strains of large cylindrical shells with a great number of circumferential and longitudinal welded joints.

2. The inherent strain function parameters of welded joints are plastic strains in the axial Π_{zz} and circumferential $\Pi_{\beta\beta}$ directions that can be determined by numerical methods of thermoplasticity on simplified models of longitudinal and circumferential welded joints. These models also allow determining local distributions of maximum welding temperatures and residual stresses in the joint zone.

3. The reliability of the mathematical model of determining residual stresses and plastic strains at FSW of aluminium alloy is confirmed by the agreement of the calculated data relative to the distribution of residual longitudinal stresses with the data of experimental measurements.

4. The developed mathematical models and calculation algorithms can be effectively used for in-process prediction of a stress-strain state in assembly welding of large cylindrical vessels of aluminium alloys.

REFERENCES

1. Poklyatskyi, A.G., Motrunich, S.I., Fedorchuk, V.Ye. et al. (2023) Mechanical properties and structural features of butt joints produced at FSW of aluminium alloys of different alloying systems. *Avtomatych. Zvaryuvannya*, **5**, 18–26 [in Ukrainian]. DOI: https://doi.org/10.37434/as2023.05.02
2. Vasanthakumar Pandian, Sekar Kannan (2020) Numerical prediction and experimental investigation of aerospace-grade dissimilar aluminium alloy by friction stir welding. *J. of Manufacturing Processes*, **54**, 99–108. DOI: https://doi.org/10.1016/j.jmapro.2020.03.001

3. Makhnenko, O.V., Muzhichenko, A.F. (2007) Mathematical modelling of thermal straightening of cylindrical shells and shafts with distortions along their longitudinal axis. *The Paton Welding J.*, **9**, 17–22.
4. Masabuchi, K. (1987) *Analysis of welded structures residual stresses, distortions and their consequences*. Pergamon Press, New-York.
5. Dresbach, C., van Enkhuizen, M.J., Alfaro Mercado, U. et al. (2015) Simulation of thermal behavior during friction stir welding process for predicting residual stresses. *CAES Aeronautical J.*, **6**, 271–278. DOI: https://doi.org/10.1007/s13272-014-0145-9
6. Tsaryk, B.R., Muzhychenko, O.F., Makhnenko, O.V. (2022) Mathematical model of determination of residual stresses and strains in friction stir welding of aluminium alloy. *The Paton Welding J.*, **9**, 33–40. DOI: https://doi.org/10.37434/tpwg.2022.09.06
7. Makhnenko, O.V. (2010) Combined use of the method of thermoplasticity and the method of the shrinkage function for the study of the process of thermal straightening of shipbuilding panels. *J. of Mathematical Sci.*, 167(**2**), 232–241. DOI: https://doi.org/10.1007/s10958-010-9917-x
8. Makhnenko, V.I. (1976) *Calculation methods for studying the kinetics of welding stresses and deformations* [in Russian]. Kyiv, Naukova Dumka.
9. Abdulrahaman Shuaibu Ahmad, Yunxin Wu, Hai Gong, Lin Nie (2019) Finite element prediction of residual stress and deformation induced by double-pass TIG welding of Al 2219 plate. *Materials,* 12(**14**), 2251. DOI: https://doi.org/10.3390/ma12142251
10. Timoshenko, S.P. (1976) *Elasticity theory course* [in Russian]. Kyiv, Naukova Dumka.
11. Saad B. Aziz, Mohammad W. Dewan, Daniel J. Huggett et. al. (2016) Impact of friction stir welding (FSW) process parameters on thermal modeling and heat generation of aluminum alloy joints. *Acta Metallurgica Sinica*, **29**, 869–883. DOI: https://doi.org/10.1007/s40195-016-0466-2

ORCID
B.R. Tsaryk: 0000-0002-8929-7722,
O.V. Makhnenko: 0000-0002-8583-0163

CONFLICT OF INTEREST
The Authors declare no conflict of interest

CORRESPONDING AUTHOR
O.V. Makhnenko
E.O. Paton Electric Welding Institute of the NASU
11 Kazymyr Malevych Str., 03150, Kyiv, Ukraine.
E-mail: makhnenko@paton.kiev.ua

SUGGESTED CITATION
B.R. Tsaryk, O.V. Makhnenko (2024) Mathematical modelling of distortions at welding of large vessels of aluminium alloy. *The Paton Welding J.*, **8**, 18–25. DOI: https://doi.org/10.37434/tpwj2024.08.03

JOURNAL HOME PAGE
https://patonpublishinghouse.com/eng/journals/tpwj

Received: 01.07.2024
Received in revised form: 31.07.2024
Accepted: 30.08.2024

DOI: https://doi.org/10.37434/tpwj2024.08.04

COMPOSITE (CORED) GRAPHITIZED ELECTRODES FOR INDUSTRIAL DC AND AC STEEL-MELTING FURNACES

O.G. Bogachenko[1], D.D. Mishchenko[1], I.O. Goncharov[1], I.O. Neilo[1], M.M. Gasik[2], S.G. Kiiko[3], I.M. Logozinskyi[3], K.M. Gorban[3]

[1]E.O. Paton Electric Welding Institute of the NASU
11 Kazymyr Malevych Str., 03150, Kyiv, Ukraine
[2]Aalto University, Espoo, Finland
[3]PJSC "Dniprospetsstal"
81 Pivdenne Highway, 69000, Zaporizhzhya, Ukraine

ABSTRACT

The paper presents summary data based on the results of laboratory studies and comprehensive industrial trials of a fundamentally new type of product in electrometallurgy — cores of graphitized electrodes developed at PWI of the NAS of Ukraine for DC and AC arc steel-melting furnaces of up to 50 t capacity. It is shown that during the last decades, the world production of steel has increased continuously, getting very close to 2 bln t per year. Approximately 30 % of this volume is produced in arc furnaces, and by the end of this decade it will reach 40 %. It is shown that the cored electrode arc has much lower specific current and power values in all the sections (cathode, column, anode) than the monolithic electrode arc. It was found that voltage drop in the core cathode spot is 2.3–3.3 times smaller than in the monolithic electrode. Cored electrodes improve all the technical-economic characteristics of operation of DC and AC steel-melting furnaces.

KEYWORDS: arc furnaces, graphitized electrodes, geometrical and power parameters of the arc, electrode work function, specific power, specific electrical resistance

INTRODUCTION

Academician B.E. Paton in his program article "Duma of Metal" made a clear prediction that metal materials in general and, above all, materials based on iron (steels, alloys, cast irons) have been and will be the basic structural materials in the near future for our civilization for the various needs of modern engineering.

This forecast is clearly confirmed by the rapid development of production and consumption of steel in recent decades. It is sufficient to point out that steel production has increased from 700 mln t in 1974 to 1.950 bln t in 2021, that is, by 2.8 times, despite constantly growing requirements for environmental protection and cruel competition at the market of production and consumption of metal materials [1–4].

Modern metallurgy is actively developing also in terms of its quality. Much attention is now paid to the transition to "green" metallurgy, the development of production of metallic raw materials, etc. New processes combining steel smelting and casting, rolling and heat treatment of steel semi-finished products are emerging everywhere.

Smelting in the arc AC (EAF) and DC (EAF) furnaces occupies more than a third part in the world production of steel. These are first and foremost alloy steels and alloys with high standard and special properties for critical products. It is expected that the world's share of electric steel will grow to 40 % in the next decade. The production of electric steel in China will grow to 25 % compared to 10 % in 2020. Naturally, the production of electrodes will grow. In this case, the focus will be on the production of high-quality electrodes of the EGSP grade (UHP) with a diameter of 700 mm or more [5]. Ukraine is a well-known metallurgical state in the world and before the war of 2022 it had firmly occupied a position in the first ten world steel makers. The great contribution to the theory and development of electrical steel-making was made by such Ukrainian scientists and manufacturers as B.E. Paton, B.I. Medovar, M.M. Dobrokhotov, V.A. Efimov, V.I. Lakomsky, A.F. Tregubenko, V.V. Leporsky et al.

Large-scale works on the improvement of technology and equipment for smelting and redistribution of steel are carried out under conditions of rigid competition at the market of metal products. These works are aimed at improvement of such important technical and economic characteristics as consumption of electric power and graphitized electrodes, alloying elements and ferroalloys, output of furnaces, etc. under conditions of providing high quality of metal, satisfying rigid requirements for environmental protection and improving the working conditions of service personnel.

RESEARCH AND DISCUSSION OF RESULTS

It is known that technical and economic characteristics of arc furnace operation are largely determined by the operational reliability of graphitized electrodes. In the cost of electric steel, electrodes occupy a considerable share — up to 8–15 and sometimes

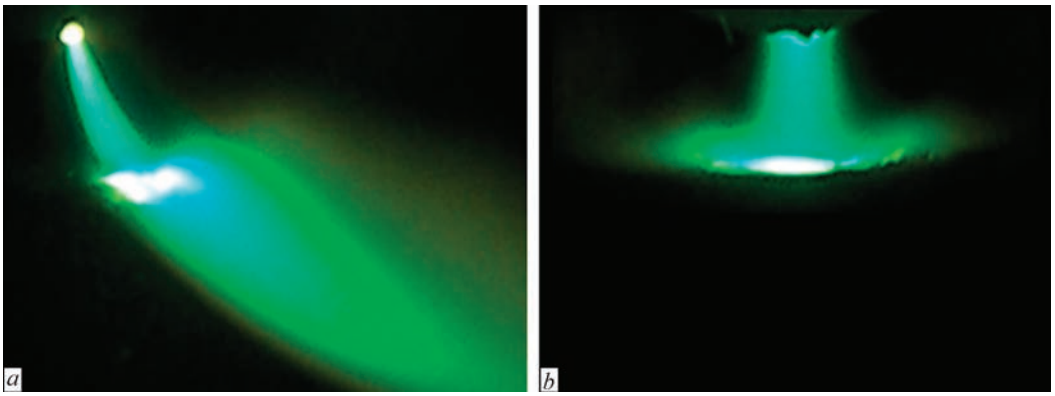

Figure 1. General appearance of the arc of graphitized monolithic (*a* — U_a = 62 V; I_a = 720 A; d_c = 2.5; d_a = 9.5 mm) and cored (*b* — U_a = 32 V; I_a = 720 A; d_c = 9.5 mm; d_a = 17 mm) electrodes at equal lengths of arcs (L_a = 15 mm)

up to 30 %. Therefore, it is difficult to overestimate the importance of the works conducted by electrode manufacturers to provide the required specific electrical resistance (SER), increase the density of electric current, ensure high mechanical characteristics of electrodes, etc. One of the modern world trends in improving the operation of arc furnaces is to increase the electric current to 80–100 kA. This requires a reduction in SER to 4–5 μOhm·m and an increase in the diameter and length of graphitized electrodes. Such famous Companies as SGL, Grafftech, Ukrgrafit, etc. have already mastered the production of electrodes with a diameter of 700, 750 and 800 mm. The length of the electrodes reached 3500 mm [5, 6]. The technical and economic assessment shows that a decrease in SER by 0.2 μOhm·m provides a reduction in power consumption by 6–8 % per a ton of metal.

At the PWI of NASU, a fundamentally new type of products for electrometallurgy — graphitized composite (cored) electrodes for arc steel-melting DC and AC furnaces was developed, which is studied and tested jointly with scientific centers and industrial enterprises.

PROCEDURE OF STUDIES

At the initial stage of works, the basic physical, chemical and power properties of the core and cored electrodes (Volt-ampere characteristics (VACh), current in the cathode-anode system, emission properties, power distribution over the arc sections, etc.) were investigated in the conditions of the PWI. For this purpose, specialized laboratory equipment was created, which used graphitized electrodes with a diameter of 50 mm. Industrial trials of cored electrodes were performed in 12-ton EAF DC-12 and three-phase DS-6N-1 and DSV-50 AC furnaces.

Cored electrodes are produced by drilling of one or more longitudinal holes in the serial monolithic electrode, which is stuffed with a mixture containing materials (components) to ensure the thermal stability of the core, regulation of its electrical conductivity and components with elements of the I and II groups of the Mendeleev table with low electron work function*. Due to these components with minimal power consumption, favorable thermodynamic conditions for the ionization of gases in the column of high-current electric arc in EAF and EAF DC are provided. The first comparative trials of cored and monolithic electrodes in laboratory equipment and in industrial furnaces showed that the cored electrode arc is fundamentally different by geometric and power parameters and very high stability compared to the monolithic electrode arc (Figure 1).

It was established that the diameter of the cathode spot on the cored electrode is approximately 4 times exceeds the analogue on the monolithic one. Diameters of anodes on the cored and monolithic electrodes differ in 2–3 times. The cored electrode arc is always maintained on the core and occupies almost the entire cross-sectional area of the electrode as a result of mutual diffusion of components in the core-electrode system. It does not migrate along the end of the electrode and does not come to its side surface, providing stable, soft heating of the melt and vertical position [7, 8]. At the same time, as a result of migration of the monolithic electrode arc, the plume of its plasma can amount to 7–8 lengths of the arc and reach the furnace lining, causing overheating and destruction of the lining. These and other features of the cored electrode arc are realized in improvement of almost all technical and economic indices of arc furnace operation.

The mentioned differences in geometric and electrical indices cause that all the cored electrode arc sections have significantly lower specific values of current density and power than the corresponding monolithic electrode arc sections. The calculations were performed according to the data of melts in a 12-ton DC furnace at equal voltages of arcs (220 V) and equal currents (11000 A) for monolithic and cored electrodes. Fifteen values were compared. It is enough to note that the spe-

*In the article, compositions of cores are not given. The cores are indicated by the letter C with indices 1, 2, 3 etc.

cific current, attributed to a unit of surface or a volume of the arc and specific power at the cored electrode cathode is 16.0 and 37.5 times lower, respectively, than at the monolithic electrode cathode [9].

RESEARCH RESULTS

SOME PROPERTIES AND FEATURES OF THE CORED ELECTRODE ARC

Studies of comparative voltage distribution over arc sections were performed in the laboratory equipment with the use of laboratory monolithic and cored electrodes with a diameter of 50 mm and a core of the composition C_4. The voltage drop on the arc sections and current under the conditions of the same voltage on the arcs (50 V), given in Table. 1, from which is follows that: the arc length L_a of the cored electrode was 23 mm, L_a of the monolithic electrode was 15 mm, i.e. more by 1.53 times; voltages on the anode spots of the arc U_{an} for these electrodes are close in values and equal to 15 and 13 V, respectively (average data by three dimensions); the emitter current I_{em} was 100 A, that is, the total current increased from 350 to 450 A, which was 28.5 %; the voltage drop on the arc column U_{col} of the core is 1.74 times higher than on the arc column of the monolithic electrode; the voltage gradients in the arc of cored and monolithic electrodes are close (1.0 and 1.1 V/mm); it is of particular interest that the cathode voltage U_c of the monolithic electrode (22.5 V) is 2.32 times higher than U_c of the cored electrode (9.7 V).

The voltage drops in the sections of the arcs at their equal lengths (15 mm) for compositions of the cores C_1–C_5 are presented in Table 2, from which it follows: the voltages U_{an} of the cored and monolithic electrodes are almost equal (10–13 V); the voltages on the arcs U_a of the monolithic and cored electrodes were 55 and 37.2 V (average values of 5 experiments), that is, the ratio is equal to 1.48 times. This index is close to the difference in arc lengths in case of equal voltages (1.53) (Table 1).

It is confirmed that equal currents can be ensured at the voltages of approximately 1.5 times lower in the case of the cored electrode compared to the monolithic one; the voltage drop on the arc column U_{col} of the monolithic and cored electrodes have close values — 25.5 and 20.8 V (average values from 5 experiments); as in the case of experiments with equal voltages (Table 2), the drop of voltages on the cathode spot of monolithic and cored electrodes: 18.0 and 5.5 V (average for 5 compositions), 18.0:5.5 = 3.3 times.

It is also important that the noted parameters have fairly clear stability at very large differences in the compositions of cores.

There were also experiments conducted to determine: the critical length of the arc at which its break occurs (L_{br}); the values of emitter currents (I_{em}); geometric parameters of the arc.

The obtained characteristics of the monolithic and cored electrodes are given in Table 3.

The VACh was investigated on the monolithic and cored electrodes of five core compositions (C_1–C_5). The results are presented in Figure 2.

As is seen from Figure 2, the current of the order of 400 A on the cored electrodes is provided at a voltage of 5–2.5 times lower than on the monolithic electrode, or at equal voltages on the arcs, the current on the cored electrodes is 1.5–2.0 times higher than the current of the monolithic electrode.

Table 1. Arc values in the sections of monolithic and cored electrodes at equal voltages of the arcs

Arc parameters	Electrode		Ratio of values
	Monolithic	Cored	
U_a, V	50.0	50.0	–
U_c, V	22.5	9.7	$\frac{U_{\text{c. cored}}}{U_{\text{c. monol.}}} = \frac{22.5}{9.7} = 2.32$
U_{an}, V	13.0	15.0	–
U_{col}, V	50–(22.5 + 13) = 14.5	50–(9.7 + 15) = 25.3	$\frac{U_{\text{col. cored}}}{U_{\text{col. monol.}}} = \frac{25.3}{14.5} = 1.74$
I, A	350	450	–
L_a, mm	15	23	$\frac{U_{\text{arc cored}}}{U_{\text{arc monol.}}} = \frac{23}{15} = 1.53$
b, V/mm	$\frac{14.5\text{ V}}{15\text{ mm}} \approx 1$ V/mm	$\frac{25.3\text{ V}}{23\text{ mm}} \approx 1.1$	–

Table 2. Values of voltage drop in the sections of the arcs at equal lengths of arcs and core compositions C_1–C_5

Arc parameters	Monolithic electrode	C_1	C_2	C_3	C_4	C_5
U_a, V	52–55 54.0	35–48 39.0	36–53 42.0	36–39 37.5	38–47 41.0	38–39 39.5
U_c, V	18–18 18.0	5–6 5.5	5–8 7.0	5–7 6.0	6–9 7.5	5–9 7.0
U_{col}, V	20–25.5 23.0	17–27 20.0	21–30 22.0	20–23 21.0	20–24 21.0	19–23 20.5
U_{an}, V	11.5–14 13.0	13–15 13.5	10–15 13.0	10–11 10.5	12–14 13.0	10–12 11.0
Current, A	300–307 304	300–360 354	300–350 350	313.5–420 367	320–387 350	310–320 313
b, V/mm	1.53	1.33	1.46	1.4	1.37	1.37

Table 3. Characteristics of monolithic and cored electrodes

Number	Mode parameters	Electrode		Note
		Monolithic	Cored	
1	U_a, V	64	64	–
2	I_a, A	400	500	I_{em} = 500 – 400 = 100 A; Δ = 25 %
3	P_a, W	25600	32000	32000:25600 = 1.25 due to I_{em}
4	L_a initial, mm	10	10	–
5	L_a break, mm	21	33	$\frac{33}{21}$=1.52
6	Cathode diameter, mm	~5	~16	–
7	Arc column diameter, mm	~8	~20	–
8	Anode diameter, mm	~15	~35	–

It is known that one of the most important characteristics of graphitized electrodes for arc steelmaking furnaces is SER. This index is of some importance for each of the four grades of electrodes (EG, EGP, EGS, EGSP) used in all arc furnaces. Here, the higher the quality of the electrode (from EG to EGSP), the lower SER they have and, consequently, the higher the admissible current loads. For example, for electrodes with a diameter of 508 mm of EG grade used in 50-t furnaces, this index is 15–18 A/cm^2, and for EGSP grade it is 22–28 A/cm^2.

The core and the electrode create a single core-electrode system and are not isolated from each other. Therefore, SER of the cored electrode will be different from SER of the monolithic electrode-analogue.

The peculiarity of the production and operation of cored electrodes is that after stuffing of the cored mass into the electrode, it is not subjected to any heat treatment and is mounted on the furnace in the raw form. Therefore, all processes like removal of binding elements, physicochemical processes, formation of structure and properties of the core and electrode occur when the electrode is heated from a temperature of 20–30 °C (mounting in a set) on the furnace to the order of 4000 °C at the working end of the electrode in the near-arc part. At the same time, all the mentioned processes take place in the closed space of the furnace under conditions of lack of oxygen and excess of carbon.

In the mentioned conditions, there are no doubts regarding two factors: the first, in the core-electrode system there active processes of mutual diffusion of components occur; the second, given the constantly

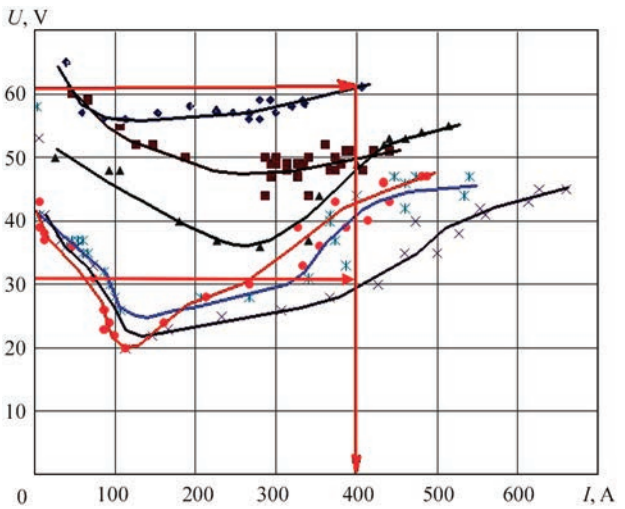

Figure 2. VACh of arcs of monolithic and cored electrodes: ✱ — monolithic electrode; ♦ — C_1; ■ — C_2; A — C_3; ● — C_4; ● — C_6

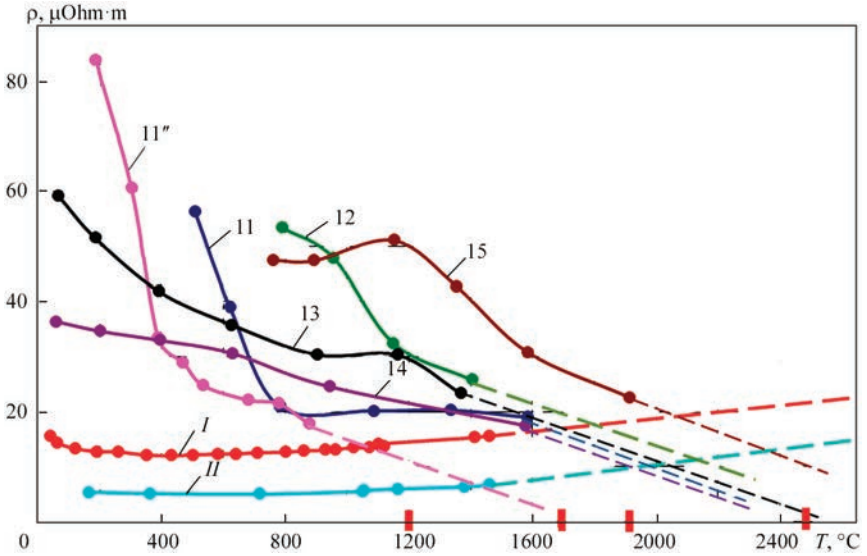

Figure 3. Dependence of specific electrical resistance of cores on temperature: 11–15 — core compositions, conditionally; *I* and *II* are monolithic electrodes

increasing temperature along the length of the electrode, all the above physicochemical processes in the core-electrode system are in a quasi-stationary state. Therefore, any analysis of the mentioned processes should be carried out in certain temperature zones along the length of the electrode.

The carried out studies and experiments indicate that SER of the cored graphitized electrode (core-electrode system) depends on many technological and power factors and processes being in a quasi-stationary state in an operating furnace. SER of the cored electrode is also in the same state, that is, it changes in time depending both on length as well as cross-section. As an example, Figures 3 and 4 show the results of studying the temperature dependence of SER on the composition of cores. In Figure 3, the results of trials of 5 core compositions (C_{11}–C_{15}) are given. As a criterion for evaluation of each composition, the temperature is accepted, at which curves of SER of cores intersect with SER of two initial monolithic electrodes (curves *I* and *II*). It is seen that SER of the core is equal to SER of the electrode and may further decrease in the temperature range of 1600–2500 °C, depending on the composition of the core and SER of initial monolithic electrodes. Even more clearly, the temperature dependence of SER of the core revealed itself when non-stoichiometric titanium nitride ($TiN_{0.8}$) was introduced into its composition. In this case, equalization of SER of the cores and electrodes has a clearly pronounced nature and occurs in the same temperature range (1400–2000 °C) relative to the initial monolithic electrode (*I*). With regard to the monolithic electrode with a low SER (*II*), the temperature interval of the SER lines intersection shifts to the right to approximately 1800–2500 °C.

Thus, the equality area of SER of the cores and electrodes is in the temperature range of 1200–2500 °C and is determined by the composition of the core and

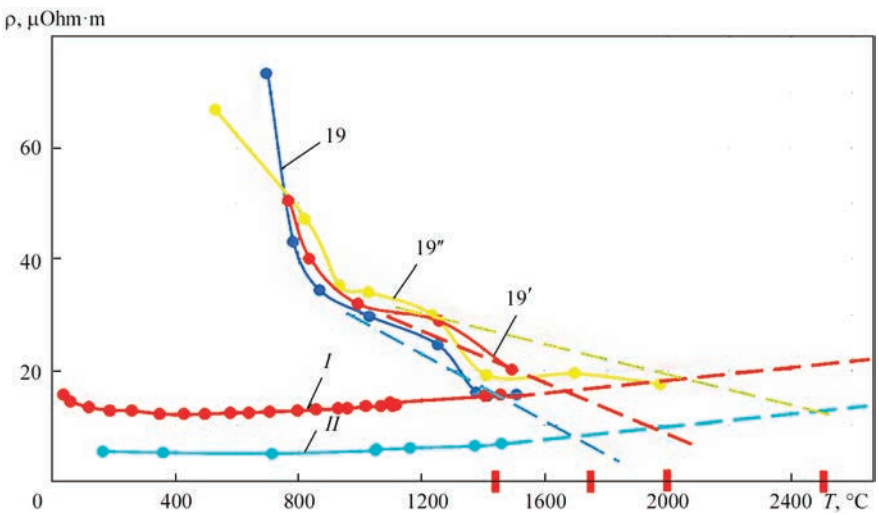

Figure 4. Dependence of specific electrical resistance on temperature of raw cores based on TiN (explanations are given in the text and in Table 2)

SER of the electrode. In turn, these indices are determined by the degree of completeness of diffusion processes in the core-electrode system and the actual state of creation (decomposition) of chemical compounds with semiconductor properties, that ultimately reduce SER of the core-electrode system.

The first studies of diffusion and determination of SER in the core-electrode system were conducted on full-scale samples from an industrial electrode with an initial diameter of 350 mm from the furnace EAF DC-12, which was heated from a temperature of 20–30 °C to the order of 3900–4000 °C (in the near-arc part) and exposure for 95 thou h.

In these melts, cores of the composition C_0^* were used. After 1.0–1.5 h from switching on the furnace, at the end of the electrode, a concave hemisphere was formed, predetermined by the presence of core in the center of the electrode. The shape of the hemisphere is determined by the electrical mode, the electrical resistance of the electrode body and core, the composition of metal and slag and other factors. The overall appearance of the working end of the electrode with the core, which was heated to 3900–4000 °C and natural cooling to room temperature, is presented in Figure 5. From the end of the electrode with the core, four samples were selected according to the scheme presented in Figure 6. The temperature dependence of SER of these samples was determined by specialized equipment. The test results are presented in Figure 7, from which it is seen that: SER of horizontal samples (1H and 2H) and extreme vertical (1V) are almost the same, which indices a high degree of isotropicity according to this indicator in the cored graphitized electrode; the vertical sample 2V has a significantly lower specific electrical resistance (in average by 12 %) and almost constant than the rest. This is explained by the fact that the elements with low electron work function, which transferred from the diffusion from the core into the electrode body, maintained in the central zone of the electrode in greater quantity than in the extreme sample 1V. Depletion of the sample 1V with the mentioned elements also occurred as a result of diffusion when the template was cooled to room temperature.

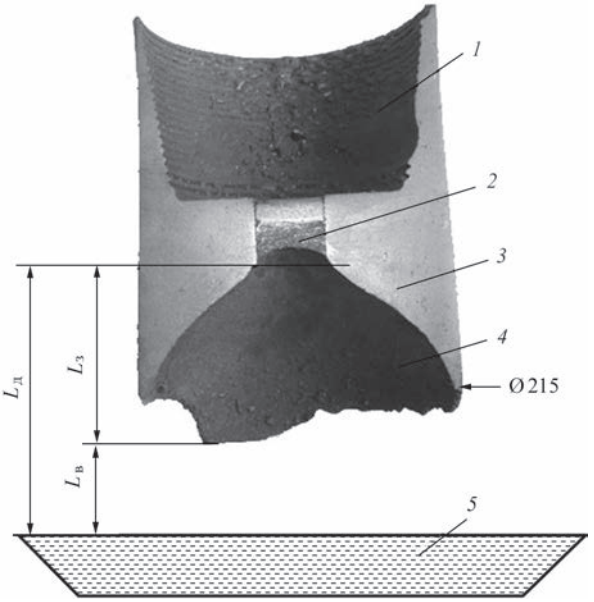

Figure 5. Macrostructure of working end of the graphitized electrode with an initial diameter of 350 mm (from EAF DC-12 furnace): *1* — nipple nest; *2* — core; *3* — electrode; *4* — hemisphere; *5* — liquid slag

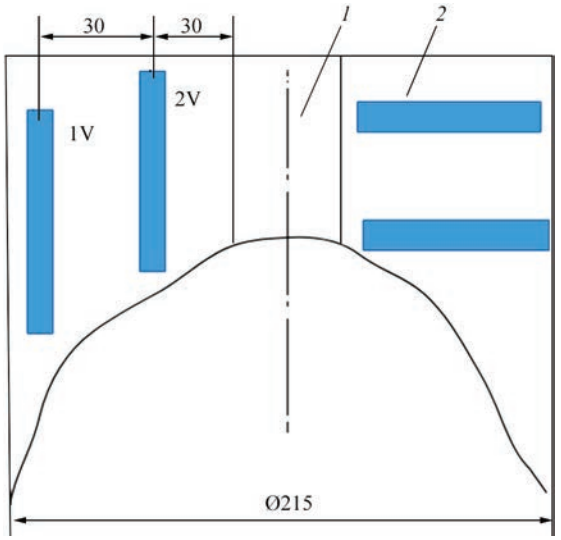

Figure 6. Scheme of cutting out samples: *1* — core; *2* — electrode

RESULTS OF USING CORED ELECTRODES IN INDUSTRIAL DC FURNACES

The above calculated, experimental and practical data convincingly testify the clear power and technological benefits of the cored arc.

The first industrial studies of cored electrodes were conducted in a 12-t EAF DC-12 furnace. 70FeSiMn wastes were used as a charge, i.e., a relatively simple and homogeneous charge. The tasks of these tests included: determination of technical and economic in-

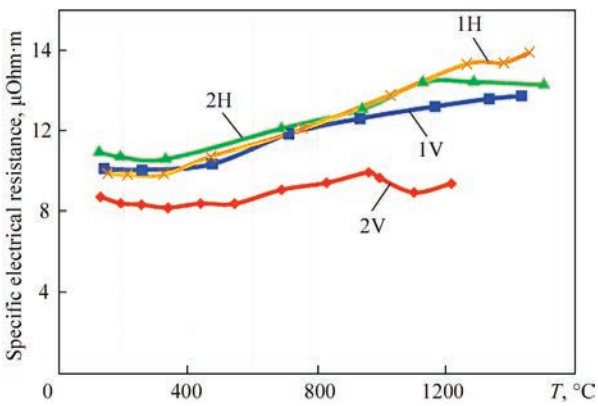

Figure 7. Temperature dependence of specific electrical resistance of samples of electrode material

*The composition of core and component distribution in electrode body is not given in the article.

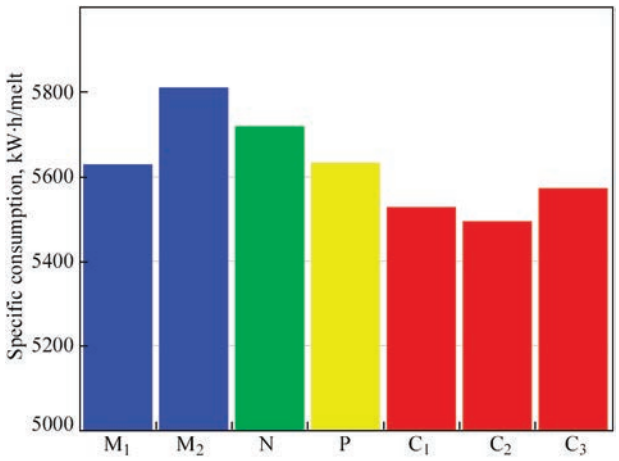

Figure 8. Specific consumption of active electric power during the melts on the serial mode using monolithic (M) electrodes, hollow (H) electrodes, nipple (N) and cored electrodes (C_1, C_2, C_6)

dicators during melts with monolithic and cored electrodes in regular modes, on short and long arcs, on reduced and increased voltages of arcs, determination of arc length before break, etc. As an example, Figure 8 shows generalized data on specific consumption of active electric power for monolithic (M_1 and M_2) electrodes, nipples (N), hollow electrode (H), cored electrodes (C_1, C_2 and C_6) in serial modes.

From Figure 8, it follows that regardless of the cores composition (C_1, C_2 and C_6), cored electrodes provide lower electric power consumption than monolithic, hollow electrodes and nipple.

The summary data on the use of cored electrodes compared to monolithic electrodes during remelting and refining of 70FeSiMn in a 12-t EAF DC are presented in [10, 11] and are the following: a stable arc in a wide range of changes in electrical modes and arc length; savings of active electric power to 10 %; reduction of reactive power to 23 %; increase in the furnace output to 12 %.

These results served as a convincing ground to use cored electrodes to remelt more complex, multifractional, heavy charge in the EAF DC-12 furnace. Such a charge was a catalyst — a product of oil refining. Its base is $A1_2O_3$. The catalyst also contains a large number of nickel, molybdenum (10–12 % of each element), vanadium. The peculiarity is the high content of sulfur (up to 4–6 %) and a high residual content of oil products. The main purpose of remelting of this material was to obtain the maximum content of molybdenum and nickel (ingots), as well as to produce a slag with a high content of V_2O_5 (more than 12 %) for the production of 50 % FeV. The preliminary preparation of the catalyst was not carried out before melting, which caused extremely unstable electrical and technological modes and, as a consequence, technical and economic indices of melting. Against this background, the testing of cored electrodes efficiency was of great interest. The work included three stages.

Stage 1. Remelting of the catalyst with the production of vanadium-containing slag and metal phase (ingots) containing Ni and Mo.

Stage 2. Refining of the ingots and obtaining a product with the highest possible content of Ni and Mo.

Stage 3. Obtaining of ferrovanadium.

As an example, Figure 9 shows the comparative results of the catalyst remelting on the monolithic and cored electrodes of the compositions C_2 and C_{11}.

From Figure 9 it follows that the furnace output when using cored electrodes grows by 25.6 %, a decrease in the burning loss of Ni, Mo and Fe is up to 9 %, savings of electric power are up to 30 % depending on the composition of cores.

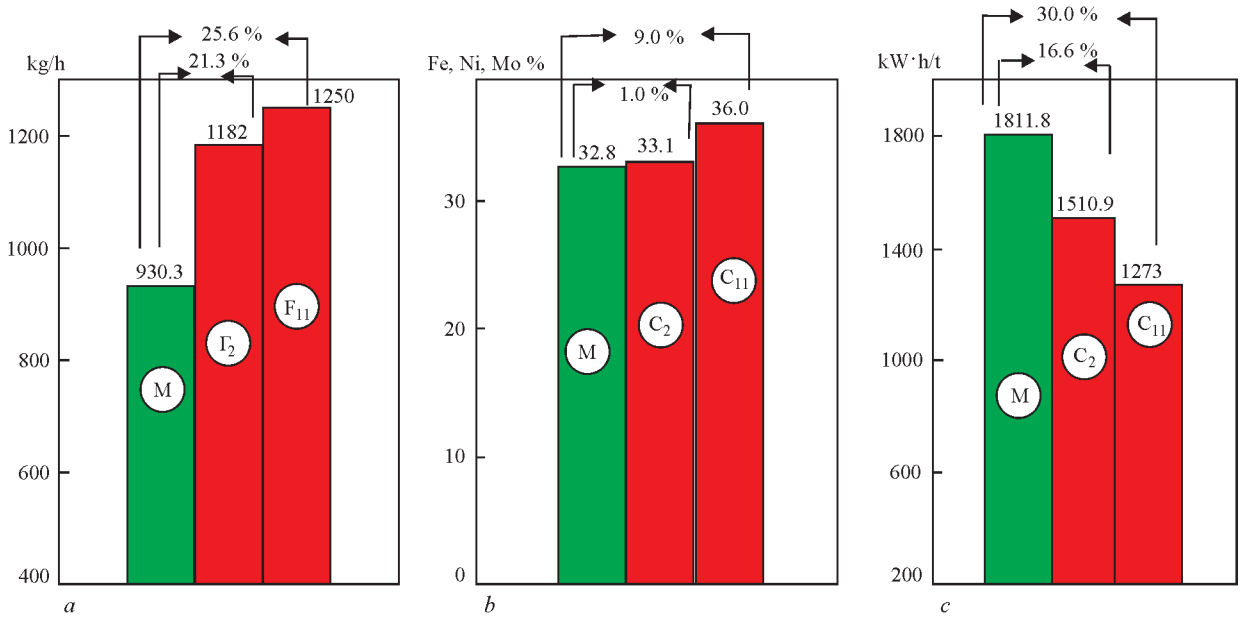

Figure 9. Furnace output (*a*), output of the metal phase (reduction in the burning loss of Fe, Ni, Mo), % (*b*) and electric power consumption (*c*) during remelting of the catalyst with the use of monolithic (M) and cored (C_2 and C_{11}) electrodes

Stage 2. During remelting of the metal phase, the use of the cored electrodes provided an increase in the furnace output by 9.6 %, a decrease in the burning loss of nickel and molybdenum by 10.3 % and saving of electric power by 2.8 %.

The similar results were obtained during smelting of 50 % FeV: the output increased by 4.2 %, the removal of vanadium form the slag increased by 17.4 % and saving of electric power were 7.1 %.

First of all, these data indicate that the electrode with a core at all stages of remelting the catalyst and its products have significant advantages compared to monolithic electrodes.

A significant advantage of cored electrodes is also the fact that when using time scattering, the melting decreases by 2.0–2.5 times, i.e., high stability of electrical modes and thermal conditions of the furnace output is provided.

As was noted, an important difference of cored electrodes is that during melting, the working end of such an electrode always has the shape of a concave hemisphere regardless of the core composition and electrical modes. This hemisphere causes the presence of close and open parts of the arc, the length of which can be adjusted. This causes two main technological factors. First, it can concentrate up to 50 % of the arc power. This in combination with the high stability of long arcs on the cored electrodes provides effective melting of a large-sized charge, a smaller number of arc breaks during penetration of wells, etc. Secondly, we assume that the consumption of refractories should be reduced

Table 4. Basic technical and economic parameters of operation of industrial EAF and EAF DC furnaces with cored electrodes*

	Melting parameters	12-ton EAF DC, electrode diameter of 350 mm	6-ton EAF, electrode diameter of 3×300 mm	50-ton EAF, electrode diameter of 3×508 mm
POWER	Arc stability	High	High	High
	Reactive power	Up to 23 %	–	–
	Increase in cosφ	From 0.88 to 0.94	From 0.81–0.86 to 0.91–0.94	–
	Reduction in time from the first short-circuit to a steady arc burning	By 2.4–4.8 times	By 2.75–5.4 times	–
	Reduction in time of arc stabilization on the wells and during charge melting	By 1.8–2.6 times	By 2.3–3.8 times	By 2.0–2.5 times
	Reduction in frequency and strength of surges into the primary mains	Significant	Significant	Significant
	Reduction in coefficients of current harmonics when penetrating wells and in liquid metal	–	From 0.65–0.59 to 0.28–0.09	From 0.9; 3.4; 1.1 to 0.3; 0.2; 0.3 respectively
	Reduction of the range of currents scattering by phases in the period of wells penetration and charge melting	–	By 25–40 %	By 30–50 %
	Distortion of sinusoidal curves of current and voltage in the basic periods of melting	–	Much lower	Much lower
	Reduction in the voltage and current fluctuations range	Voltage by 15 %, current by 31 %	–	–
TECHNOLOGY	Reduction in specific active electric power consumption (average), kW·h/t (%)	16.6–30.0 %	In average by 10 %	7–14 %
	Reduction in time of melt scattering (increase in stability)	2.0–2.5	1.5–2.0	2.0–2.5
	Increase in the furnace output, kg/h	Up to 25 %	By 23 %	By 18–22 %
	Reduction in burning loss of alloying elements (Mo, Ni, etc.)	Up to 10.3 %	–	–
	Reduction in overall burning loss of charge	Up to 3 %	Up to 2–3 %	Up to 3.5 %
	Reduction in specific consumption of cored electrodes of EG grade (in average), kg/t	–	By 18 %	By 16 %
METALLURGY	Reduction of nitrogen content in steel (in average)	–	By 15 %	By 19 %
ECOLOGY	Reduction in the noise level of furnace	By 7–10 %	By 8–10 %	By 7–10 %
	Reduction in the amount of dust and gas emissions	By 8–12 %	By 7–12 %	By 10–15 %
*Comparison is made with monolithic electrodes.				

by 20–30 %, a number of furnace repairs should decrease and its overall output should grow.

It was also confirmed that the cored arc causes a reduction in the noise level during operation of EAF DC-12 by 10–12 %. More detailed results of using cores in DC furnaces are presented in [7, 8, 10, 11] and in the summary Table 4.

RESULTS OF USING CORED ELECTRODES IN INDUSTRIAL AC FURNACES

Currently, about 1200 electric arc furnaces are being operated in the world: 200 DC and 1000 AC furnaces, including the most common industrial furnaces with a capacity from 6 to 50 t (old furnaces) and 100–180 t furnaces of ultra-high capacity, which have been installed recently in different countries of Europe, Asia and America. Therefore, the possibility of using cored electrodes in AC furnaces is of great interest. The first melts of the kind were carried out in an industrial three-phase 6-ton EAF DS-6N1 furnace.

The wastes from abrasive cleaning of high-cut steels and heat-resistant alloys with large scraps of carbon and ball-bearing ShKh15 steels were exposed to remelting. In the process of works, the electrodes with cores of five compositions (C_{16}, C_{18}, C_{19}, C_{20} and C_{21}) were tested. The melts were carried out with different combinations of cored and monolithic electrodes operating in the furnace simultaneously: three cored; two cored and one monolithic; one cored and two monolithic.

For adequate comparison of the results, the melts were carried out on regular electrical modes with registration of current, arc voltage values and other parameters.

As in the case of DC furnaces, the high stability of all electrical mode parameters in the DS-6N1 furnace was immediately noted. It was found that: the time of arc stabilization from the first interfacial short-circuit to continuous burning in the cored electrodes is 1.75–5.40 times shorter than in the monolithic electrodes; the time of frequent arc breaks in the cored electrodes is 3–10 times shorter than in the monolithic electrodes.

These factors determine quick stabilization of the electrical melting mode, rapid formation of wells and efficient melting of the charge. This also results in a decrease in the frequency and strength of current surges into the primary mains, which improves the quality of electric power, providing more stable operation of such powerful electric power consumers as neighbooring furnaces, units for out-of-furnace treatment, mill rolls, etc.

In more detail, the results of experimental melts in the DS-6N1 furnace are outlined in [12, 13] and a summary Table 4.

Further, the experimental works were carried out in a 50-ton three-phase AC furnace of DSV-50 type, which uses graphitized electrodes with a diameter of 508 mm.

The works program included an assessment of the impact of a large-scale factor on the technical and economic indices of 6- and 50-t EAF, the operation of the furnace in continuous mode (melting by melting) for 8 days, the features of the furnace operation on long arcs, control of parameters of electric and technological modes of melting, etc. For this purpose, 24 electrodes of 508 mm diameter with cored inserts of four compositions (C_{18}, C_{22}, C_{23} and C_{27}) were made. For the correct comparison of the results, the melts were carried out on regular electrical modes. Also current and voltage oscillograms were recorded, some of which were made on long arcs and reduced currents. In total, with the use of cored electrodes, 1968 t of carbon, low-alloy high-strength structural and alloyed tool steels were smelted.

The obtained results convincingly indicate the high efficiency of using cored electrodes when smelting the entire assortment of structural and tool steels on both regular and experimental modes. These results are outlined in [9] and a summary Table 4.

CONCLUSIONS

1. It is stated that in recent decades, the world production of steel has increased continuously and is getting very close to 2 bln t in 2021. This is 2.86 times more than in 1970 (0.7 bln t). About 30 % of steel is produced in EAF AC and EAF DC arc furnaces. By the end of the decade, this index will grow to 40 %. Moreover, much attention is paid to green technologies and use of hydrogen instead of carbon.

2. It was established that equal lengths of the arcs of the cored and monolithic electrodes are ensured at a voltage on the arc of the cored electrodes approximately twice shorter than the arc of the monolithic electrodes at equal currents.

3. The arc of the cored electrode is always stable, disoriented, it does not migrate along the end of the electrode and has much larger sizes than the arc of the monolithic electrode. Therefore, all specific parameters (electric current density, power) of the cored electrode arc are much lower than in the monolithic electrode arc.

4. It has been shown for the first time that the voltage drop on the cathode spot of the cored electrode arc is 2–3 times lower than on the cathode spot of the monolithic electrode arc.

5. It was found that at equal voltages on the arcs (of the cored and monolithic electrodes), the length of the cored electrode arc is in average 1.5 times larger than of the monolithic electrode.

6. It was found that the voltage drop on the anode spots of the cored and monolithic electrodes is approximately the same.

7. The current of emitters contained in the core can amount to 25–43 % of the working melting current.

8. The specific electrical resistance of cores before a temperature of 1200–2500 °C is always higher than that of the electrode. After the range of 1200–2500 °C, SER of cores becomes equal or lower than that of the electrode body. This temperature range is purely indicative because SER depends on the core composition, the completion of mutual diffusion processes in the core-electrode system, the actual state of physicochemical processes in this system, etc.

9. It is shown that the mutual diffusion of components in the core-electrode system increases the isotropicity of SER of this system.

10. The cored graphitized electrodes provide high stability of the arc and improve all the main power, technological and metallurgical parameters of operation of steel-making arc furnaces.

11. The cored electrodes provide a reduction in the noise level by 7–10 % and emissions of dust and gases into the atmosphere by 7–15 %.

12. The efficiency of cored electrodes does not depend on the design of the arc furnace, the type of current (direct or alternating), as well as the capacity of the furnace.

13. The production of cored electrodes does not require significant capital costs and can be organized either at a steel-making enterprise or at an enterprise manufacturing graphitized electrodes.

REFERENCES

1. Dyudkin, D.A., Kisilenko, V.V. (2008) *Steel-making.*Vol. 1. Moscow, Teplotekhnik [in Russian].
2. (2013) "*Steeltime*" *— Information portal about ferrous and nonferrous metallurgy.*
3. Belkovsky, A.G., Kats, Ya.L., Krisnyanskiy, M.V. (2012) State-of-the-art and trends of development of steel-making technology in arc steel-making furnaces and their design. *Staleplavilnoe Proizvodstvo,* **8**, 15–18 [in Russian].
4. Grishchenko, S.G., Granovsky, V.K. (2015) Metallurgy of the world and Ukraine in 2015. Problems and prospects. In: *Proc. of Int. Sci.-Tekh. Conf., National Metallurg. Academy of Ukraine, Dnepropetrovsk, Ukraine, 9–11 December, 2015*, 23–26 [in Russian].
5. *Analysis of market and market share of graphitized electrodes — Tendencies of growth and forecasting (2024–2029)* "*Mordor-Intelligence*".
6. Panov, E.N., Pedchenko, A.Yu. (2014) Analysis of development of Kastner graphitization furnaces under the conditions of modern market demands. *Tekhnologicheskii Audit i Reservy Proizvodstva,* 4(**1**), 57–60 [in Russian].
7. Paton, B.E., Lakomsky, V.I., Galinich, V.I., Mishchenko D.D. (2011) Cored electrodes of electric arc furnaces. *Chyornye Metally,* **5**, 13–15 [in Russian].
8. Bogachenko, A.G., Mishchenko, D.D., Braginets, V.I. et al. (2016) Cored graphitized electrodes. Electric arc furnaces of direct current (EAF DC). Saving of electric power. In: *Proc. of Medovar Memorial Symp., 7–10 June, Kyiv, Ukraine, 2016*, 185–193 [in Russian].
9. Bogachenko, O.G., Chernyakov, A.V., Goncharov, I.O. et al. (2024) Application of graphitized cored electrodes in 50-ton steel melting AC arc furnace of DSV-50 type. *Suchasna Elektrometal.*, **1**, 32–39 [in Ukrainian]. DOI: https://doi.org/10.37434/sem2024.01.04
10. Bogachenko, A.G., Mishchenko, D.D., Goncharov, I.O. (2023) Efficiency of using cored graphitized electrodes on electric arc furnaces of direct current. *Advances in Materials Sci.,* Vol. 23(**1**)(75), March**,** 82–97. DOI: http://dx.doi.org/10.2478/adms-2023-0006
11. Bogachenko, O.G., Mishchenko, D.D., Honcharov, I.O. et al. (2023) Application of graphitized wick electrodes in DC arc steel furnaces. *Suchasna Elektrometal.,* **1,** 53–61 [in Ukrainian]. DOI: https://org/10.37434/ sem2023.01.07
12. Paton, B.E., Bogachenko, O.G., Kyiko, S.G. et al. (2021) Experience of application of graphitized wick electrodes in industrial steel-making AC furnace. *Suchasna Elektrometal.,* **1,** 48–3 [in Ukrainian]. DOI: https://org.37434/sem/2021.01.06
13. Bogachenko, A.G., Sidorenko, L.A., Goncharov, I.O. et al. (2023) Technical-economic indices of operation of AC steel-making furnace with application of cored electrodes. *The Paton Welding J.,* **4**, 54–59. DOI: https://org/10.37434/tpwj2023.04

ORCID

O.G. Bogachenko: 0000-0002-3306-6626,
D.D. Mishchenko: 0000-0003-3612-1819,
I.O. Goncharov: 0000-0003-2915-0435,
I.O. Neilo: 0009-0003-4771-3630,
M.M. Gasik: 0000-0002-5782-7987,
S.G. Kiiko: 0000-0002-1161-5866

CONFLICT OF INTEREST

The Authors declare no conflict of interest

CORRESPONDING AUTHOR

O.G. Bogachenko
E.O. Paton Electric Welding Institute of the NASU
11 Kazymyr Malevych Str., 03150, Kyiv, Ukraine.
E-mail: E-mail: stemet@ukr.net

SUGGESTED CITATION

O.G. Bogachenko, D.D. Mishchenko, I.O. Goncharov, I.O. Neilo, M.M. Gasik, S.G. Kiiko, I.M. Logozinskyi, K.M. Gorban (2024) Composite (cored) graphitized electrodes for industrial DC and AC steel-melting furnaces. *The Paton Welding J*., **8**, 26–35.
DOI: https://doi.org/10.37434/tpwj2024.08.04

JOURNAL HOME PAGE

https://patonpublishinghouse.com/eng/journals/tpwj

Received: 29.04.2024
Received in revised form: 07.06.2024
Accepted: 22.08.2024

DOI: https://doi.org/10.37434/tpwj2024.08.05

METHODS FOR RECOGNIZING SURFACE DEFECTS ON THIN-SHEET MATERIALS FOR VISUAL TESTING AUTOMATION (REVIEW)

A.S. Novodranov

E.O. Paton Electric Welding Institute of the NASU
11 Kazymyr Malevych Str., 03150, Kyiv, Ukraine

ABSTRACT

The use of methods for recognizing surface defects in order to automate the process of visual non-destructive testing in production of rolled thin-sheet materials is becoming an increasingly urgent task. The use of automated systems for recognizing surface defects leads to early detection of damage and determination of their class and level of danger. After classifying a defect, the system makes a decision on further actions without the operator participation. The presence of such systems prevents the equipment downtime and reduces the impact of the human factor on production. The classifier performance rates were determined and analysis of the current techniques for determining surface defects was performed. The advantages and disadvantages of the methods are determined. The feasibility of using a method was analyzed depending on the type of surface and geometric characteristics of a defect. The expediency of using several methods to ensure more accurate recognition of surface defects is determined. Significant prospects for the application of machine learning methods based on neural networks are noted. The prospect of using neural networks in the systems for automated recognition of surface defects is predetermined by the possibility of automatic selection of features from the image, as well as processing of complex structures.

KEYWORDS: surface defects, defect detection methods, sheet materials, automated monitoring, defect recognition, image processing

INTRODUCTION

The intensive development of industry specifies the task of improving the quality of products. Due to this reason, automated monitoring of surface defects of thin-sheet materials is important in many industries [1–4]. The quality of thin-sheet products is determined by a number of mechanical characteristics and the presence of defects depending on the material from which it is made. The presence of defects leads to the downtime of production equipment due to the need in the shutdown of the forming machine, elimination of break or defect, which is negatively reflected in the efficiency of production. At the same time, modern computer technologies and methods of artificial intelligence make it possible to achieve a significant effect at improvement of control systems. Detection of minor defects in the early stages of production can prevent the appearance of rejection and ensure the compliance of products with the quality standards. The use of industrial cameras of GigE standard allows transmitting RAW images without compression to a server at a speed of up to 5 Gbps for further processing and analysis [5]. With the use of the methods for detection and recognition of surface defects based on statistic data, namely size, frequency of detection and type of defects, spectrum of brightness or color, as well as machine learning, it is possible to detect and classify defects by their degree of danger with high accuracy.

The term "accuracy of detection" should imply the correct assessment of a defect, namely the ability of the method to detect whether a defect is present on the obtained image. In this case, the accuracy of the classification reflects how true the method determines the class of a detected defect. According to the classification results, the automated system takes a decision on further steps.

AIM OF THE WORK

is analyzing and systematizing the methods of automated recognition of surface defects on thin-sheet materials to determine their advantages, disadvantages and potential areas of application.

STATEMENT OF PROBLEM FOR RECOGNITION AND CLASSIFICATION OF DEFECTS

Two-dimensional color image of the thin-sheet material surface serves as the primary information in the problem of recognition and classification of defects. The images are obtained by scanning the surface with the use of the system of digital CCD cameras. The size and shape of defects typical for respective production can be significantly different. In the general case, automated systems for monitoring of the thin-sheet material surface are capable of detecting defects from 1–2 mm^2. To check the recognition quality of the methods, a magnified image of a through defect in a rolled paper web with a size of 5.8×30.9 mm was

used. To detect defects in the sheet materials from their digital images, widespread methods were selected based on statistic data analysis, as well as methods based on spectral analysis were determined, that are less widespread in the solution of machine vision problems. Unlike the traditional recognition methods, the methods based on machine learning were chosen.

CLASSIFIER PERFORMANCE RATES

Assessment of the results of applying methods for detection of surface defects occurs on the basis of the following statistical categories (Figure 1):

- TP is a true positive, that indicates that a real defect is determined as a defect;
- TN is a true negative, that indicates that a real defect is determined as a background;
- FP is a false positive, that indicates that a background is mistakenly determined as a defect;
- FN is a false negative, that indicates that a real background is correctly determined as a background.

TP, FN, TN and FP categories are generally accepted and widely used in many fields of science, including machine learning and computer vision [7]. Therefore, for a high percentage of detecting surface defects, it is necessary that TP and FN categories prevail. If TN and FP prevail among the detection categories, the appropriate detection algorithms and/or methods should be improved. Based on the above-mentioned categories, the classifier performance rates can be calculated:

- True positive rate:

$$TPR=\frac{TP}{TP+FN}; \quad (1)$$

- True negative rate:

$$TNR=\frac{TN}{TN+FP}; \quad (2)$$

- False positive rate:

$$FPR=\frac{FP}{FP+TN}; \quad (3)$$

- False negative rate:

$$FNR=\frac{FN}{FN+TP}; \quad (4)$$

- Precision rate:

$$Precision=\frac{TP}{FP+TP}; \quad (5)$$

- Recall rate:

$$Recall=\frac{TP}{TN+TP}; \quad (6)$$

- Accuracy rate:

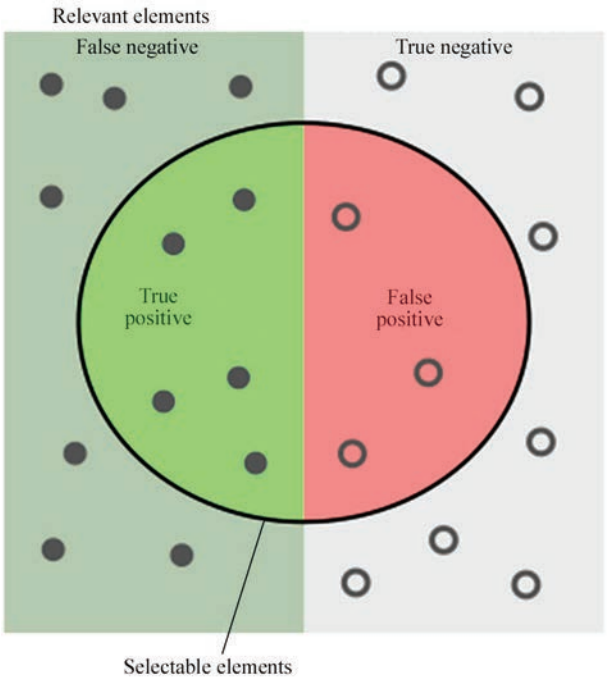

Figure 1. Confusion matrix [6]

$$Accuracy=\frac{TP+TN}{TN+TP+FP+FN}; \quad (7)$$

- G-mean:

$$G_{mean}=\sqrt{TPR\cdot TNR}; \quad (8)$$

- F-measure:

$$F_{measure}=\frac{2Precision\cdot Recall}{Precision\cdot Recall}. \quad (9)$$

Among these rates, G-mean and F-measure should be especially noted. G-mean is a value that estimates accuracy based on true positive and true negative rate. F-measure determines the overall efficiency of the process of detecting surface defects based on recall and precision parameters. The highest rate of F-measure is 1, which indicates the perfect precision and recall.

METHODS FOR RECOGNIZING SURFACE DEFECTS

The general classification of methods for recognizing surface defects is shown in Figure 2. In order to ensure the most effective level of recognizing defects, it is expedient to combine these methods and approaches depending on the task and production conditions.

1. STATISTICAL APPROACHES

The use of statistical approaches is justified in those cases, when the nature of defects is related to the surface texture. Therefore, the detection, description or classification of features on the base of textured surface characteristics, such as entropy, contrast, correla-

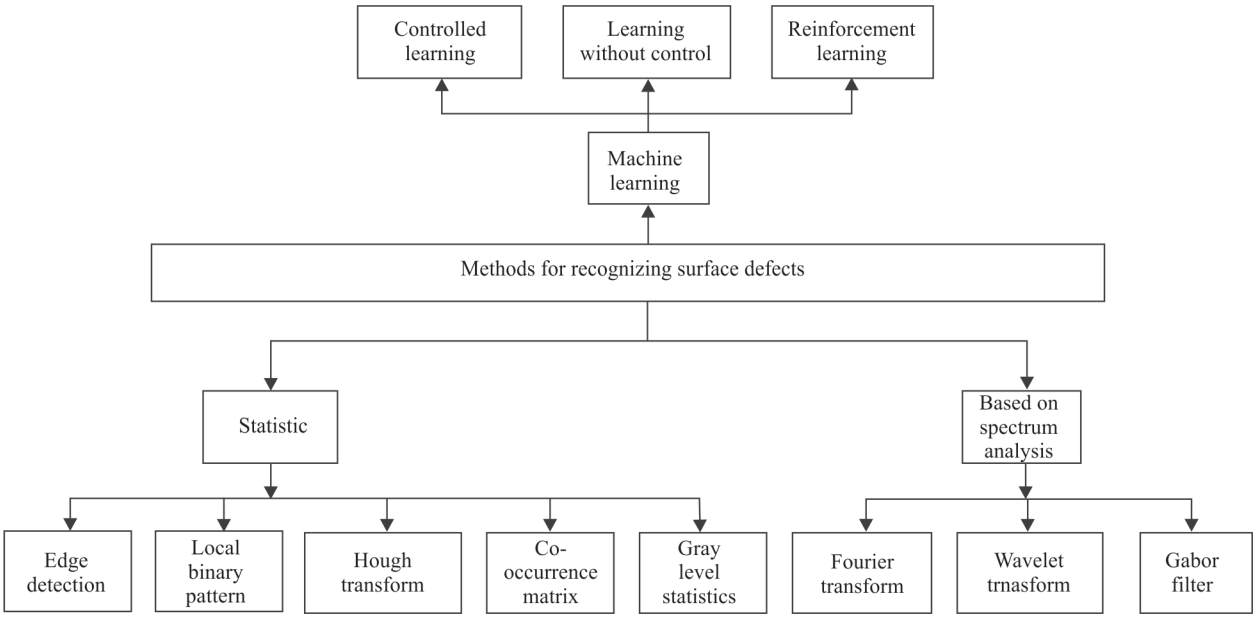

Figure 2. Classification of methods for recognizing surface defects

tion, etc., is an important element of the problem of recognizing surface defects [8].

1.1. METHOD OF EDGE DETECTION

An important step in recognizing defects on RAW images is the method of edge detection. There are several operators (Figure 3) to detect the edges of surface defects in the images.

Sobel operator is one of the most popular. To detect horizontal and vertical edges, it uses kernel convolution. Among the advantages of this operator, its simplicity of implementation, as well as a short time of performance should be attributed [9, 10]. However, the roughness of detection edges compared to the next operator should be noted, namely Canny operator [11]. At the first stage during its application, the

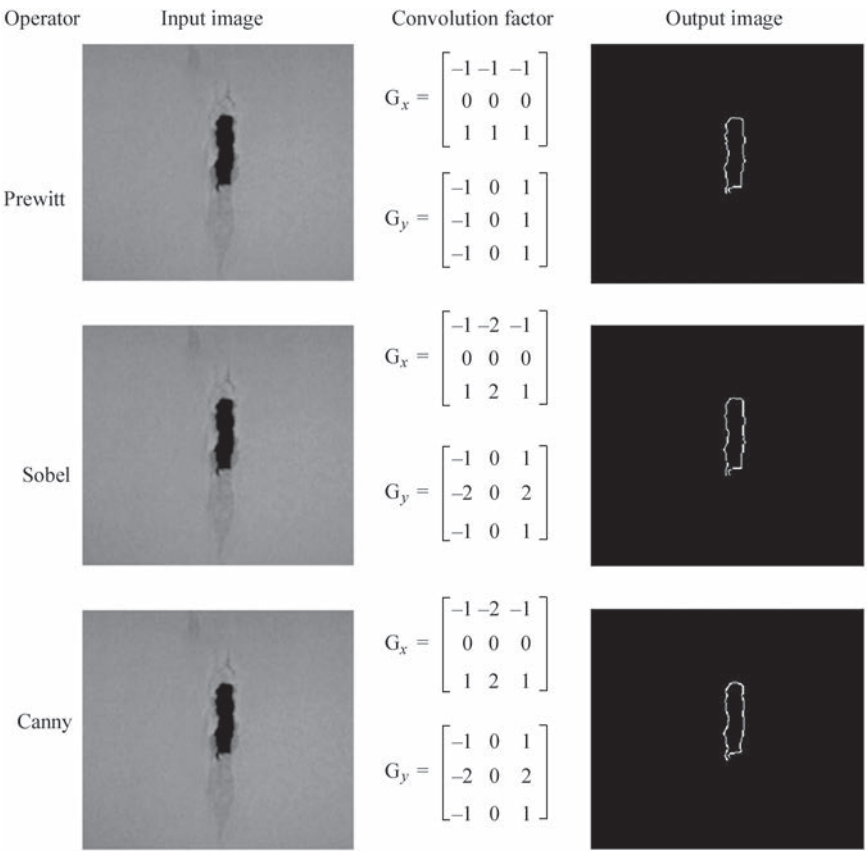

Figure 3. Result of using operators for edge detection

Table 1. Values of metrics for quality assessment of recognizing the considered methods

Number	Method	F-measure	Accuracy, %	Precision, %	Recall, %	Running time, ms
1	Edge detection					
	Canny operator	0.96	93.00	96.79	95.44	8.57
	Prewitt operator	0.92	92.34	92.34	90.83	4.12
	Sobel operator	0.86	81.00	85.41	86.67	5.36
2	Local binary pattern	0.83	82.00	84.51	81.70	21.41
3	Hough transform	0.78	72.00	75.57	80.18	27.49
4	Co-occurrence matrix	0.74	73.00	73.46	74.71	24.85
5	Gray level statistics	0.69	66.00	69.26	69.26	11.51
6	Fourier transform	0.65	63.00	65.77	64.72	36.21
7	Wavelet transform	0.85	82.00	88.85	80.69	67.32
8	Gabor filter	0.85	81.00	84.14	85.44	81.92
9	Supervised learning	0.94	93.00	95.00	93.58	12.38*

*Runnin time without taking into account the time for neural network learning.

image is smoothed. Then, a gradient of brightness is calculated for each image pixel. At the next stage, not maximum suppression and threshold value are used to obtain more smooth edges compared to Sobel operator. Among the disadvantages, the complexity of performance, as well as longer time for performance should be attributed. Sobel operator is similar to Prewitt operator. The use of a convolution to detect changes in brightness in the images is the same for these methods. Among differences, different characteristics of the kernel, less sensitivity to changes in intensity, as well as the smaller value of the Prewitt operator gradient can be attributed [12]. Sometimes, Roberts operator is also used, which is one of the simplest methods of detecting edges, Kirsch operator, as well as Laplace operator.

Quantitative characteristics of recognition quality using the method of highlighting edges is shown in the Table 1.

1.2. LOCAL BINARY PATTERN

The use of the local binary pattern (LBP) method has the most effective result of recognizing surface defects when they affect the textured characteristics of the surface. The essence of the method (Figure 4) is to determine a local surrounding context for each pixel of the image. In the next step, the brightness parameter of the central pixel is compared with the brightness of the pixels of the selected context. Next, a binary pattern is created for each pixel by setting the value "1" in the case when the brightness of the central pixel is less or equal to the brightness of the current value, as well as by setting "0" in other case. Next, for each image area, a histogram of LBP codes is created. This histogram reflects a number of each LBP code in the corresponding area [13–15]. The significant advantage of the LBP method is the ability to determine texture changes in the image. A high rate of calculations should also be noted.

Quantitative characteristics of recognition quality using the local binary pattern method are shown in the Table 1.

1.3. HOUGH TRANSFORM

This statistical approach is used to detect straight lines, round or ellipsoidal shapes in the image. The straight line detection algorithm is composed of the following steps. In the first step, each point of the image is transferred to the parametric space. In such a space, a straight line is represented by two values: an angle of inclination and a distance to the beginning of coordinates. In the second step, for each point of the image, a diagram is built in the parametric space. This diagram will display a hypothetical line crossing the current point. In the case when several points of the image lie on one straight line, their diagrams in the parametric space are intersected at one point. Programming of such an algorithm for highlighting of straight lines is based on the analysis of the above-mentioned intersections in the parametric space [16, 17]. To detect round shape objects in the image, a three-dimensional space for the mentioned algorithm

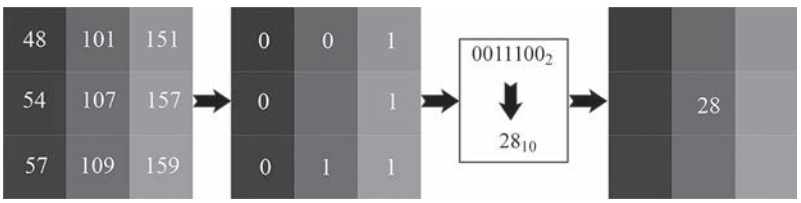

Figure 4. Principle of using LBP method

is used, in which objects to be detected will be represented by the coordinates of the center and the radius. Regarding the detection of ellipsoidal objects, in this case an object to be detected will be represented by the coordinates of the center, ellipse axis and angle of inclination.

Quantitative characteristics of recognition quality using the Hough transform method are shown in the Table 1.

1.4. CO-OCCURRENCE MATRIX

The co-occurrence matrix is a data structure used to assess the degree of similarity or coincidence between the areas or patterns of an image in the process of detecting surface defects. When applying this method, at first, textured characteristics, color information, shape, size and other attributes from images are distinguished, that may indicate surface defects. The selected features are compared with the features of reference patterns, which are created in advance on the basis of information about the types of defects. At the next step, a matrix for each image area is created, each cell of which contains comparison values. Next, the obtained matrix is analysed to detect coincidence with reference patterns [18]. Based on the analysis of the co-occurrence matrix, the system can make decisions on the presence of a defect and plan further actions.

Quantitative characteristics of recognition quality using the co-occurrence matrix are given in the Table 1.

1.5. GRAY LEVEL STATISTICS

The use of gray level statistics is justified in the case when the brightness and contrast of the defect zone is different from the surrounded area. Depending on the problem, this method can be used both independently as well as in combination with other methods for better results of detecting surface defects. One of the most popular methods is determination of the brightness threshold. By determining a threshold value of the gray level and highlighting all the pixels, the brightness of which exceeds this value, probable surface defects can be highlighted, the brightness of whose pixels is different from the surrounding pixels. At the next step, the obtained histograms for determination of texture features of the image are analyzed. Based on the results of the analysis, it is possible to determine textured features that may be superficial defects. To increase the probability of a defect based on the textured surface features, it is expedient to apply one of the methods of neural networks [19, 20]. Sometimes, the method of changing contrast is also used. The essence of this method consists in comparing the contrast of pixels of a probable defect and the surrounding area. A high level of contrast may indicate a surface defect. Quantitative characteristics of recognition quality using the gray statistics method are shown in the Table 1.

Among the disadvantages of statistical methods, unreliability in the case of light changes, as well as interference of pseudo-effects can be attributed.

2. METHODS BASED ON SPECTRUM ANALYSIS

These methods are used to determine and analyze the frequency characteristics of textured features of surface defects of thin-sheet materials.

2.1. FOURIER TRANSFORM

Fourier transform method is often used to analyze the frequency characteristics of textures and details on the images of surface defects. The essence of the method is the transition from the spatial representation of the image to the frequential representation. This transformation allows analyzing an image in the frequency range, as well as selecting the basic frequencies in the image that will be useful in highlighting edges and textures. As a result of this transformation, an image spectrum in the form of two-dimensional matrix is obtained, which contains information about the frequency components and their phase-frequency characteristics. The next step is highlighting and recognition of defects on the image by analyzing the frequency characteristics of the spectrum. Due to the fact that defects can change the frequential composition of the input image, i.e., contain high-frequency components or noise, it provides the visibility of probable defects in the spectrum. The use of this transformation makes it possible to detect defects or changes in the structure by suppressing undesired components or enhancing the required frequencies. After analyzing the frequency characteristics, it is possible to return to the spatial image representation by means of the inverse Fourier transform. The next step is the use of the threshold filtration method for detection and classification methods to determine the type of a defect [21, 22]. As a disadvantage of the Fourier transform method, the inability to describe the spatial model of information signal should be mentioned. That is the reason for ignorance of the most information of a local description.

Quantitative characteristics of the recognition quality using the Fourier transformation method are given in the Table 1.

2.2. WAVELET TRANSFORM

This method of image analysis is quite powerful, and therefore is often used for the recognition of surface defects of thin-sheet materials. The essence of the method consists in decomposition of the input image by scales and orientations with the use of the wavelet

transformation. The result of the transformation are wavelet coefficients, presented in the form of scales and orientations of details of the input image. The filtration of the corresponding coefficients should be applied to highlight the required defects on the image. In the next step, the inverse wavelet transformation is performed to transform the image into a pixel system of coordinates. The result of the inverse transformation is an image with highlighted surface defects. In the case of insufficient intensity of highlighted defects, it is expedient to apply the method of threshold filtration. The final step is to apply the classification algorithms to determine the type and level of danger of a detected defect. This method makes it possible to recognize defects of different sizes by analyzing texture features, as well as localizing defects of different spatial frequency. The disadvantages of the method include sensitivity when choosing wavelets and decomposition parameters [23, 24]. The quantitative characteristics of recognition quality using wavelet transformation are shown in the Table 1.

2.3 GABOR FILTER

This method describes the spatial model of the information signal more effectively, compared to the method of Fourier transformation, by modulating the function of the Gaussian kernel with a sinusoidal wave of a certain frequency. In other words, Gabor filter is a mathematical filter that is used to analyze structural and textured surface defects. The essence of the method consists in determination of the filter parameters, such as frequency, orientation and size. On the basis of these parameters, the filter kernel is created, which is a two-dimensional function in the form of a sinusoidal wave limited by the Gaussian function. By means of the convolution operator, the obtained kernel of the function is applied to the image. This application helps to determine the texture and structural features by enhancing the textured details in the image corresponding to the filter frequency parameters. The use of the Gabor filter results in creation of a reaction map that reflects the degree of compliance of the textured features of each pixel of an image. Large values on this map can mean the presence of a surface defect. The reaction map is further processed using a threshold filtration method to highlight defect areas [25, 26]. Among the disadvantages of the method, its unortrogonality, resulting in excess components of features, which leads to a decrease in the efficiency of the textured image analysis, should be attributed. Quantitative characteristics of recognition quality using the Gabor filter are given in the Table 1.

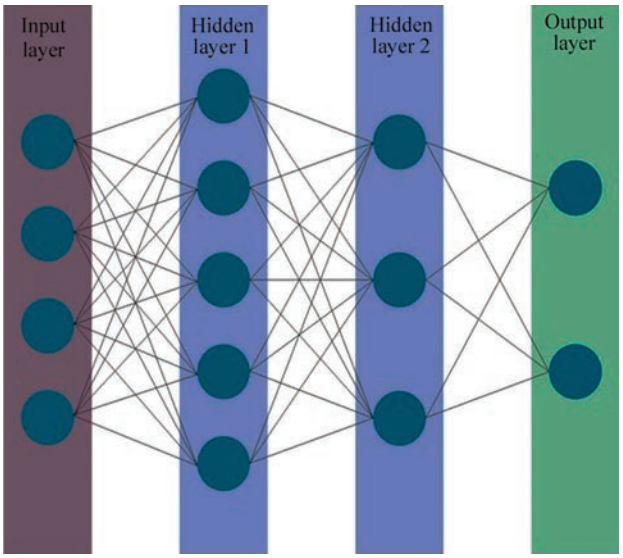

Figure 5. General structure of neural network [27]

3. APPROACHES BASED ON MACHINE LEARNING

Machine learning is a set of algorithms and methods of artificial intelligence (AI), by means of which a computer runs a self-learning process without direct instructions. To the main methods of machine learning, the following should be attributed:

- supervised learning or learning with a teacher;
- unsupervised learning;
- reinforcement learning.

The most used algorithm of machine learning is an artificial neural network. The use of a neural network requires a large amount of datasets for learning. Images with the required type of defects and without them serve as learning data. The required set of images with defects is selected depending on the material surface, on which recognition will be carried out. Typical defects for paper-cardboard production are web break, crumpling and defects of web edges, wandering crack, etc. In contrast to paper and cardboard production, typical defects for metal-rolled industries are scratches, corrosion and rust, exfoliation, traces of treatment, etc.

The neural network in the general case (Figure 5) consists of the input layer responsible for the normalization of data, a certain number of hidden layers that perform computing functions, as well as the output layer.

The methods of the neural network learning are divided into methods of direct and back error propagation. At the direct error propagation, the answer is directly predicted. At the back error propagation, the error between the answer and the prediction is minimized.

3.1. SUPERVISED LEARNING

The essence of the method consists in learning of a model with a teacher based on marked data, namely

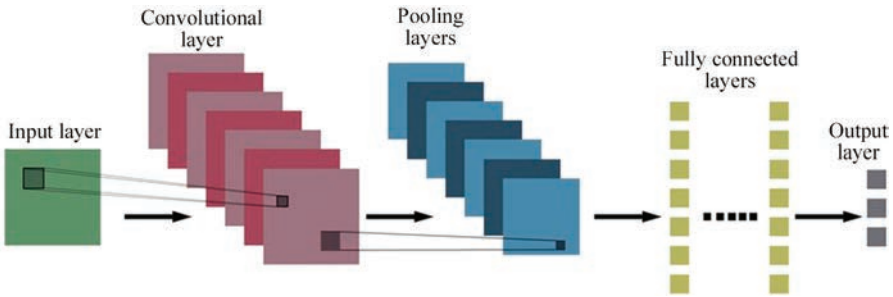

Figure 6. Typical architecture of CNN network [27]

samples having a known mark or class. Supervised machine learning is used to teach a model of surface defect classifier. At the first step, a database with images of product areas with typical defects indicating their type and coordinates (x, y) of the defect zone is created. At the second step, the selection of characteristic features from the images is carried out, that can be used to classify defects. The characteristic features include geometric or textured features, etc. Next, the appropriate model of machine learning is selected, namely CNN, SVM, RF, etc. After that, the process of model learning begins on the marked data using the extracted characteristic features of defects. During learning, a model of the neural network is adjusted to the characteristics of images that correspond to various classes of defects. Upon completion of the learning process, assessment of the accuracy of recognition is checked by means of a test dataset. In case of insufficient accuracy, repeated learning on another dataset is carried out until the required accuracy is achieved. The need in a large volume of quality data for learning can be attributed to the disadvantages of the method. Among the benefits, high accuracy at proper adjustment and learning should be mentioned [28, 29].

It should be noted that for the solution of computer vision problems, convolution neural networks (CNN) are best suited due to specialized architecture (Figure 6), scalability, as well as invariance to displacements and distortions. By means of the convolution layers, automatical selection of the features for detection of defects occurs. The next step is using subdiscretization layers to reduce data dimensions. To solve the problem of classification, pooling layers are used.

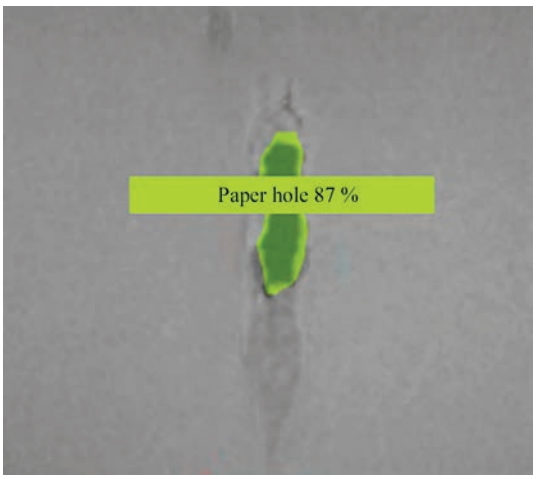

Figure 7. Result of detecting and classifying a defect with the use of the supervised learning method

Having selected a model of YOLOv4 neural network and having trained on a test sampling of images, containing typical defects of the paper web, the next result was achieved (Figure 7). The learning sampling of the marked data had 80 images. Test and validation samplings contained 10 images each. The availability of test and validation sampling is caused by the need in checking the adequacy of the learning process.

Quantitative characteristics of recognition quality using the supervised learning method are given in the Table 1.

3.2. UNSUPERVISED LEARNING

This method of machine learning accepts not marked data as input data. During learning, the model itself should find regularities or patterns without information about the classes of possible defects. The principle of clustering consists in seeking the model to independently group images by similar features without certain classes. The principle of reducing dimensions consists in preserving as much information as possible while reducing the dimensions of data. The use of the unsupervised method allows detecting hidden patterns or characteristics for further analysis or clustering of data, finding anomalies or associations. But there is a difficulty in determining the accuracy of detection due to the absence of "correct" answers [30].

3.3. REINFORCEMENT LEARNING

This method of machine learning consists in the interaction of the agent with the environment. The agent is a neural network that makes a decision based on input data. The agent receives a positive or negative assessment for made decisions. The main task of the agent is to maximize the positive assessments during learning and choose the optimal interaction strategy. The process of reinforcement learning of a neural network is based on the iterative interaction of the agent with the contacted environment. Thus, the agent learns at

his actions and also on the gained experience of interaction with the environment. This method is the most suitable for learning robots and autonomous systems for control of unmanned vehicles [31, 32].

It should be noted that unsatisfactory quality assessment metrics were obtained with the help of machine learning methods, namely, unsupervised learning and reinforcement learning, because of the complexity of architecture and, as a consequence, complex adjustment. In turn, it should be noted that the supervised learning method showed a high result of the recognition quality. However, the "confidence" parameter (Figure 7) was at a level of 87 %, which can be explained by not sufficiently large set of learning data. Each of the above-mentioned machine learning methods can be used together for a more effective learning process on a limited input dataset.

Quantitative characteristics of defect quality recognition on digital images using the considered methods are shown in the Table 1.

CONCLUSIONS

Based on the results of the analysis of methods for recognizing surface defects, it can be concluded that machine learning methods, namely, convolution neural networks are the best suited for the use in the automated systems for testing the quality of thin-sheet material production. The use of machine learning methods is perspecitve due to the automatic separation of features from the image, as well as the ability to process complex data structures. Among the disadvantages of these methods, the need for a large amount of data for learning should be attributed. However, the correctly adjusted neural network on the ascending array of data for learning will only increase the accuracy of recognition. The considered statistical approach methods, as well as methods based on the spectrum analysis, are expedient for the use in combination with other methods to achieve greater accuracy of recognition. In some cases, the use of the methods for detection of edges, gray level statistics, local binary pattern, etc. is rationally to use as a preliminary processing for the formation of a learning database for machine learning methods. The cases and circumstances were also determined, in which the use of one or other method is more appropriate for a number of reasons. For example, it was determined that the Hough transform method shows the highest efficiency in the recognition of geometric shapes on images such as lines, circles and ellipses.

REFERENCES

1. Lv, X., Duan, F., Jiang, J., Fu, X., Gan, L. (2020) Deep metallic surface defect detection: The new benchmark and detection network. *Sensors*, **20,** 1562. DOI: https://doi.org/10.3390/s20061562
2. Lv, X., Duan, F., Jiang, J. et al. (2020) Deep active learning for surface defect detection. *Sensors*, **20**, 1650. DOI: https://doi.org/10.3390/s20061650
3. Ghorai, S., Mukherjee, A., Gangadaran, M., Dutta, P.K. (2013) Automatic defect detection on hot-rolled flat steel products. *IEEE Transact. Instrum. Meas.*, **62**, 612–621. DOI: https://doi.org/10.1109/TIM.2012.2218677
4. Song, K., Yan, Y. (2013) A noise robust method based on completed local binary patterns for hot-rolled steel strip surface defects. *Appl. Surf. Sci.*, **285**, 858–864. DOI: https://doi.org/10.1016/j.apsusc.2013.09.002
5. Luo, Q., He, Y. (2016) A cost-effective and automatic surface defect inspection system for hot-rolled flat steel. *Robot. Comput. Integr. Manuf.*, **38**, 16–30. DOI: https://doi.org/10.1016/j.rcim.2015.09.008
6. Medium https://miro.medium.com/v2/resize:fit:640/format:webp/1*GDR0plA0fmHHbk9lZoGPBg.png
7. Alaa Tharwat (2020) Classification assessment methods. *Applied Computing and Informatics,* **17**, 168–192. DOI: https://doi.org/10.1016/j.aci.2018.08.003
8. Xuewu, Z., Fang, G., Lizhong, X. (2012) Inspection of surface defects in copper strip using multivariate statistical approach and SVM. *Int. J. Comput. Appl. Technol.*, **43**, 44–50. DOI: https://doi.org/10.1504/IJCAT.2012.045840
9. Shi, T., Kong, J., Wang, X., Liu, Z., Zheng, G. (2016) Improved sobel algorithm for defect detection of rail surfaces with enhanced efficiency and accuracy. *J. Cent. South. Univ.*, **23**, 2867–2875. DOI: https://doi.org/10.1007/s11771-016-3350-3
10. Borselli, A., Colla, V., Vannucci, M., Veroli, M. (2010) A fuzzy inference system applied to defect detection in flat steel production. In: *Proc. of the IEEE Int. Conf. on Fuzzy Systems, Barcelona, Spain,* 1–6. DOI: https://doi.org/10.1109/FUZZY.2010.5584036
11. Shen, Y. (2010) Techniques of machine vision applied in detection of copper strip surface's defects. *Electron. Meas. Technol*., **33**, 65–67. DOI: https://doi.org/10.1007/978-3-642-15621-2_34
12. Huang, X., Luo, X. (2014) A real-time algorithm for aluminum surface defect extraction on non-uniform image from CCD camera. In: *Proc. of the Int. Conf. on Machine Learning and Cybernetics (ICMLC), Lanzhou, China*, 556–561. DOI: https://doi.org/10.1109/ICMLC.2014.7009668
13. Ojala, T., Pietikainen, M., Harwood, D. (1996) A comparative study of texture measures with classification based on feature distributions. *Pattern Recognit.*, **29**, 51–59. DOI: https://doi.org/10.1016/0031-3203(95)00067-4
14. Song, K.C., Yan, Y.H., Chen, W.H., Zhang, X. (2013) Research and perspective on local binary pattern. *Acta Automatica Sinica*, **39**, 730–744. DOI: https://doi.org/10.1016/S1874-1029(13)60051-8
15. Liao, S., Zhu, X., Lei, Z. et al. (2007) Learning multi-scale block local binary patterns for face recognition. In: *Proc. of the Int. Conf. on Biometrics, Seoul, Korea*, 828–836. DOI: https://doi.org/10.1007/978-3-540-74549-5_87
16. Sharifzadeh, M., Alirezaee, S., Amirfattahi, R., Sadri, S. (2008) Detection of steel defect using the image processing algorithms. In: *Proc. of the 12th Int. Multitopic Conf., Karachi, Pakistan*, 125–127. DOI: http://dx.doi.org/10.1109/INMIC.2008.4777721
17. Bulnes, F.G., Garcia, D.F., Javier de la Calle, F., Usamentiaga, R., Molleda, J. (2016) A non-invasive technique for online defect detection on steel strip surfaces. *J. Nondestruct. Eval.*, **35**, 1–18. DOI: https://doi.org/10.1007/s10921-016-0370-8

18. Tsai, D.-M., Chen, M.-C., Li, W.-C., Chiu, W.-Y. (2012) A fast regularity measure for surface defect detection. *Mach. Vis. Appl.*, **23**, 869–886. DOI: https://doi.org/10.1007/s00138-011-0403-3
19. Choi, J., Kim, C. (2012) Unsupervised detection of surface defects: A two-step approach. *In: Proc. of the 19th IEEE Int. Conf. on Image Processing (ICIP), Lake Buena Vista, FL, USA*, 1037–1040. DOI: https://doi.org/10.1109/ICIP.2012.6467040
20. Djukic, D., Spuzic, S. (2007) Statistical discriminator of surface defects on hot rolled steel. *Proc. of Image and Vision Computing New Zealand 2007*, 158–163.
21. Ai, Y., Xu, K. (2013) Surface detection of continuous casting slabs based on curvelet transform and kernel locality preserving projections. *J. Iron Steel Res. Int.*, **20**, 80–86. DOI: https://doi.org/10.1016/S1006-706X(13)60102-8
22. Paulraj, M.P., Shukry, A.M.M., Yaacob, S., Adom, A.H., Krishnan, R.P. (2010) Structural steel plate damage detection using DFT spectral energy and artificial neural network. In: *Proc. of the 6th Int. Colloquium on Signal Processing & its Applications, Mallaca City, Malaysia*, 1–6. DOI: https://dx.doi.org/10.1109/CSPA.2010.5545247
23. Wu, X., Xu, K., Xu, J. (2008) Application of undecimated wavelet transform to surface defect detection of hot rolled steel plates. In: *Proc. of the 1st Int. Congress on Image and Signal Processing, Sanya, China*, 528–532. DOI: https://doi.org/10.1109/CISP.2008.278
24. Li, X., Tso, S.K., Guan, X., Huang, Q. (2006) Improving automatic detection of defects in castings by applying wavelet technique. *IEEE Transact. Ind. Electron.*, **53**, 1927–1934. DOI: https://doi.org/10.1109/TIE.2006.885448
25. Choi, D.C., Jeon, Y.J., Yun, J.P., Kim, S.W. (2011) Pinhole detection in steel slab images using Gabor filter and morphological features. *Appl. Opt.*, **50**, 5122–5129. DOI: https://doi.org/10.1364/AO.50.005122
26. Chol, D.C., Jeon, Y.J., Kim, S.H. et al. (2017) Detection of pinholes in steel slabs using Gabor filter combination and morphological features. *ISIJ Int.*, **57**, 1045–1053. DOI: https://doi.org/10.2355/isijinternational.ISIJINT-2016-160
27. Amirhossein Yazdani Abyaneh, Ali Hosein Gharari Foumani, Vahid Pourahmadi (2018) *Deep Neural Networks Meet CSI-Based Authentication*. DOI: https://doi.org/10.48550/arXiv.1812.04715
28. Kang, G.W., Liu, H.B. (2005) Surface defects inspection of cold rolled strips based on neural network. In: *Proc. of the 4th Int. Conf. Machine Learning Cybernetics, Canton, China*, 5034–5037. DOI: https://doi.org/10.1109/ICMLC.2005.1527830
29. Chen, F., Jahanshahi, M.R. (2018) NB-CNN: Deep learning-based crack detection using convolutional neural network and naive bayes data fusion. *IEEE Transact. Ind. Electron.*, **65**, 4392–4400. DOI: https://doi.org/10.1109/TIE.2017.2764844
30. Bulnes, F.G., Usamentiaga, R., Garcia, D.F., Molleda, J. (2012) Vision-based sensor for early detection of periodical defects in web materials. *Sensors*, **12**, 10788–10809. DOI: https://doi.org/10.3390/s120810788
31. James Lindsay, Sidney Gigivi (2020) A novel way of training a neural network with reinforcement learning and without back propagation. In: Proc. of the *Int. Joint Conf. on Neural Networks (IJCNN)*. DOI: https://doi.org/10.1109/IJCNN48605.2020.9207659
32. Seyed Sajad Mousavi, Michael Schukat, Enda Howley (2017) Deep reinforcement learning: An overview. In: *Proc. of the SAI Intelligent Systems Conf.*. DOI: https://doi.org/10.48550/arXiv.1701.07274

ORCID
A.S. Novodranov: 0000-0002-3380-3745

CORRESPONDING AUTHOR
A.S. Novodranov

E.O. Paton Electric Welding Institute of the NASU
11 Kazymyr Malevych Str., 03150, Kyiv, Ukraine.
E-mail: artur19940731@gmail.com

SUGGESTED CITATION
A.S. Novodranov (2024) Methods for recognizing surface defects on thin-sheet materials for visual testing automation (Review). *The Paton Welding J.*, **8**, 36–44.
DOI: https://doi.org/10.37434/tpwj2024.08.05

JOURNAL HOME PAGE
https://patonpublishinghouse.com/eng/journals/tpwj

Received: 26.03.2024
Received in revised form: 30.05.2024
Accepted: 22.08.2024

DOI: https://doi.org/10.37434/tpwj2024.08.06

ADDITIVE MANUFACTURING REVOLUTION IN THE CONTEXT OF TECHNOLOGY REVOLUTIONS

E. Balikci

Bogaziçi University, 34342, Bebek, Istanbul, Turkey

ABSTRACT

This article positions Additive Manufacturing (AM) within the broader context of historical technological revolutions, recognizing its transformative impact while acknowledging that future generations may perceive it as an early-stage technology. AM has evolved through several industrial revolutions, particularly benefiting from advancements in Artificial Intelligence (AI) and the Internet of Things (IoT). The convergence of traditional manufacturing techniques with these contemporary innovations has created a favorable environment for the widespread adoption of AM technologies. The article emphasizes the need for AM to fully embrace this integration to achieve its potential. The discussion highlights that the core objective of Focused Beam Additive Manufacturing (FBAM) is to control the solidification process, ensuring the production of sound and reliable components on the first attempt. Despite being a multidisciplinary technology, all relevant disciplines converge on achieving a flawless melting and solidification process. This involves precise modulation of energy sources, effective powder management, motion control systems, and temperature/environment regulation, all aimed at producing microstructurally and geometrically flawless components. The article concludes that the success of FBAM depends on the careful orchestration of these multidisciplinary activities, centered around a well-controlled solidification process, to deliver high-quality components that meet business needs.

KEYWORDS: technology revolutions, additive manufacturing, artificial intelligence, Internet of things

INTRODUCTION

It is common to hear people talk of technology revolutions when referring to computers, artificial intelligence (AI), additive manufacturing (AM), and many more. The word "revolution" refers to an abrupt change in the status quo of a social structure or technology. An example for the social structure change is the socialist revolution that started with the beginning of the 20th century and expanded to different parts of the world in that century. Another example is the revolution brought about by the Black Death, the plaque in the late 1340s. It wiped out half of the population from China to Europe situated around the Silk Rod [1]. Reactions from peoples and leaders of the time were similar to what was heard during the COVID19. Some tried to protect themselves, and others preached it was a punishment from God so there was nothing humans could do. Whatever the messaging was, the plaque had a huge social effect; an economically extractive system of serfdom diminished starting from western Europe, mainly in England.

Both of these social events can rightfully be described as a revolution with a major difference between the two. The socialist revolution was imposed by a leadership team everywhere it was implemented, whereas the disappearance of serfdom was driven by the serf peasants themselves but was aided by an unpredictable event that changed the social force balance. When half of the population was exterminated, the survivors were at a better position to bargain for their labor. In fact, the peasant revolution had far reaching impacts on future social struggles, including the socialist revolution whose style of implementation was experimentally proven unsuccessful. False, under calculated, or over promised ideals were not sustainable.

Technology revolutions actually do not happen abruptly. They are rather a result of a series of evolutions in multiple technological fronts taking place in an unseen backstage. For example, what dazzles people as AI today has essentially evolved on algorithmic statistics, data science, and computers over decades [2].

Social and technology revolutions can have mutual influences. COVID19, for example, has initiated everlasting social changes to technology use. Similarly, technology (e.g., AI) will impact the future social structures in a very substantial way. In this interactive world, new technologies will survive as they deliver their promises. Additive Manufacturing (AM), as a significant revolution in manufacturing, has very strong promises. Luckily, it acquired the will of world leaders and peoples. Therefore, AM is at a very favorable historical spot to deliver its true promises without exaggeration for its sustainable future.

This article intends to place AM in a historical perspective. Technical arguments are qualitative. From that broad perspective, it is the aim to illustrate that although it is revolutionary, AM is part of a manufacturing sphere with centuries of experience and should interact with it constantly to increase its chance of rapid success.

TECHNOLOGY REVOLUTIONS

Throughout history, human endeavor has developed various ways to make tools and devices to help sus-

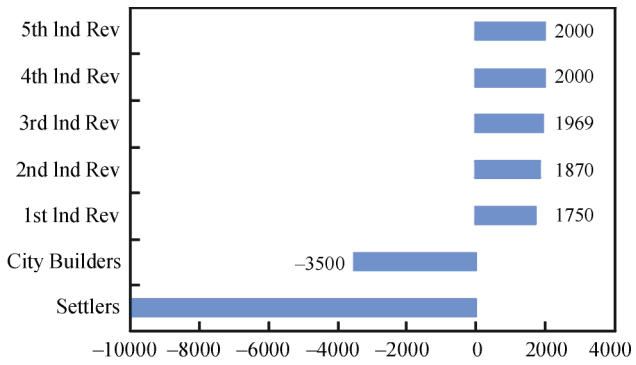

Figure 1. Technology revolutions [3]

tain human life. The pace of these developments was unnoticeable until the end of the last ice age in 10000 BCE, which then took a sharp stride as seen in Figure 1. After their first documented evidence of existence about 7 million years ago, early human migration from Africa to occupy the entire world dates back to 1.6 million years ago, and signs of tool making goes back to 2.5 million years ago [3]. Following a long period of hunting and gathering, humans settled and started agriculture in around 10000 BCE in the Fertile Crescent, which envelopes the Levant, southern Turkiye, and northern Iraq. This was the Neolithic revolution. Tools were made from naturally available materials such as bone, stone, wood, straw, mud, etc. The next revolution came 6500 years later in 3500 BCE. At this time, humans learned to use bronze and formed city states. It was also around this time the first examples of writing appeared in Mesopotamia by Sumerians. Another 5250 years were needed to reach the first industrial revolution in about the 1750s, started in England. Mechanization was the motivation of this revolution. At that point, it became clear that human intellect dominated the manual labor of old times. That surged brainpower brought the second industrial revolution, electrification, in the 1870s, only about 120 years after the first one. The third industrial revolution, automation, ensued even faster in 1969, less than 100 years following the second. Digitization, the fourth industrial revolution, in the 2000s is the latest advancement in the human endeavor to control their destiny through the use of new manufacturing technologies, Internet of Things (IoT), and Artificial Intelligence (AI). This evolution took place only 31 years after its predecessor. The fifth industrial revolution has already been underway since 2020 [4]. Obviously, time lapse between the revolutions has shrunk rapidly.

While manufacturing has transitioned from serving individual needs to serving societal needs (a tribe, local ruler, city, or country), it progressively has generated knowledge of making things, named technology. At some point, research based technology creation ensued. A systematically reasoned research then led to science, although it must have intuitively influenced the decisions of a stone-age tool maker, because he/she most probably had had a thought process about how to shave a piece of stone into a tool. In fact, the words science and technology are used, most of the time, in a compound form almost to mean the same thing, though they are different. Technology goes back to the time when humans developed the skills to make tools. This activity, however, did not need a deep understanding of fundamental principles of making or using the tools, which is defined as science. In other words, early humans did not need science to create technology. A more recent example may be the steam engine which was developed by Newcomen in 1712 and substantially improved by Watt in 1769. A scientific foundation for the working principles of the steam engine was offered by Sadi Carnot in 1824 when the first industrial revolution was already paving the way for the second [5]. Thus, the steam engine served human needs for more than a century without humans understanding its science, thermodynamics.

None of these revolutions were introduced or evolved without problems. A consequential anecdote from Queen Elisabeth 1st of England can be cited here [1]. William Lee develops the first stocking frame knitting machine in 1589. He seeks an interview with Queen Elisabeth 1st to show his invention and secure patent rights. The Queen refuses to grant a patent by asserting "Thou aimest high, Master Lee. Consider thou what the invention could do to my poor subjects. It would assuredly bring to them ruin by depriving them of employment, thus making them beggars." This and similar events delayed the first industrial revolution almost by two centuries. It is insightful to keep in mind that all industrial revolutions brought tragedies, but, like the people of England, humans always have found ways to better their lives. In fact, leaders and peoples who embraced contingent creative destructions have succeeded eventually [1]. Fast forward to today, it is very fortunate that there has been a desire from world leaders and peoples to implement new technologies to improve the competition in technology creation and subsequently human lives.

KNOWLEDGE CREATION

Scientific methodology for knowledge creation follows a series of steps such as observation, data collection and analysis, hypothesis development, hypothesis testing, refinement, and generalization. This is a mixture of two historical approaches, a deductive one and an inductive one. The inductive approach, initiator of the scientific methodology, sets out experiments to generate data to help understand a phenomenon,

whereas the deductive approach devises a hypothesis to explain a phenomenon. Both of these approaches have pros and cons. It is good to have a hypothesis that can explain multiple phenomena via a systematic approach, and it is also good to generate data based on observations of the physical world rather than on hypotheses created just for the sake of creating hypotheses. The inductive approach can also be termed a trial-and-error approach. For example, the Edisonian approach is this type. It is commonly attributed to Thomas Edison that success is meticulously exhausting thousands of unsuccessful ways to single out one successful way of developing a product or a process. This approach appeals to many as it infers perseverance, and Edison, indeed, created several great products/technologies. However, if a phenomenon can be explained by a simple, systematic calculation, why try to exhaust thousands of alternatives by experimentation [6]. In fact, modern economy does necessitate efficient use of resources. Thus, technology and science should rely on waste-free research approaches; an approach that is based on fundamental understanding of the interested phenomena coupled with lean project management.

ADDITIVE MANUFACTURING REVOLUTION

Additive manufacturing (AM) is one of the latest beads in the string of technology revolutions. Since its first patent granted in 1971 [7] at the dawn of the 3rd industrial revolution and its first wider appearance in rapid prototyping applications in the early 1980s, AM has evolved to become a functional part manufacturing technology. Although its evolution has taken place during the 3rd industrial revolution, it is frequently cited as one of the keystones of the Industry 4.0, Factory 4.0, or Manufacturing 4.0. It is a bottom-up, disruptive manufacturing approach which offers flexibility in time and space and makes on-time and on-site customized manufacturing possible. Thus, it has received tremendous attention from several industries ranging from toys to aerospace.

Interestingly though, AM has introduced itself as an immiscible entity within the global manufacturing industry which has a significant share (16 %) in the global economy [8]. In contrast, AM is only a blob of oil (0.057 %) in a large ocean of manufacturing [9]. The effort has been to emphesize how AM is superior to and different from traditional manufacturing (TM). While there is a truth to this and are significant differences, there are also fundamental similarities and opportunities where they can complement each other. Perhaps, enthusiasm and overexcitement, as a reflection of human nature to new beginnings, have led to the immiscibility.

However, all past revolutions were transient (evolutionary) socio-technological processes that lasted hundreds to thousands of years, except for the recent acceleration, paving the way to the next revolution. Each revolution was built over the knowledge generated during its predecessor. It is important to note that all human achievements should be revered, so AM is no different than the stone age technology revolution from a technology revolution perspective. Indeed, AM has stretched over several technology revolutions, 3rd, 4th, and 5th. Hence, it should embrace the vast knowledge that can be inherited from the earlier and present-day manufacturing as well as other contemporary technologies like AI and IoT. Indeed, AM can accelerate its success by interacting with TM. It is only that way AM can see what TM components it can transition, what gaps exist that cannot be covered by TM, and how it can fill those gaps.

ADDITIVE MANUFACTURING METHOD

Following sections intend to provide a comparative insight between AM and TM of metals to provoke a hand shake between the two. After a general focus on process reliability and comparison, fusion-based AM (FBAM), which is a melting-solidification process, is used as an example to illustrate fundamental similarities. Then, the article ends with sections on recent FBAM trends and effective utilization of skills. Although FBAM is exemplified, there are implications in the article that are applicable across various AM technologies (modalities) and material types. In any case, FBAM modalities comprise >90 % of the metal AM industry [9], so concepts in this article would resonate with most of the AM industry.

AM is a multidisciplinary technology. It takes sufficient understanding of each discipline to comprehend what it really takes to manufacture a validated component additively at a reasonable cost and scale. FBAM is a sub family of the AM technologies (modalities), primarily categorized into two groups in ASTM 52900 [10], powder bed fusion (PBF) and directed energy deposition (DED). The former uses powder as feedstock, and its energy source is either laser (PBF-L/M) or electron beam (PBF-EB/M). The latter can use powder or wire feedstock, and its energy source is laser (DED-L/M), electron beam (DED-EB/M), or electric arc (DED-Arc/M).

FBAM of metals involves transforming a feedstock into 3-dimensional (3D) components via first melting (fusion) and then solidifying it. The solidification behavior of the molten metal is very important for the final part performance. After all, it is the solidification behavior of the melt which leads to a distinct microstructure that essentially determines a variety of

properties and performances (e.g., mechanical, thermal, environmental, etc.) of an AM fabricated component. In addition, it is critical to understand the AM machine systems and their sub-systems such as the energy source, build chamber, feedstock management system, motion system, the atmosphere, and thermal management system. These functional systems enable AM to be an automated fabrication method. Furthermore, validation is a necessity for safe utilization and certification of a component. Hence, it should also be understood why a statistically significant validation is necessary for this complex process that is expected to yield a reliable product performance repeatedly. All these concepts are interrelated and can be successfully orchestrated for a business success by effective and efficient skills/resource utilization.

AM AS A RELIABLE PROCESS

AM is an automated, push-button process as advertised globally. Nevertheless, it takes a good amount of effort to make it really a reliable push-button process. It has been a misconception, at least in some spheres, that sophisticated manufacturing systems, such as those used for AM, should create parts so perfect that they should not require a thorough validation that quantifies reliability via qualification. In fact, validation is a piece within the total quality assurance in manufacturing. If the quality assurance is planned considering key performance indicators (KPIs) imposed by the application, there shouldn't be any awe or surprise when an AM fabricated component functions well in the aerospace, medical, high pressure/temperature, or other challenging applications. Nevertheless, the initial excitement on AM concealed the effort needed for Process Qualification (a.k.a. Operational Qualification, OQ) that confirms required material properties and final-product qualification (a.k.a. Performance Qualification, PQ) that guaranties the expected performance. Of course, the AM system itself and the operators should be qualified, too. These qualifications ensure a repeatable process and product performance for an AM system or reproducibility across several AM systems. They enable certification, too. It is a sour fact that validation is expensive and time consuming. Luckily though, multiphysics and multiscale simulations aided by AI can offer a tremendous help in the design of AM suitable feedstock (alloys) [11], component geometry [12–14], and process [13–15]. They will, in turn, enable desired product performance at a reduced time and cost by enabling print/fabricate right the first time and validate the first time.

Additive Manufacturing Original Equipment Manufacturer, AM OEMs have an obligation to assure safe and reliable operation of their sub-systems and integrated systems through statistically significant repeatability and reproducibility analyses. It is good to see the OEMs continue to release improved new systems. It would be even more appealing if they also published their process capability indices or Sigma levels for each one of their systems. The OEMs should be encouraged through regulations and customer behavior. Nonetheless, it is the due responsibility of the final component manufacturers and users to make sure a component is appropriately validated for a safe utilization. As such, it is essential to realize that validation is a cumbersome but a necessary step in manufacturing, and there is not a magical wand to make stuff happen. Standards such as ASTM 52920 and 52930 [10] can provide guidance in qualifications of the systems, processes, and part performances. Actually, the AM community can borrow a lot from the experiences of the Technological Manufacturing (TM) community with regards to validation and standardization. After all, analysis methods (data generation and processing) used for a component's testing and validation are agnostic to how the component is manufactured. Fortunately, AM service providers recently started implementing AM according to principles of manufacturing [16].

AM PROMISES AS A MANUFACTURING TECHNOLOGY

Let's step back and revisit a question, backed up with an almost 40 years of AM evolution. How advantageous is AM compared to, for example, Computer Numerical Control, CNC machining which has about 80 years of history as a TM method? When talking about AM, almost everybody starts by expressing that AM is a digital manufacturing; it is enabler of the Industry 4.0. Yes, everybody is correct. However, CNC manufacturing is also fully digital. A CAD is used in Computer Aided Manufacturing, CAM operations to fabricate the final part directly. Feedstock management during the machining is not as complex as it is in AM. Heat treatments or surface treatments are generally the only and well-understood post processes, unlike elaborate AM post processes. It is hard for AM actually to compete with fully digital CNC machining centers without its other advantages such as part consolidation, possibility of complex geometries especially with internal features or lattice structures that improve product functionality and/or performance, low buy-to-fly ratio, no-tooling requirements, rapid prototyping for design iterations, and low inventory requirements. Furthermore, since a single AM machine is able to build multiple geometries, shop floor complexities can be reduced. These are obviously

significant advantages. One other advantage AM has promised is distributed manufacturing. Design files can be sent to AM farms in multiple locations on earth (and space) to print the same geometry with the same qualities everywhere. Even so, considering increased footprints and investment costs of AM systems, one can make a similar claim for CNC machining centers, though this is still a realizable promise with small footprint AM systems. Yet another promise of AM is the democratization of manufacturing. Nevertheless, the democratization can also be tarnished by similar arguments made for distributed manufacturing. Of course, when possible, the distributed manufacturing can help with supply chain. In view of the foregoing, it seems an overall reevaluation of the AM promises is due. Beyond all, a real value assessment of AM is only possible through a total life cycle analysis which fortunately has gained traction in recent years [17].

Surely, AM has a disruptive potential that may make some TM methods obsolete in the long run, but it has a complementary, enabler characteristic for TM as well. For example, AM can fabricate tools and equipment for TM such as metal injection molds, forging dies, casting molds and cores, etc. Either disruptive or with great complementary potentials, AM is another manufacturing method. As such, it can learn a lot from the TM experience, especially with regards to statistically significant process and product validation procedures. Conversely, instead of behaving as an immiscible entity within the manufacturing community, AM should establish a bridge into traditional manufacturing and use its knowledgebase.

FUNDAMENTAL SIMILARITIES BETWEEN THE TM AND AM SOLIDIFICATION PROCESSES

As stated earlier, solidification behavior determines the microstructure of a component which in turn dictates the performance. Hence, knowledge of solidification is essential for a successful FBAM fabrication. This knowledge also can orchestrate the AM systems/sub-systems to prevent formation of micro defects like pores and cracks and macro defects like geometric/dimensional nonconformity. Furthermore, understanding of the solidification process helps achieve desired AM fabricated component performance.

It is relavant to mention here, in passing, that powder metallurgy routes for component manufacturing also exist and form the basis for sinter-based additive manufacturing (SBAM) technologies. There is a vast amount of knowledge in the powder metallurgy industry that SBAM can benefit.

Performance of a component depends on its material properties which, in turn, are dependent of its microstructure that is dictated by its processing history. When the ingredients (chemical composition) of a component is fixed, the process history defines its performance. Until they are ready for service, most industrial components go through primary/secondary melting operations that form the raw feedstock as billets or rods to be used in primary/secondary manufacturing operations like casting, atomization, forming, joining, or machining. An AM fabricated component assumes its net-/near net-shape during the AM process. It cannot, for example, go through a forming (forging or rolling) operation that can modify the grain structure and may alleviate internal porosity. Therefore, AM is a single step, final operation to create a geometry, similar to casting.

All AM modalities that involve melting of a feedstock followed by its solidification can be analyzed by principles of the solidification science. Some of the processes that involve solidification are casting, directional solidification, single crystal growth, vacuum arc re-melting (VAR), electro slag re-melting (ESR), welding, and FBAM. These methods are illustrated by cartoons in Figure 2.

In FBAM, creation of a desired microstructure in a component for a given alloy and a geometry conforming to CAD is attainable by managing thermally driven phenomena like heat transfer, fluid dynamics, undercooling, stress, etc. One should realize that equation systems that describe these phenomena are same for the FBAM and other solidification processes with varying boundary conditions. For example, FBAM is very similar to traditional melting based welding which is similar to traditional continuous directional solidification. They are all dynamic solidification processes with a moving heat source, but the fundamentals are similar to stationary casting, too.

During solidification, a molten substance starts transforming into a solid when its temperature drops below the melting point. This transformation forms a solid-liquid (s-l) boundary (interface) separating the two phases. Fate of this interface is driven by the heat flux and the composition profile ahead of it, which in turn, controls the morphology and size of the forming solid.

Heat flux during solidification can be from the melt to the solid or vice versa. In the former case, the interface moves in the opposite direction to a constrained heat flux in a positive temperature gradient. However, when solid grains form in the melt due to random temperature fluctuations or inoculation, the interface advances in the direction of an unconstrained heat flux in a negative temperature gradient. The temperature gradient is defined from the melt to the solid. In other words, in directional solidification, the heat is extract-

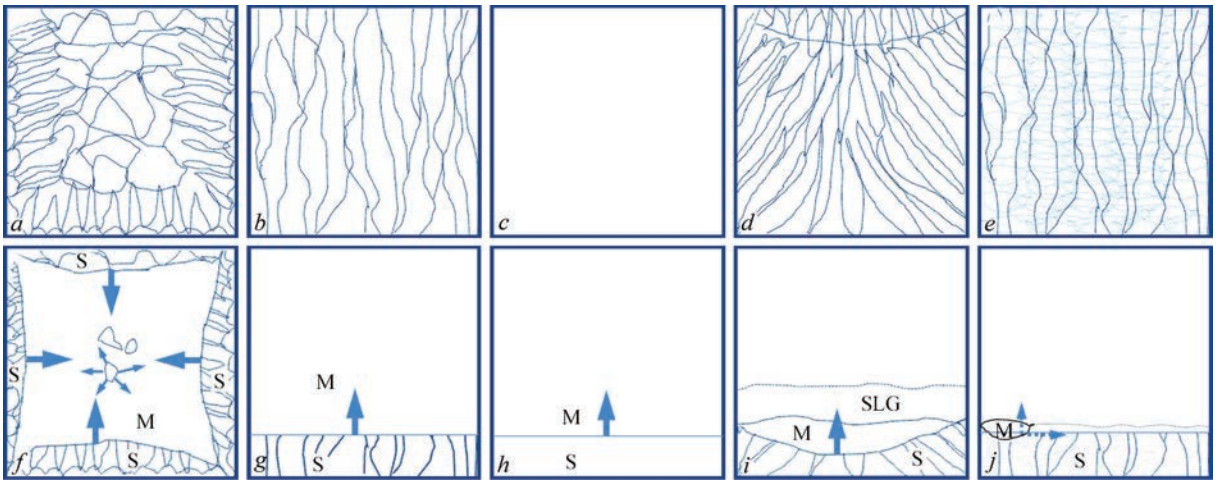

Figure 2. The top row sketches illustrate grain microstructures that can be created by solidification methods sketched in the bottom row. Grain structure after (*a*) casting, (*b*) directional solidification, (*c*) vertical Bridgman type single crystal growth, (*d*) electroslag re-melting (ESR) and vacuum arc re-melting (VAR), (*e*) FBAM. Arrows in (*f*–*j*) show direction of the solid-liquid interface during solidification. A slag (SLG) layer exists in ESR, shown by a dashed line in (*i*). A melt pool is outlined in (*j*) with dotted line representing powder bed. S indicates the solid and M the melt

ed thorough the solid (melt is hottest), but in the equiaxed solidification, the heat is extracted through the melt (solid is hottest, the middle grains in Figure 2, *f* and Figure 3, *b*). Although an interface stability analysis is beyond the scope of this article, it is important to review the basic conditions leading to the stability/instability as they determine the morphology of the grain microstructure. When the interface advances in a planar fashion, it is said that the interface is stable. On the other hand, when random perturbations form at the interface and grow in time, the interface becomes unstable. The perturbations follow a direction defined by the heat flux and the crystallographic orientation

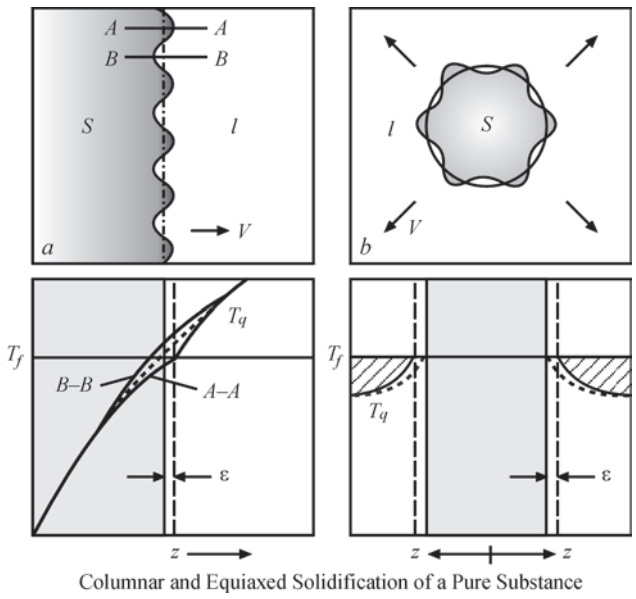

Figure 3. In directional solidification of pure substances, any perturbation (ε) in a positive temperature gradient melts back (left images). A solid nucleus in the melt assumes a dendritic morphology at its interface and grows into an undercooled melt (hatched) in its vicinity (right images). T_f is the melting temperature, and T_q is the real temperature [18]

of the solid perturbation. The directional solidification may take place with a stable interface to yield a single grain (single crystalline) microstructure, while the equiaxed solidification has an unstable interface with random nucleation sites that leads always to a poly grain (polycrystalline) microstructure.

Composition profile ahead of the interface also plays a decisive role in the stability/instability of the interface. In fact, a positive temperature gradient is adequate to suppress the instability during the solidification of pure substances, like pure metals or semiconductors, because thermal undercooling is the only driving force for the instability, Figure 3. This is useful to keep in mind when AM fabricating pure metals. However, during the solidification of alloys, another phenomenon, called constitutional (compositional) undercooling, develops due to a solute accumulation or depletion (C_L) ahead of the interface. Figure 4 represents the case of the solute accumulation. Equilibrium melting temperature (T_L) in this undercooled region of the melt is greater than the actual local temperature (T_F). Hence, the s-l interface advances into this undercooled region between the T_L and T_F to form cellular or dendritic grains depending on the s-l interface velocity (V) and temperature gradient (G) ahead of the interface.

In casting (Figure 2, *a*, *f*), the melt loses its heat into its surroundings in all directions. This enables formation of solidification fronts initiating from periphery of the melt's container, the mold. The result is a non-uniform grain morphology ranging from fine equiaxed at the periphery to coarse equiaxed ones in the middle. Elongated grains exist between the two regions. It is noteworthy that grain morphology (shape) as well as the scale (fine vs coarse) change during the

solidification. Two main parameters are responsible for these, s-l interface velocity (V) and temperature gradient (G) ahead of the interface as seen in Figure 4. The GxV controls the scale of the microstructure where a high value leads to a fine microstructure (cast periphery, Figure 2 (F)) and a low value leads to a coarse one (cast middle). The ratio G/V controls the morphology. The middle of the cast has a low value of the G/V that gives rise to an equiaxed dendritic solidification. In contrast, intermediate values of GxV and G/V between the periphery and middle of the cast yield a columnar dendritic grain morphology.

Directional solidification (Figure 2, *b*, *g*) restricts the heat transfer to the axial direction. Therefore, the solid grains form and grow bottom-up in this direction, and grains take an elongated morphology because their lateral growth is restricted. Although all of the grains are largely aligned in the axial direction, their crystallographic orientations are different. That is the reason for the existence of grain boundaries. A more precise solidification control is necessary to suppress the grain boundary formation during the solidification. First, the lateral temperature and composition variations should be eliminated. Second, a high positive G/V is necessary in the axial (vertical) direction to suppress s-l interface instability, Figure 5. These conditions should yield a single grain (Figure 2, *c*, *h*) when the solidification is complete.

Grain microstructure of the Vacuum Induction Melting/Vacuum Arc Remelting, VIM/VAR continuous solidification (Figure 2, *d*, *i*) follows similar arguments where a vertical steady temperature gradient leads to elongated grains, and the lateral temperature variations generate a polycrystalline grain structure.

It is worth noting that the s-l interface in all of these solidification methods advances by addition of new atoms from the liquid to the solid. That is to say the interface advances continuously by additions of new atomic layers. This is additive manufacturing at atomic scale. The single crystal growth processes (Figure 2, *h*) is especially useful to visualize the additive nature of the solidification. It is also important to understand that the solidification takes place in the entire interface at the same time in these traditional solidifications. In contrast, in FBAM, an energy source melts a metallic feedstock (powder or wire) and then allows for its solidification following a lateral path in a plane. This is to say the solidification is compartmentalized. When the melting and the solidification of the geometry in the lateral plane is complete, several atomic layers are added to the previously created solid layer, and the additions repeat in a compartmentalized (lateral) and discontinuous (axial) manner until all of the planned number of lateral planes (layers/slices) are melted/solidified. A checkerboard scan strategy or the area melting, to be briefly introduced later, may be useful to visualize the compartmentalized solidification. Therefore, FBAM is new only in that the solidification is compartmentalized into a much finer

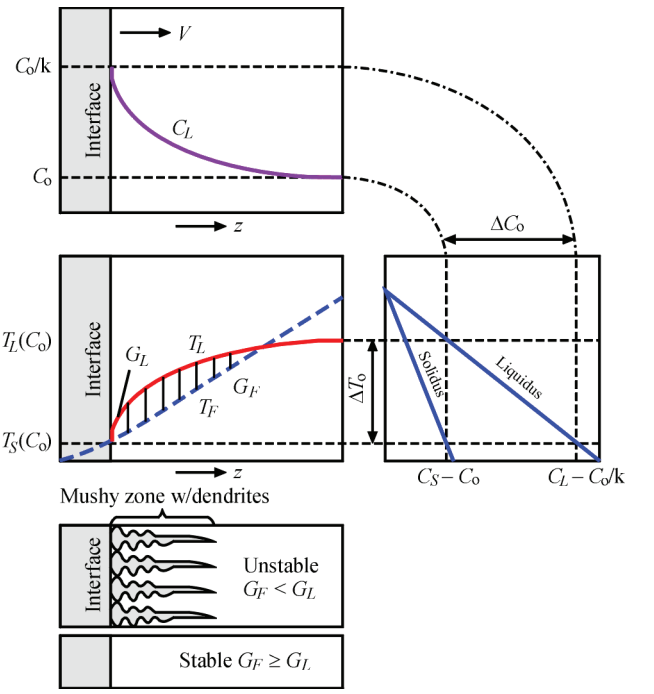

Figure 4. Accumulated solute profile C_L ahead of the interface (top) leads to temperature profile T_L (middle-left). The hatched region is undercooled into which s-l interface advances (bottom). A sketch of the partial phase diagram is on the middle-right. G_L is the equilibrium temperature gradient, and G_F is the actual one

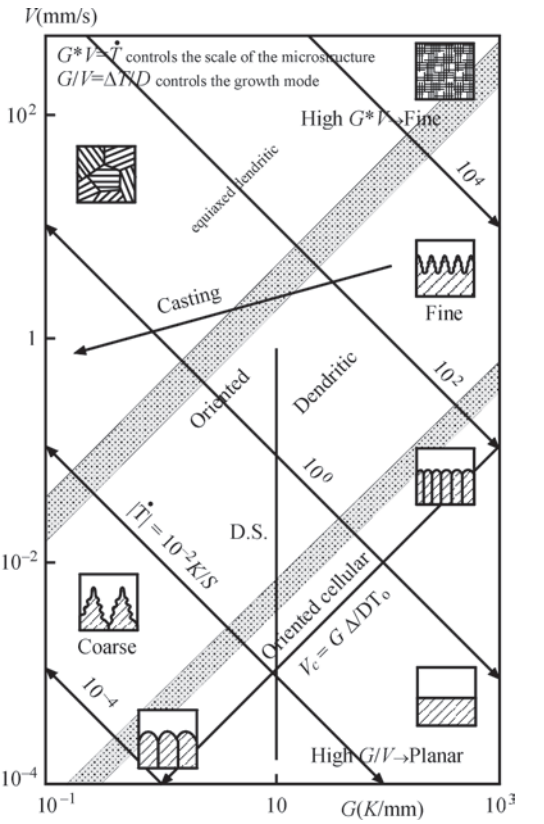

Figure 5. Solidification morphologies [18]

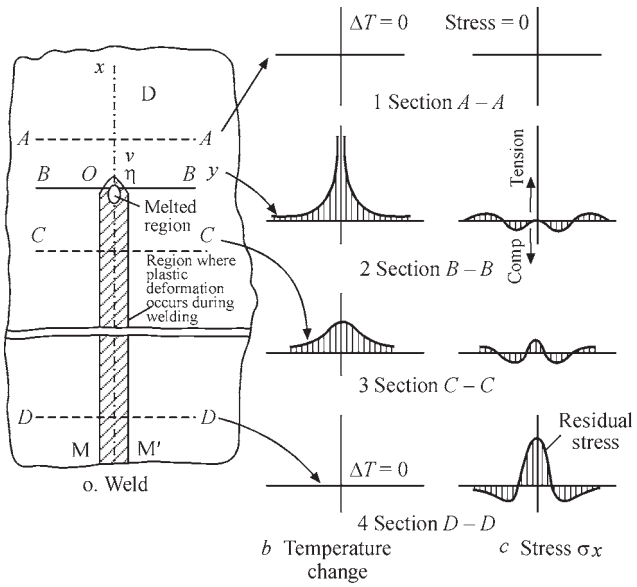

Figure 6. Evolution of temperature and stress during a single-track melting [19]

resolution in the lateral directions. Otherwise, layered (additive) solidification is a very old method that can be seen in a variety of methods as explained so far and illustrated in Figure 2.

Whether it is PBF or DED, in essence, FBAM is a process akin to welding by melting. Nevertheless, there are differences between the welding and FBAM processes. In the welding, microstructure in and around the weld is discontinuous. The temperature and stress fields are also localized to the welded region as seen in Figure 6 [19]. In contrast, a repeated melting and solidification in FBAM alleviates the stress localization and the grain structure is not discontinuous, as seen in Figure 2, *e*. The energy source (laser, electron beam, or electric arc) creates a melt pool on the previously produced layer on interacting with the feedstock (Figure 2, *j*). When the energy source moves, the melt pool then starts solidifying from the tail. The solidification is certainly similar to the welding and in a way similar to casting as described above. Thus, the melt pool solidifies from the periphery towards the middle. The previously created layer serves as the mold. Boundary conditions of the melt pool (solid, packed powder, or gas) determines the grain microstructure according to G/V and GxV of the interface [20]. Usually, the elongated grains, similar to ones in Figure 2, *a* and commonly seen in the welds, extend from both sides and collide at the weld centerline because of the welded plates acting as heat sink and a much narrower mold width than the conventional cast mold. A side water cooling in continuous casting creates a grain structure more similar to welding (Figure 2, *d*). Of course, the grain structure that forms in a layer is re-melted during creation of a subsequent layer. Thus, the grains in the new layer continues from the previous ones. This leads to a typical directional, long grain structure in the FBAM fabricated parts (Figure 2, *e*). Additionally, the boundaries of the individual melt pools are discernible in FBAM. That is because of the rapid solidification yielding fine grains at the base of the mold (previous layer) and trapping of accumulated solute ahead of the interface (Figure 4). Such marks are also commonly observed in single crystal growth when the interface velocity rapidly changes [21]. The degree to which melt pool boundaries show up depends on the solidification rate and alloying elements that are rejected from the solid solution. However, observed dendritic or cellular grains in these regions indicate absence of an absolute solute trapping which manifests itself with a planar interface and partitionless solidification (uniform composition) at extreme high solidification rates. As seen in Figure 7, the dendritic/cellular tip radius and spacing decreases with solidification velocity where capillary forces lead to the absolute interface stability. On a similar note, dendritic grain structures seen in atomized powders indicate that solidification rate is not high enough to experience the absolute stability. These basic solidification principles have guided many research works in academia and industry to create engineered grains in FBAM fabricated components. The attempts range from local grain engineering to single crystal solidification [20].

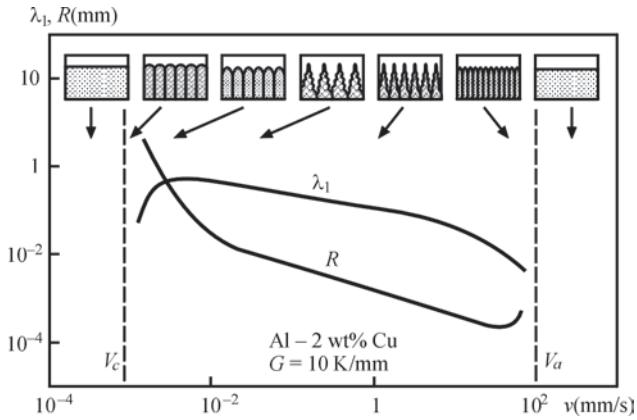

Figure 7. Morphology, tip radius (R), and spacing (λ_1) of cells and dendrites. V_c is the boundary of the constitutional stability, and V_a is the boundary of the absolute stability [18]

RECENT TRENDS IN FBAM

A few recent advances, briefly touched upon below, are increasing melted area per unit time, low angle printing, laser beam modulation, process monitoring, and new alloy design. Without a doubt, each topic is actually so important that deserves to be treated in a separate article.

One recent trend, mainly in PBF-L/M, has focused on approaches to melt a larger area in a given time. This can provide a competitive edge to PBF-L/M

against the other high yield AM modalities. Building AM systems with multiple (>1) lasers is one approach, and using expanded laser beams that can melt an area (area melting) several orders of magnitude larger than a conventional single point laser is another. The multi laser and area melting PBF-L/M can compete in production yield. Certainly, increasing number of lasers should increase the production yield, but at an increased initial investment cost. Stitching in multi laser PBF-L/M still needs to be characterized thoroughly. Similarly, spatter interactions from concurrently active lasers needs elucidation. Also, a careful control of thermal distribution in the build chamber with multiple active lasers is necessary as it can affect the melt pool dynamics as well as the thermal distortion of the solid. A variety of area melting approaches based on pulsed diode lasers can be found in the literature. Some create a line or rectangular shaped laser beam by combining several individually switchable Gaussian laser beams [22]. Scanning of this beam over the build plane consolidates the powder into a solid. The ability to switch an individual laser on and off provides the spatial resolution. In another approach, several diode laser beams are homogenized into an area and then shaped by an Optically Addressable Light Valve (OALV) [23]. In any area melting approach, the laser pulse frequency required to melt a given area as well as the penetration depth is critically important because they determine the volume melted per unit time. Also, due to a large lateral dimensions to very small thickness ratio of a melted/solidified volume, an appreciably high stress may prevail in this volume during the area melting process. Notably, in area melting, it can be possible to promote a single crystal solidification because of its melt pool shape. Firstly, the packed powder thermally insulates the melt pool laterally to minimize the heat loss in those directions. Secondly, the base of the melt pool is in direct contact with a higher thermal conductivity solid which is expected to create a large vertical temperature gradient (G), parallel to the build direction. Thirdly, the melt pool is expected to be more quiescent than that in the keyhole mode of the Gaussian laser beam. Finally, a melt pool with a large, flat base oriented perpendicular to the high vertical temperature gradient is in a favorable orientation to solidify as a single grain. Thus, a very carefully balanced area melting process control may promote a single crystal growth as well as alleviate the stress in the solid. The forgoing also implies that a spatial modulation (shape) of a single laser beam may help with single crystal solidification through modification of the melt pool shape.

Low angle printing is still an ongoing, recent effort to eliminate supports in PBF-L/M. Currently, there are AM systems that can fabricate as low as 20° planes from the horizontal without supports, which is a huge advance from 40° that was common just a few years ago. A cautionary note is necessary about this trend. The low angle printing is realized by manipulating the process parameters in downskin regions which serve as a crust to transition to the bulk build parameters. It goes then without saying that a downskin region has a different microstructure and so material properties due to different G/V and GxV than the bulk. Defect density in the downskin may be different, too. It is important to realize that this region is an external surface that interacts with its surroundings and influences surface related material properties and performance like corrosion and fatigue. At this point, it is trivial to see that a validation procedure must take this downskin into consideration. The downskin either should be appropriately validated or removed during a post-processing operation.

Laser beam wavelength and shape modulation, which have found a place both in the PBF and DED, is an advancement that can help control the solidification (melt pool) dynamics. The modulations can also help manipulate thermal conditions to alleviate fabricated component distortion. A vast number of academic and industrial work, as well as commercial [15] multiphysics and multiscale simulation tools, is available on melt pool dynamics and thermal management during the FBAM fabrication which can help to obtain desired part performance through engineered microstructures.

The FBAM process monitoring is still evolving. It is accomplished by either passive or active monitoring. In the passive monitoring, AM system parameters are monitored to predict process anomalies. In the active approach, different types of on-/off-axis sensors are utilized. The monitoring is useful in that it can tell where, when, and sometimes how/why a defect forms. Its technical feasibility and value per cost, however, prevent its full penetration into the AM fabrication. Data management is also a big issue. Defect information from each of the thousands of layers can be obtained at the scale of a melt pool or of a layer by visible/infrared based sensors (seeing eyes) with various spatial and/or spectral resolutions. Alternative approaches based on hearing, like acoustic and ultrasound, have been suggested. More elaborate monitoring approaches have been implemented by fusing several seeing and hearing sensors. Considering the complexities of the monitoring, it is legitimate to ask if the process can safely proceed without being monitored at all? In fact, a geometry and material specific process parameter set and path definition, empowered by physics in-

formed AI, can prevent processing defects. Then, the focus may be on identifying the probability of a defect occurrence to prevent the occurrence.

Metal AM has been practiced so far by using conventional metallic materials (pure or alloy). Those materials are the ones usually available for welding. The reason is obviously the thermo-mechanical similarity between the welding and FBAM processes as stated earlier. The welding community has developed in many years the proper metals that are durable against phenomena like melt undercooling, strain age cracking, liquation cracking, centerline cracking, etc. New metals are necessary to push the frontiers of FBAM forward. Multiphysics and multiscale simulation tools based on thermodynamics and AI should be utilized for a faster material (alloy) design to keep up with fast pacing evolution of the AM technology [11].

SKILLS REQUIRED IN FBAM

Among the essential resources of a company, human resources is the one with outmost importance. It is a company's personnel who simply make the business function. When a company secures required finances, facilities, and equipment, the success forward depends strongly on the human capital which includes leadership and individual contributors.

As mentioned at the start, AM is a multidisciplinary technology. Each discipline demands a specialized skill set. It is practical to group the skills as ones that relate to the AM processes and others that relate to building or operating the AM systems. Usually though, individuals carry out tasks in either group regardless where their strongest skills lie.

The process related skills in FBAM include specializations, for example, in heat transfer, fluid dynamics, solid mechanics, and solidification. The system related skills require specializations in the energy source, motion systems, temperature control, environment control, and feedstock management. Only a good match of a specialization and a required skill can lead to success. For example, an expert in mechatronics may be very skillful in operating an AM system, but process development in that system begs for other skills. Similarly, a fluid dynamics expert can very satisfactorily simulate and describe behavior of a melt pool in FBAM, but interpretation of why the solid does not follow a heat flux direction perhaps needs knowledge of preferred solidification directions dictated by heat flux as well as crystallographic structure of the solidifying metal.

In new technology development, concepts can be demonstrated and verified through multiple experimentations. However, when involved parameters are many, which is the case in FBAM, simulations can help. For an efficient resource utilization, both in the experimentations and simulations, it is important to know what parameters to investigate and how to investigate them. A purely inductive, trial-and-error approach will only generate waste in resource utilization, though success is possible. In contrast, a systematic approach based on fundamental understanding of the involved phenomena can help with an efficient AM technology development. Thus, suitable expertise and skills should be tasked to facilitate the correlations between the fundamental phenomena and the investigated concepts to correctly set a simulation or conduct only necessary experiments. That brings efficiency to an investigation and prevents waste in resource utilization.

A fast paced new technology development journey necessitates the highest level of expertise and skills that might be obtained either by formal education or by experience. This is presently relevant to AM as it still continues its technology developmental journey. The experts should recognize and dissect a problem effectively. They should be familiar with conducting systematic and efficient research which is essential to bringing a new technology to market fast and first in a cost effective manner. They also should know what information is needed to solve a problem, where to look for it, and how to access it. They should quickly absorb the information, analyze it, generate results, interpret them, and finally create procedures for implementation. This skilled workforce, of course, needs support of a servant leadership to function properly.

CONCLUSIONS

Intention of this article is to place AM in a historical technology revolution perspective. AM is a revolutionary manufacturing technology, but it will certainly be seen as a "stone-age" technology for those living in millennia ahead of our present time. All revolutions (social or technological) come with an excitement which is in the human nature, but it should not curb seeing the broader landscape. The AM technologies have evolved passing through several industrial revolutionary epochs, the 3rd through the 5th. It is certainly very lucky that it can take advantage of many different types of technological and social advancements. The leaders and peoples of the world embrace the AM technologies. Traditional manufacturing methodologies that have been developed throughout the centuries together with contemporary AI and IoT are extending their hands to AM. It is time AM embraced this warm welcome.

The foregoing qualitative technical discussion has indicated that the core of FBAM is to have a controlled solidification process that yields sound products which

can be validated at first trial and then utilized safely. Although FBAM is a multidisciplinary technology, all of the relavant disciplines essentially support accomplishment of a flawless melting and solidification of a small melt pool that when it traverses an entire build plane and then repeats this for all of the sliced planes of a geometry, a successful solid component is created. For instance, any advance in modulation of the energy source targets a desired control of the solidification process to, let's say, increase the melting efficiency, reduce the spatter, or manage the thermal field in and around the melt pool to promote desired grain structure and accomplish geometric conformity. Similarly, a powder management system that spreads (or blows) the powder perfectly and prevents powder contamination aims to have a flawless solidification process. Moreover, a motion control system either of the build platform or the energy source helps to melt and solidify the feedstock flawlessly. Temperature and environment control of the process area also establish necessary conditions to enable a flawless solidification process. Finally, accommodations to keep the thermal stress under control are implemented to have a steady melt pool and its uninterrupted in-plane translation. Hence, all FBAM multidisciplinary activities can be orchestrated, by accurately assigned skill sets, around the need for a well-controlled solidification process to fabricate a microstructurally and geometrically flawless component for business success.

REFERENCES

1. Acemoglu, D., Robinson, J.A. (2012) *Why nations fails, currency*. DOI: https://doi.org/10.1142/S2251361213800037
2. Breiman, L. (2001) Statistical modeling: The two cultures. *Statistical Sci.,* **3**, 199–231.
3. Diamond, J. (2017) *Guns, germs, and steel — The fate of human societies*. W.W Norton and Company.
4. Sarfraz, Z. et al. (2021) Is COVID-19 pushing us to the Fifth Industrial Revolution (Society 5.0). *Pak. J. Med. Sci.,* 37(**2**), 591–594.
5. https://en.wikipedia.org/wiki/Nicolas_L%C3%A9onard_Sadi_Carnot
6. https://teslauniverse.com/nikola-tesla/articles/tesla-says-edison-was-empiricist
7. Ciraud, P.A.L. (1971) France Pat. FR2166526A5.
8. https://www.macrotrends.net/global-metrics/countries/WLD/world/manufacturing-output
9. (2023) *AMPOWER*. https://ampower.eu/reports/
10. *ASTM*. https://www.astm.org/
11. Montakhab, M., Balikci, E. (2019) Integrated computational alloy design of nickel-base superalloys. *Metallurgical and Materials Transact. A,* **50**, 3330–3342. DOI: https://doi.org/10.1007/s11661-019-05252-7
12. https://www.ntop.com/
13. https://www.materialise.com/en
14. https://www.ansys.com/
15. https://www.flow3d.com/
16. https://www.additivemanufacturing.media/articles/freeform-binder-jetting-does-not-change-the-basics-of-manufacturing?utm_content=291921550&utm_medium=social&utm_source=linkedin&hss_channel=lcp-10383111
17. https://amgta.org/
18. Kurz, W., Fisher D.J. (1989) *Fundamentals of solidification*. Trans. Tech. Publ.
19. Vishwakarma, K. (2007) *Microstructural analysis of weld cracking in 718 plus superalloy*: Ph.D. Thesis.
20. Mukherjee, T. et al. (2023) Control of grain structure, phases, and defects in additive manufacturing of high-performance metallic components. *Progress in Materials Sci.,* **138**, 101153. DOI: https://doi.org/10.1016/j.pmatsci.2023.101153
21. Balikci, E., Deal, A., Abbaschian, R. (2004) Antimony-doped germanium single crystals grown from the melt by the axial heat processing (AHP) technique. *J. of Crystal Growth,* 262(**1–4**), 581–593. DOI: https://doi.org/10.1016/j.jcrysgro.2003.10.074
22. Zavala-Arredondo, M. et al. (2017) Laser diode area melting for high speed additive manufacturing. *Materials and Design.,* **117**, 305–315. DOI: https://doi.org/10.1016/j.matdes.2016.12.095
23. Roehling, J. et al. (2021) Physics of large-area pulsed laser powder bed fusion. *Additive Manufacturing,* **46**, 102186. DOI: https://doi.org/10.1016/j.addma.2021.102186

CORRESPONDING AUTHOR

E. Balikci
Bogaziçi University, 34342, Bebek, Istanbul, Turkey.
E-mail: ercanbalikci@hotmail.com

SUGGESTED CITATION

E. Balikci (2024) Additive manufacturing revolution in the context of technology revolutions. *The Paton Welding J.*, **8**, 45–55.
DOI: https://doi.org/10.37434/tpwj2024.08.06

JOURNAL HOME PAGE

https://patonpublishinghouse.com/eng/journals/tpwj

Received: 13.06.2024
Received in revised form: 16.07.2024
Accepted: 20.08.2024

DEVELOPED IN PWI

LASER WELDING OF SPEED TRAIN CARRIAGES. Technology and equipment allow welding inner body elements with each other and with a thin-walled lining of carriages inside the carriage body in such a way that outer deformations and tarnishing colors are absent.

SUBSCRIPTION–2025

«The Paton Welding Journal» is Published Monthly Since 2000 in English, ISSN 0957-798X, doi.org/10.37434/tpwj.

«The Paton Welding Journal» can be also subscribed worldwide from catalogues subscription agency EBSCO.

If You are interested in making subscription directly via Editorial Board, fill, please, the coupon and send application by E-mail: patonpublishinghouse@gmail.com; journal@paton.kiev.ua

12 issues per year, back issues available.

348 Euro, subscriptions for the printed (hard copy) version, air postage and packaging included.

288 Euro, subscriptions for the electronic version (192 Euro, discounted subscription price for 2024 only). Sending issues of Journal in pdf format or providing access to IP addresses.

Subscription Coupon **Address for Journal Delivery**			
Term of Subscription Since	**20**	**Till**	**20**
Name, Initials			
Affiliation			
Position			
Tel., E-mail			

The archives for 2009–2023 are free of charge on
www://patonpublishinghouse.com/eng/journals/tpwj

ADVERTISING
in "The Paton Welding Journal"

External cover, fully-colored:
First page of cover
(200×200 mm) — $350
Second page of cover
(200×290 mm) — $275
Third page of cover
(200×290 mm) — $250
Fourth page of cover
(200×290 mm) — $300

Internal cover, fully-colored:
First/second/third/fourth page
(200×290 mm) — $200

Internal insert:
(200×290 mm) — $170
(400×290 mm) — $250

- Article in the form of advertising is 50 % of the cost of advertising area
- When the sum of advertising contracts exceeds $1001, a flexible system of discounts is envisaged
- Size of Journal after cutting is 200×290 mm

Address
International Association "Welding"
11 Kazymyr Malevych Str., 03150, Kyiv, Ukraine
Tel.: (38044) 205 23 90
E-mail: patonpublishinghouse@gmail.com; journal@paton.kiev.ua
www://patonpublishinghouse.com/eng/journals/tpwj